INVESTIGATING LABEL-FREE MARKERS AT NANOSCALE FOR LIQUID BIOPSY USING MULTIMODAL MICROSCOPY

MARIA AUGUSTA DO R. B. F. DE LIMA

UNIVERSITÀ DEGLI STUDI DI TRIESTE

XXXIII CICLO DEL DOTTORATO DI RICERCA IN NANOTECNOLOGIA

SUPERVISOR:
Dan Cojoc

ANNO ACCADEMICO 2019/2020

UNIVERSITÀ DEGLI STUDI DI TRIESTE

UNIVERSITÀ DEGLI STUDI DI TRIESTE

XXXIII CICLO DEL DOTTORATO DI RICERCA IN

NANOTECNOLOGIA

Investigating Label-Free markers at Nanoscale for Liquid Biopsy Using Multimodal Microscopy

Settore scientifico-disciplinare: **FIS/07**

DOTTORANDO / A
MARIA AUGUSTA DO REGO BARROS FERNANDES LIMA

COORDINATORE
PROF. ALBERTO MORGANTE

SUPERVISORE DI TESI
PROF. DAN COJOC

ANNO ACCADEMICO 2019/2020

SUPERVISOR:
Dan Cojoc

ABSTRACT

Liquid biopsy emerges as a noninvasive, easily repeatable, and potentially low-cost approach alternative to standard tissue biopsy. In most cases, it can be used to investigate the cause of symptoms or to help diagnose a number of different health conditions. Although originally used to designate analysis of non-solid tissues to screen for cancer cells, liquid biopsy also refers to the investigation of other general body fluids including its constituents characterization and not necessarily related to cancer.

In this thesis, three new applications for the usage of label-free markers in the analysis of body fluid cellular constituents will be presented. Digital Holographic Microscopy (DHM) and optical tweezers are applied to the characterization of ex-vivo generated and native red blood cells. In a second application, neutrophils precursors are characterized and classified according to its cellular and nuclear morphology during granulocytic differentiation. In a third proposed application, morphological markers retrieved by digital holographic microscopy are used to perform fast screening urinalysis, including leukocyturia and bacteriuria. Lastly, although not label-free, fluorescence superresolution microscopy is used to bring insights into why nuclear morphology can be used as a trustful label-free marker and shows the structural arrangement of lamin in the nucleus of neutrophil precursors with unprecedented resolution.

The use of optical tweezers and digital holographic microscopy provided related results in terms of cell deformation and membrane fluctuations for ex-vivo generated and native red blood cells, allowing a reliable discrimination between them. In the second application, digital holographic microscopic images provided additional information with respect to the standard fluorescence imaging of stained nucleus, allowing the discrimination between different stages of neutrophil differentiation with a label-free approach. In addition, the use of DHM to perform fast screening urine analysis allowed to identify urine components despite its low contrast in a flowing and turbid environment. Lastly, for the first time in literature, the supramolecular arrangement of the lamin meshwork in the nucleus of neutrophil precursors are presented with a $70\,nm$ resolution. Fast screening label-free liquid biopsies integrates the group of emerging approaches that will revolutionize the future of early disease diagnosis and therapeutic choice with disruptive impact on the society. All the investigations described in this Thesis were aimed to contribute to this promising and intriguing new scenario.

PUBLICATIONS

The results of the research have been published in two papers and make the subject of a patent and other three papers in preparation.

Bernecker, C., do RBF Lima, M. A., et Al. "Biomechanics of Ex Vivo-Generated Red Blood Cells Investigated by Optical Tweezers and Digital Holographic Microscopy," *Cells*, v. 10, p. 552, 2021.

do RBF Lima, M. A., Cojoc, D. "Monitoring Human Neutrophil Differentiation by Digital Holographic Microscopy". *Frontiers in Physics*, v. 9, p. 190, 2021.

do RBF Lima, M. A., Cojoc, D., "Investigating neutrophils differentiation: towards automatic screening of nuclear morphological abnormalities with Digital Holographic Microscopy". Poster presented at: 13th European Biophysics Congress; July 26, 2021; Wien, Austria.

Cojoc, D., do RBF Lima, M. A., Galiano, P., "Method and System to detect Bacteria and Other Cells and Classify Urine Samples.". Patent submission. (PCT/IT2020/000033).

Bernecker, C., do RBF Lima, M. A., et Al., "Biomechanics of Ex Vivo Cultured and Native Red Blood Cells". Poster presented at: European Red Cell Society (ERCS); September, 2020; Online.

do RBF Lima, M. A., Cojoc, D., "Cell Biomechanics Investigation by Quantitative Phase Microscopy". Oral Presentation at: Italian national conference on the physics of matter; October, 2017; Trieste, Italy.

ACKNOWLEDGEMENTS

I am glad to present this work and grateful for the support and assistance that have carried me through my dissertation projects. First and foremost, I would like to thank you Dr. Dan Cojoc, for offering me the opportunity to do this PhD under his supervision and for inspiring me on many different levels. I deeply appreciate your trust and the freedom you have granted me so I could combine a PhD with the demands of motherhood. Thank you for the kind guidance, which comprises but goes beyond the scientific domain.

I would like to acknowledge Prof. Lucia Pasquato for bringing me words of comfort, hope and inspiring me in one of the most difficult moments of this journey. Thank you for telling me that my pregnancy was a reason to be joyful rather than an obstacle in pursuing my PhD. I'll carry your kind words in my heart for my entire life.

I would like to acknowledge the people from the Optical Nanoscopy Department at the Max-Planck-Institut für medizinische Forschung in Heidelberg, which, nonetheless the pandemic, welcomed me in their laboratory. Thank you Dr. Stefan Hell for accepting me in his laboratory. Thank you Dr. Elisa D'Este for the warm welcoming, all the trainings, the trust and the precious help with STED and MINFLUX microscopes. Thank you Dr. Jessica Matthias, Clara-Marie Gürth and Jasmine Hubrich, for the trainings and support. You all contributed to a great and memorable experience. Vielen Dank und bis später!

I would like to acknowledge Anna Comini and Ilaria Pierdomenico from Friuli Venezia Giulia's Welcome Office and Rosita Glavina from the Department of Physics of the University of Trieste. Your help and support were fundamental so I could make through the bureaucracy of a foreign country.

A warm and big thank you to my laboratory-office mates and PhD colleagues. It was a pleasure to share this journey with you. Grazie di cuore: Valentina Masciotti, José Suarez, Alice Battistella, Teresa Steinhartová, Martina Conti, Michele Zanetti and Timur Nurmamytov. In bocca al lupo a tutti voi! Also a big thank you for the precious friends who became part of my family: Veronica Fantini and Carlo Scarpa. Grazie di esserci sempre.

Thank you for everyone who has influenced my life somehow. Dr. Maria Chiara Passoluinghi, for celebrating with joy my acceptance in the PhD and later, the life I was carrying in my womb. Thank you Prof. Edval J. P. Santos, for my very first scientific-tecnologic experience in the Laboratory for Devices and Nanostructures (UFPE) and to encourage me to pursue a scientific career.

My deepest gratitude to my parents: Manoel Fernando Neto and Marta Maria do Rêgo Barros Fernandes de Lima, who gave me life and a huge surname. Thank you for all the unconditional love and support they have always given me, together with my wonderful sister Fernanda and brother André. Thank you for being always close to me, nonetheless the physical distance. Eu os amo imensamente.

Last, but not least, thank you to the most wonderful person I have ever met in my life, which happens to be also my husband and father of my son Fernando: Guilherme Feitosa de Almeida. I'm grateful for his efforts to turn the prose of this life into poetry, into heroic verse.

With love and gratitude, I dedicate this thesis to my parents and in the memory of José do Rêgo Barros e Francisco Julião de Lima.

CONTENTS

LIST OF FIGURES

LIST OF TABLES

ACRONYMS

DHM Digital Holographic Microscopy

QPI Quantitative Phase Imaging

OPD Optical Path Difference

CTC Circulating Tumour Cell

RI Refractive Index

FFT Fast Fourier Transform

OT Optical Tweezers

CMF Cell Membrane Fluctuations

RBC Red Blood Cell

nRBCs Native Red Blood Cells

cRBCs Cultured Red Blood Cells

OOTs Oscillatory Optical Tweezers

QPI Quantitative Phase Imaging

DIC Differential Interference Contrast

UTI Urinary Tract Infection

STED Stimulated Emission Depletion

SIM Structured Illumination Microscopy

STORM Stochastic Optical Reconstruction Microscopy

SF Steerable Filter

NMS Non Maximum Supression

Part I

INTRODUCTION

1

LABEL-FREE MARKERS FOR LIQUID BIOPSY

1.1 LABEL-FREE MARKERS

Label-free markers refers to the group of biomarkers that, by definition, are able to indicate cellular, biochemical or molecular alteration in cells, tissues or fluids without the need of labels [1]. Later, the definition has been broadened to include biological characteristics that can be objectively measured and evaluated as an indicator of normal biological processes, pathogenic processes, or pharmacological responses to a therapeutic intervention [2].

These markers are usually extracted and evaluated at single cell (low throughput) [3, 4] or for high throughput, fast screening [5, 6]. Further, they can be classified as: screening biomarkers, which are used in risk prediction; diagnostics biomarkers, used to check if a disease is present; and prognostic biomarker, for monitoring disease progression [7].

Label-free markers utilize intrinsic physical properties of the sample, which includes the characterization of some properties: mechanical (flexibility, deformability, viscosity), electrical (charge, electrical impedance, dielectric permittivity), optical (refractive index), or phenotypical (morphology, weight) [8]. Label-free markers arises as a non invasive technology that bypass the intrinsic costs and time demands of labeling procedures.

1.1.1 *Mechanical Markers*

Cellular intrinsic mechanical properties, such as flexibility, deformability and viscosity have been shown to be promising biomarkers. For instance, the deformability of cells (i. e., compliance under an applied load) [9] is an indicative of underlying cytoskeletal or nuclear changes associated with various disease processes and changes in cell state [4].

Other mechanical properties extensively used as markers are: stress, defined as force per area; viscosity, which measures the degree to which a liquid resists flowing under an external stress; and stiffness, the extent to which a material resist deformation under an applied force [10]. For instance, stiffness have been used to characterize spherocytosis, a cytoskeletal disorder from red blood cells [11, 12]. Invasive cancer cells have shown increased cell deformability compared to benign or normal cells of the same origin [13–15] and changes in stiffness of leukocytes in response to activation with antigens or other signals [16].

Biomechanical markers can be either measured directly, as the examples above mentioned, or can be estimated from primary measurements. For instance, from cell membrane fluctuations (CMF) it is possible to estimate the bending modulus [17, 18]. In this way, additional mechanical markers can be extracted also with non-contact microscopic techniques, such as Oscillatory Optical Tweezers or Quantitative Phase Imaging (QPI) [17].

1.1.2 *Phenotypical Markers*

The importance of cell morphology can be best exemplified by the distinct morphologies associated with different cell types. The adage 'form follows function' applies to cells as RBCs, which its biconcave shape allows oxygen exchange at a constant rate over the largest possible area [19], granulocytic neutrophil differentiation, which nuclear morphology is associated to cell maturation, migration and the release of extracellular traps [20, 21] and sheet-like, polarized epithelial cells, that provide barrier functions through out the body [22].

Due to well-established relationship between morphology and cellular function, morphological biomarkers have become widely utilized to characterize cellular functional heterogeneity [23]. Common morphological features, that can be used as biomarkers are: cell area, perimeter, circularity and elongation, in two dimensional, and surface area, optical volume, sphericity and height (thickness) in three dimensions. Other phenotypical markers are mean corpuscular haemoglobin (for RBCs) and cell dry mass [17, 21, 24–27].

Although two-dimensional label-free morphological markers can be derived from standard microscopic techniques as bright field microscopy or phase contrast approaches, QPI additionally provides information about sample height and changes in its refractive index [17, 25–27]. In this thesis, Digital Holographic Microscopy is used as main technique to extract cellular morphological features.

1.2 LIQUID BIOPSY

The term liquid biopsy or equivalently, fluid biopsy is originally used to designate the sampling and analysis of non-solid biological tissues, as blood, to screen for cancer cells or tumor nucleic acids [28–30]. In most cases, biopsies can be used to investigate the cause of symptoms or to help diagnose a number of different health conditions. Where a pathological condition has already been diagnosed, a biopsy can be used to measure how severe or at what stage it is [31]. Liquid biopsy can designate also the investigation of other general body fluids like urine, synovial fluid, amniotic fluid, cerebrospinal fluids and serous fluid, including its constituents characterization and not necessarily related to cancer [32].

The concept of liquid biopsy is referred in this thesis as the analysis of the cellular components of body fluids. More specifically, label-free markers are suggested for the characterization of RBCs and neutrophil precursors during granulocytic differentiation in specific contexts other than blood analysis. However, the derived parameters can be extended to blood biopsy. Moreover, morphological markers are suggested to identify and count urine constituents.

2

MULTIMODAL MICROSCOPY

Multimodal microscopy consists on the use of more than one microscopic technique, either employing them simultaneously in the same setup [33], or separately, but investigating the same object of study [34, 35]. The combination of different microscopic readouts from the same specimen, opens new avenues to understand structure-function relations in biomedical research. Commercial microscopes, for instance, are usually equipped with epifluorescence or bright/-dark field microscopy, as a reference to some highly specialized modalities.

On the other hand, it is also desirable to combine two or more those highly specialized modalities working together to provide equally valuable perspectives from a single phenomenon. For example, Raman spectroscopy and Quantitative Phase Imaging (QPI) are complementary with each other as both morphological and chemical information can be obtained from the co-registered sample without fluorescent labelling [36–38].

Several studies also apply combined label-free and fluorescence imaging, because they can provide both structural and functional images from different working mechanisms. For instance, the implementation of QPI together with epifluorescence has been demonstrated in [39–41] and used to investigate live cell membranes in [42]. In another example, total internal reflection fluorescence (TIRF) was implemented in an Optical Tweezers (OT) instrument to perform single molecule experiments [43]. Label-free imaging provides structural and morphological indicators, while fluorescence imaging allows the visualization of specific molecules as labeled proteins.

In this chapter, I will introduce the two main microscopic techniques used in this Thesis to investigate label-free markers for liquid biopsy at single cell level and fast screening: Digital Holographic Microscopy (DHM) and Optical Tweezers (OT). Furthermore, Stimulated Emission Depletion (STED) microscopy was used to deeper investigate a morphological marker, so it will be also introduced.

2.1 DIGITAL HOLOGRAPHIC MICROSCOPY

The concept of Digital Holography Microscopy is understood here in the sense of digital recording of the holograms and the numerical reconstruction of the wave fields in a computer. There are many ways in which digital holography can be realized, including off-axis, in-line, coherent, and incoherent holography. Comprehensive reviews on the topic can be found elsewhere: [44–50].

In the next sections I will recapitulate the hologram recording and numerical reconstruction process of coherent digital holographic microscopy in off-axis configuration. Then, its application to the study biological phase samples will be introduced.

2.1.1 *Historical context*

Holography is already over half a century old, if we mark its birth from the first developed theory by Dennis Gabor (1948), while he was working to improve the resolving power of electron microscopes [51]. Gabor's theory was then validated by a number os scientists worldwide: G.L. Rogers, A.B. Baez, H. El-Sum, P. Kirkpatrick and M.E. Haine. Regardless its initial response from the scientific community, the interest in optical holography declined after a few years due to poor image quality caused by light sources with very limited coherence and poor quality recording plates.

In these early years, the mercury arc lamp was the most coherent light source available, and due to its low coherence, (in the micrometer range) it was only possible to produce holograms with this depth, thus restricting research. A further issue was the overlap of the desired image with the twin-image and the undirected light resulting in the DC-term in the reconstruction (as seen in Figure 2.1). These hurdles were overcome in the sixties with the invention of the laser by Maiman (1960) [52], whose coherent light was ideal for making holograms, and, with the separation of the reconstructed image terms by an off-axis setup developed by Leith and Upatnieks (1962) [53].

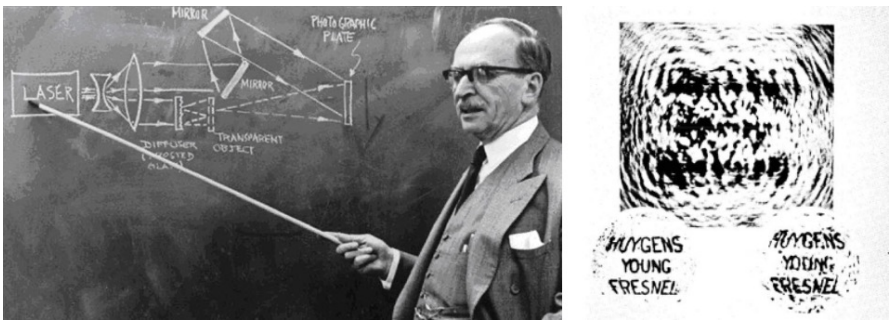

Figure 2.1: Dennis Gabor showing as an off-axis hologram of a transparency is recorded (left) and first hologram and first holographic reconstruction, 1948 (right). Images from [54].

Although many progress has been made, yet the object wave could be reconstructed optically but not be measured directly. In 1967, Goodman and Lawrence demonstrated the feasibility of numerical reconstruction of an image from a Fourier hologram detected by a vidicon camera [55]. Twenty-seven years later, Schnars and Jueptner were the first to use a CCD camera directly connected to a computer as the input, and compute the optical phase image in a Fresnel holography setup [56]. Only with the technological progress in the

computer field, as well as the advent of digital recording devices such as CCD- and CMOS-camera, Digital holography could replace physical and chemical recording processes with electronic ones, and the optical reconstruction process with numerical computation [45].

2.1.2 *Principles of Digital Holographic Microscopy*

Digital Holography can described as a two-part process: the first part consists in recording both the amplitude and phase of an electromagnetic wave scattered off (in reflection mode), or diffracted by (in transmission mode), an object. In practice, this can be achieved by illuminating an object with a coherent light source, interfering the resulting scattered light (the 'object beam') with a mutually coherent 'reference beam', and recording the resulting interference pattern on a digital media. This process is called *hologram recording* [45, 57].

The second part of the digital holography process is to 'reconstruct' the recorded hologram into a complex image. The reconstruction procedure takes place in a numerical environment rather than optically. This procedure is also known as *hologram numerical reconstruction* [45, 57]. As the recorded interference pattern has encoded both amplitude and phase information of the object, the reconstruction process recovers its three-dimensional nature [45].

In Digital Holography Microscopy (DHM), the image of the object is magnified before the hologram recording. There are two main recording geometries used in holography: *on-axis* (also called inline) or *off-axis*, according to how the reference wave is positioned with respect to the object wave [45]. In on-axis arrangement, the reference coaxially illuminates the hologram with the object wave. Alternatively, in off-axis configuration, the object and reference beams are combined with an offset angle, called *recording angle* [58].

2.1.2.1 *Hologram Recording in Off-axis configuration*

Considering that the light emanating from the object and the reference obey the scalar theory of light, so the object and reference waves can be defined, respectively, as:

$$\begin{aligned} \widetilde{O}(\boldsymbol{r}, z) &= |O(\boldsymbol{r}, z)| \exp^{j\phi(\boldsymbol{r},z)} \\ \widetilde{R}(\boldsymbol{r}, z) &= |R(\boldsymbol{r}, z)| \exp^{j\psi(\boldsymbol{r},z)} \end{aligned} \tag{2.1}$$

where ϕ and ψ are the respective phase factors and $\boldsymbol{r} = (x, y)$ and the waves are propagating in the $z-$direction.

The interference[1] between the object wave $\widetilde{O}(\boldsymbol{r}, z)$ and the reference wave $\widetilde{R}(\boldsymbol{r}, z)$ produces a distribution of intensity, which is written as an addition of four terms [59]:

1 In order for interference to be observed, the path-length difference between the beams should be within the coherence length of the light source.

$$
\begin{aligned}
I_H(\boldsymbol{r}_H, z_H) &= |\widetilde{O}(\boldsymbol{r}, z) + \widetilde{R}(\boldsymbol{r}, z)|^2 \\
&= |\widetilde{O}(\boldsymbol{r}_H, z_H)|^2 + |\widetilde{R}(\boldsymbol{r}_H, z_H)|^2 \\
&+ \widetilde{O}(\boldsymbol{r}_H, z_H)\widetilde{R}^*(\boldsymbol{r}_H, z_H) + \widetilde{R}(\boldsymbol{r}_H, z_H)\widetilde{O}^*(\boldsymbol{r}_H, z_H)
\end{aligned} \tag{2.2}
$$

where $I_H(\boldsymbol{r}_H, z_H)$ is the intensity of the hologram and the subscription H indicates the hologram plane. The term $|\widetilde{O}(\boldsymbol{r}_H, z_H)|^2 + |\widetilde{R}(\boldsymbol{r}_H, z_H)|^2$ is often referred as DC term and do not bring any information regarding the object's wavefront phase change. $\widetilde{O}(\boldsymbol{r}_H, z_H)\widetilde{R}^*(\boldsymbol{r}_H, z_H)$ and $\widetilde{R}(\boldsymbol{r}_H, z_H)\widetilde{O}^*(\boldsymbol{r}_H, z_H)$ represent the interference terms with $\widetilde{R}^*$ and $\widetilde{O}^*$ denoting the complex conjugates of the reference and object waves, respectively.

In off-axis configuration, the reference beam is set at an angle to the object beam. For microscopy applications, off-axis holography needs splitting the illumination beam in object and reference, and then recombining the reference wave with an image of the object captured. A common used approach to implement off-axis DHM is to use Mach-Zender interferometer geometry [21, 26, 41, 46, 48–50, 60–68].

Assuming the simplest and ideal case, where the reference beam is a plane wave with a phase factor equal to the angle it makes relative to the object beam, i. e., the recording angle (φ). Then, the reference wave can be described as:

$$
\widetilde{R}(\boldsymbol{r}_H, z_H) = |R(\boldsymbol{r}_H, z_H)|e^{-jk(x\sin\varphi + y\cos\varphi)}. \tag{2.3}
$$

From Equation 2.2, the interference pattern on the recording plane will be:

$$
\begin{aligned}
&I_H(\boldsymbol{r}_H, z_H) = |O(\boldsymbol{r}_H, z_H)|^2 + |R(\boldsymbol{r}_H, z_H)|^2 + \\
&\widetilde{O}(\boldsymbol{r}_H, z_H)|R(\boldsymbol{r}_H, z_H)|e^{+jk(x\sin\varphi + y\cos\varphi)} + \\
&|R(\boldsymbol{r}_H, z_H)|\widetilde{O}^*(\boldsymbol{r}_H, z_H)e^{-jk(x\sin\varphi + y\cos\varphi)}.
\end{aligned} \tag{2.4}
$$

The consequence of the angled reference beam was a linear phase shift along the (x,y)-axis of the recording plane. A schematic of the 2D Fourier transform of the intensity of a recorded hologram (Equation 2.4) is shown in Figure 2.2. The effect of the linear phase shift caused by φ in the space domain, becomes a linear translation in the frequency domain and the two last terms in Equation 2.4 are centred in $\pm(k\sin\varphi, k\cos\varphi)$.

The recording angle φ determines the spatial frequency of the interference fringes and consequently, the spatial separation (in the frequency domain) of the individual terms in Equation 2.4, shown in Figure 2.2. Thus, the choice of φ is constrained two conditions, in order to have a proper off-axis hologram recording [69–71]:

1. It must be sufficiently large so the spatial frequency spectra of the phase-shifted twin images do not overlap each other nor overlap the spectra of the DC term in Equation 2.4 (shown in Figure 2.2).

2. It must not exceed a maximum value, for which the carrier frequency of the interferogram is equal to the Nyquist frequency of the detector.

The conditions imposed to φ are directly related to the numerical aperture (NA) and magnification (M) of the microscope system, and to the wavelength (λ) of the illuminating source, since they determined the spatial bandwidth $\Delta\varphi$ of each Equation 2.4's terms. Further, for a digital recording media, with squared recording zone, uniform sampling and identical interpixel distance along both axes equal to Δp, the conditions stated above are mathematically described as [69, 71]:

$$\sin^{-1}\left(\frac{3}{2\sqrt{2}\pi}\frac{NA}{M}\right) \leq \varphi \leq \frac{\lambda}{2\Delta p} \tag{2.5}$$

2.1.2.2 *Numerical Hologram Reconstruction*

The optical hologram reconstruction is accomplished by illuminating the recorded hologram with the reference wave. In this way, Equation 2.4 becomes:

$$\begin{aligned} I_H(\boldsymbol{r}_H, z_H)\widetilde{R}(\boldsymbol{r}_H, z_H) = &|R(\boldsymbol{r}_H, z_H)|^2\widetilde{R}^*(\boldsymbol{r}_H, z_H) \\ &+ |O(\boldsymbol{r}_H, z_H)|^2\widetilde{R}^*(\boldsymbol{r}_H, z_H) \\ &+ |R(\boldsymbol{r}_H, z_H)|^2\widetilde{O}^*(\boldsymbol{r}_H, z_H) \\ &+ \widetilde{R}^*2(\boldsymbol{r}_H, z_H)\widetilde{O}(\boldsymbol{r}_H, z_H) \end{aligned} \tag{2.6}$$

In DHM, the reconstruction procedure takes place in a digital environment and the process described in Equation 2.6 is performed numerically. In this case, multiplication by the reference beam it is not necessary, rather, the numerical reconstruction methods focus on isolating the object term $\widetilde{O}(\boldsymbol{r}_H, z_H)$ from the recorded interference (Equation 2.4) and propagating it back to the object plane.

Isolating the Object Term

In digital holographic reconstruction, a main step is to isolate numerically the real object term from both the reference beam and the virtual object term in the recorded hologram intensity. In off-axis configuration, the effect of linear phase shift caused by the recording angle φ becomes evident when we consider the spatial frequency of the hologram. Applying a Fourier Transform in Equation 2.4, we have:

$$\begin{aligned} &\mathcal{I}_H(k_x, k_y) = \mathcal{F}\{I_H(x, y)\} \\ &= |R|^2\delta(k_x)\delta(k_y) + \widetilde{\mathcal{O}}(k_x, k_y)\widetilde{\mathcal{O}}^*(k_x, k_y) \\ &+ |R|\widetilde{\mathcal{O}}^*(k_x - k\sin\varphi, k_y - k\cos\varphi)) \\ &+ |R|\widetilde{\mathcal{O}}^*(k_x + k\sin\varphi, k_y + k\cos\varphi) \end{aligned} \tag{2.7}$$

where $\mathcal{F}$ denotes the Fourier transform operator and $\widetilde{\mathcal{O}}$ is the Fourier transformed object function. (k_x, k_y) are the coordinates in the Fourier space and z

is assumed to be constant in the hologram plane $z = z_H$. The Fourier transform of the $\widetilde{R}(\boldsymbol{r}_H, z_H)$ term is a delta function $\delta(k_x, k_y)$[59] centred on $(0, 0)$ in the spatial frequency plane.

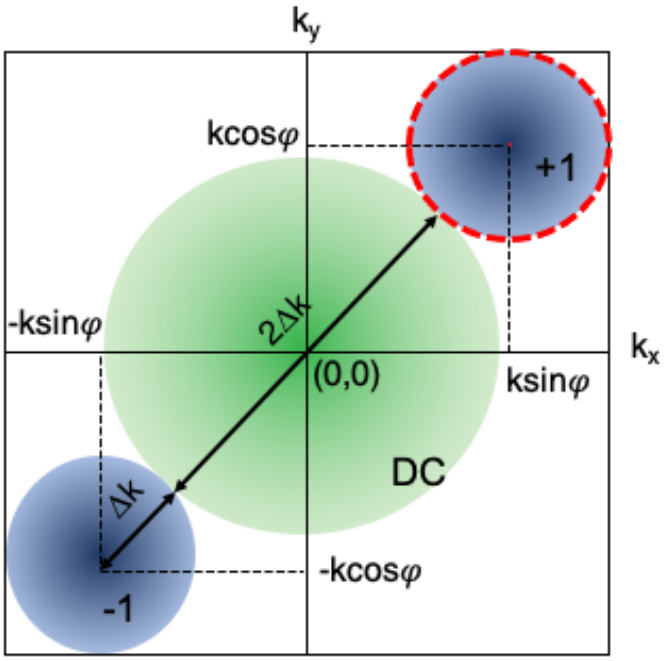

Figure 2.2: The Fourier domain of an off-axis hologram, with a recording angle = φ. (k_x, k_y) are the coordinates in the Fourier space. The DC term in centered in $(0, 0)$ and represented in green. The phase-shiffted object beams are represented in blue. Δk is two times the highest spatial frequency term in the object wave.

In Equation 2.4, the hologram is composed by four terms. The first two terms do not carry any information about the phase of the object and the angle of the reference wave. They produce, when Fourier transformed (Equation 2.7), the zero-order of diffraction (usually known as the DC term, represented at the center of the Fourier transform). The third and fourth terms are identified as the -1 and $+1$ diffraction orders in the Fourier domain and encode the whole sample information, both in amplitude and phase. Due to the off-axis configuration, the -1 and $+1$ diffraction orders are arranged symmetrically around the DC term in the Fourier. In Figure 2.2 and Figure 2.4 we have illustrated, respectively, a schematic and an image of the Fourier domain of an off-axis hologram.

To isolate the object term $\widetilde{O}(\boldsymbol{r}_H, z_H)$ from the recorded interference, we can simply apply a spatial filter in the Fourier domain containing the $+1$ diffraction order. The filter is represented as a red dashed line in Figure 2.2 and Figure 2.4. The size of the filter should be large enough to take the maximum frequencies from the object, but not so big to avoid introducing noise proceeding from the DC diffraction order [71]. In a diffraction limited system, the size of the filter

will be equal to two times the magnitude of the highest spatial frequency term in the object wave.

Hologram Backpropagation

To reconstruct a hologram consists in calculating its diffraction back to the original object plane towards the original illumination source. This is called *back propagation* and can be model as an electromagnetic wave diffracted from an aperture, but in this case the aperture is the hologram with a non-zero intensity distribution that modifies the diffracting beam [72]. The numerical approaches developed to describe the Diffraction Theory can be used to propagate back the hologram, given the conditions imposed by the propagating distance and wavefront modelling [57, 59].

One simple alternative, called *Convolution Approach*, gives a way to find the three-dimensional complex field generated by an object that has been imaged holographically $\widetilde{O}(x, y, z)$ by simply convolving the recorded object field in the hologram $\widetilde{O}(x_H, y_H, d)$ with the Rayleigh-Sommerfeld propagator [72]:

$$\widetilde{O}(x, y, z) = \widetilde{O}_H(x_H, y_H, d) * \widetilde{H}(x_H - x_0, y_H - y_0) \tag{2.8}$$

where d is the propagating distance and (x_0, y_0) are the coordinates of the origin of the wavefield after propagation (as illustrated in Figure 2.3).

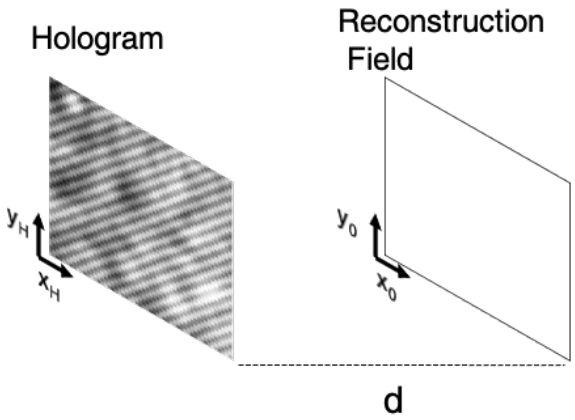

Figure 2.3: The geometry of the holographic reconstruction distance. d is the propagating distance and (x_0, y_0) are the coordinates of the origin of the wavefield after propagation.

From the Convolution theorem [57, 59], Equation 2.9 can be written as:

$$\widetilde{O}(x, y, z) = \mathcal{F}^{-1}\left\{\mathcal{F}\{\widetilde{O}_H\}\mathcal{F}\{\widetilde{H}\}\right\} \tag{2.9}$$

Finally, once the complex amplitude from $\widetilde{O}(x, y, z)$ is retrieved, we can compute the phase variation undergone by the the object wavefront due to the presence of a sample in the optical path. The phase of a complex function is

uniquely defined only in the principal value range (e. g.$-\pi$ to $+\pi$). The recover of original phases from the principal values is a classic signal processing problem, known as *phase unwrapping*. The wrapped phase images present discontinuities when the phase of the object has phases higher than $mod(2\pi)$ and require to be unwrapped to form a continuous phase map. The third image in hologram reconstruction workflow from Figure 2.4 illustrates the case of a wrapped phase.

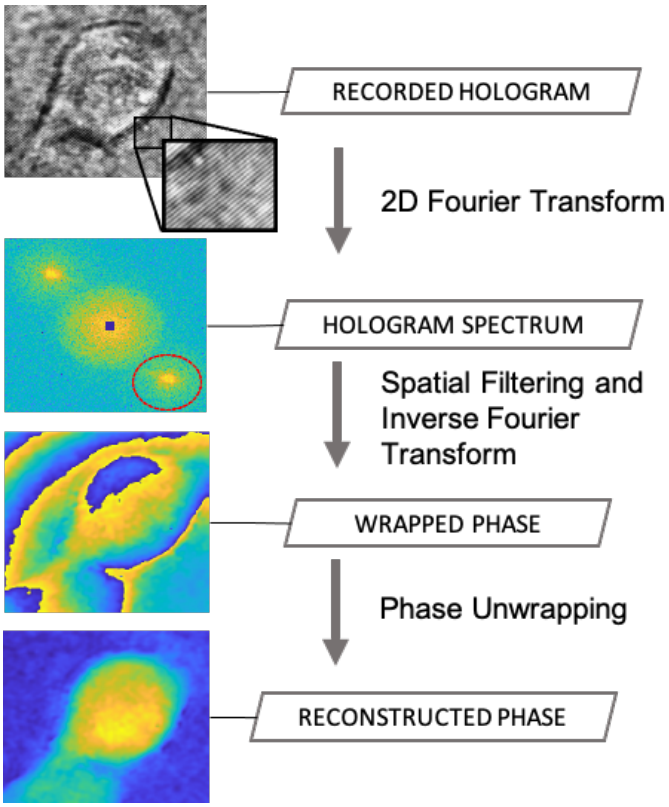

Figure 2.4: Hologram Reconstruction workflow: recorded hologram intensity of a neuroblastoma cell, followed by the FFT of the hologram with the zero-order in the center and its peak blocked by a square mask equal to zero. The two circular and symmetric patterns are the -1 and +1 diffraction orders. The +1 order is spatially filtered in the frequency domain and an inverse Fourier transform is applied. The retrieved phase before and after unwrapping.

There are many algorithms available for phase unwrapping, since this processing problem is present in a variety of applications, such as terrain elevation estimation, in synthetic aperture radar, field mapping in magnetic resonance imaging and wavefront distortion measurement [73], for instance. An extensive review on the topic can be found in the book [74]. In this Thesis, we have approached the phase wrapping problem using a customized version of Goldstein's branch-cut method [75], which was speeded optimized with flood fill algorithm by [76]. The original source code was written by Carey Smith and can be found in [77].

2.1.3 *Phase imaging of Biological Samples*

A considerable number of biological samples either do not absorb light, i. e., do not modify the amplitude of light or generate only modest changes in it . This makes them hard to image with bright field microscopy. On the other hand, those transparent specimens (also called phase objects) generally alter, or shift, the phase of light more significantly. Being a quantitative phase imaging (QPI) technique, DHM is suitable to investigate phase objects without the need of labeling, because it can quantify these phase shifts. DHM has recently been used in different setups to study morphology, structure and dynamics of unstained living cells [46, 48, 67]. The phase shift, δ introduced by a phase object is proportional to the the optical path difference (OPD), which depends on the object's thickness t and the difference between the refractive indexes (RI) of the cell, n_c and the medium, n_m:

$$OPD = t \cdot \Delta n. \tag{2.10}$$

The phase shift is defined as:

$$\delta = \frac{2\pi}{\lambda} OPD. \tag{2.11}$$

Many cell morphological features can be directly extracted from the OPD, e. g.OPD mean/median, phase volume, phase surface area, dry mass, phase sphericity, phase statistical parameters, energy. Moreover, knowing the cell refractive index (RI), various biophysical parameters, such as dry and wet mass, protein concentration, elasticity and conductivity can be derived. Both directly and derived OPD parameters are possible candidates to be used as markers for cell biopsy.

2.2 OPTICAL TWEEZERS

2.2.1 *Historical Context*

The existence of radiation pressure was first experimentally demonstrated by P. N. Lebedev in Russia (1900), and Ernest F. Nichols and G. F. Hull in the U.S. (1901). The first to propose that atoms could be trapped in a light beam was Vladilen S. Letokhov (1968), but in 1970, Arthur Ashkin proved experimentally that micron-sized particles could be accelerated and trapped in stable optical potential wells using only the force of radiation pressure from a continuous laser [78]. He trapped micron-size latex spheres suspended in water in between two focused, counter propagating beams of light. In 1986 Ashkin, Bjorkholm, B. Dziedzic and Steven Chu showed that particles that range in size between 0.02 and 10 microns can be trapped in a single focused laser beam [79], this was the advent of Optical Tweezers. After showing that optical tweezers could handle live bacteria and other organisms without apparent damage [80], Ashkin has drawn the attention of many biologists and biophysicist to this technique.

Since then, the applications of Optical tweezers has grown exponentially.

The historical context of Optical Tweezers written by its inventors can be read in [81] and [82]. Further references encompassing the technological aspects and applications include, but are not limited to [83], [84],[85], [86] and [87].

2.2.2 *Basic Principles of Optical Trapping*

In addition to carrying energy, light transports momentum and is capable of exerting mechanical forces on objects. When photons enter an object that has a different refractive index than its surrounding medium, part of the momentum of the photons can be transferred to this object. This transfer of momentum is the physical principle that underlies optical trapping [88]. If an object bends the light, changing its momentum, conservation of momentum requires that the object must undergo an equal opposite momentum change. This gives rise to a force acting on the object [89].

In a typical OT setup, the incoming light comes from a laser that has a Gaussian intensity profile. When this light interacts with a bead, the light rays are bent according to the laws of reflection and refraction. The sum of the forces from all rays can be separated into two components: the scattering force (due to radiation pressure), pointing in the direction of the incident light, and the gradient force, arising from the Gaussian intensity profile. This last one is a restoring force that pulls the bead into the centre. Figure 2.5a illustrates how a micro-sized particle is attracted to the gaussian laser beam.

Two different regimes of theoretical approach can be distinguished. They are determined by the ratio of the incident light's wavelength λ to the diameter D of the irradiated particle:

Rayleigh Regime

If the particle is very small compared to the wavelength ($D << \lambda$), the distinction between the components of reflection, refraction and diffraction can be ignored. Since the perturbation of the incident wavefront is minimal, the particle can be viewed as an induced dipole behaving according to simple electromagnetic laws [91]. In this case, the *scattering force*, which arises from the absorbed or reflected light, points towards the propagation of the laser beam (omited in Figure 2.5 scheme). The *gradient force* is caused by the laser beam, which polarizes the object. This force points in the direction of the intensity gradient (illustrated by the big arrow in Figure 2.5a and white arrows in Figure 2.5b).

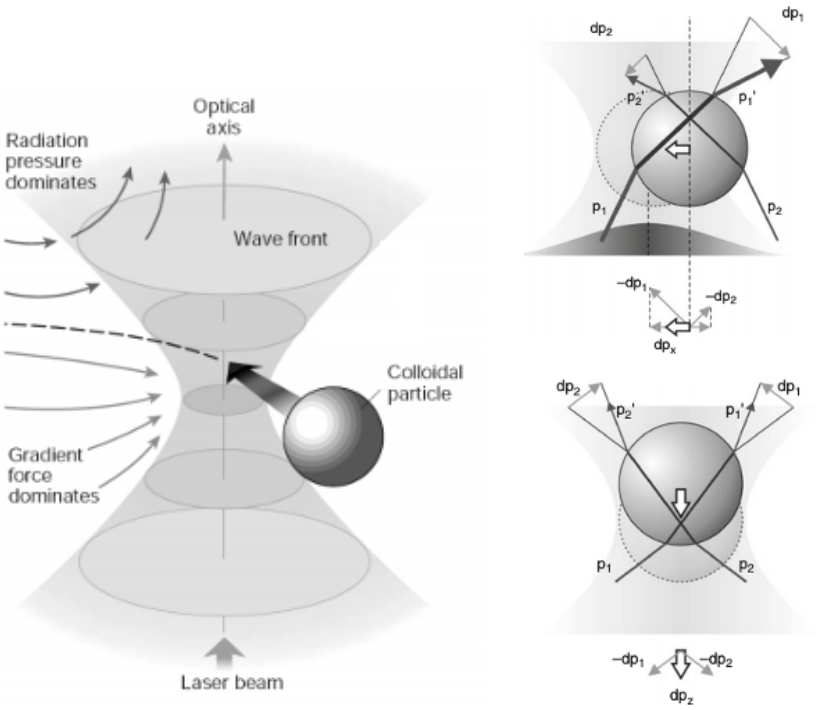

(a) Optical forces around the focus spot.

(b) Forces on an optically trapped particle in the ray-optics regime.

Figure 2.5: Intensity gradients in the converging beam draw small objects toward the focus, whereas the radiation pressure of the beam tends to blow them down the optical axis. (b) Lateral gradient force of a Gaussian laser beam profile (top) and axial gradient force toward the focus of the trapping light (bottom). The white arrows indicate the net restoring force. Adapted from [90].

The *scattering force* is the resulting force from several events in which the incident radiation is absorbed and isotropically reemitted by atoms or molecules. This force is given by [91]:

$$F_{scat} = n_m \frac{\sigma \langle S \rangle}{c}, \tag{2.12}$$

where n_m if the refractive index of the surrounding medium, $\langle S \rangle$ is the time averaged Poynting vector, c is the speed of light and σ is the particle's cross section, which in case of a spherical particle is defined by:

$$\sigma = \frac{8}{3}\pi (kr)^4 r^2 \left(\frac{n^2 - 1}{n^2 + 2} \right)^2, \tag{2.13}$$

with the particle radius r, the refractive index n of the particle and the wavevector k of the impinging light. The scattering force alone, would cause the object to be propelled out of the focus. The object is stably trapped only if the scattering force is compensated by the *gradient force* along the opposite direction. To achieve this, a significant fraction of the incident light should come in at large

angles, calling for a tightly focused trapping light source typically obtained by using a microscope objective with high numerical aperture (NA) [88]. In this regime, the particle is approximated to a dielectric sphere and the key parameters influencing the force of the trap are the light intensity, the refractive indexes of both particle and medium, the cross-section of the sphere and its radius [91].

Mie Regime

Also called Ray Regime, it assumes that size of the object is much larger than the wavelength of the light ($D >> \lambda$) and a single beam can be tracked throughout the particle. The incident laser beam can be decomposed into individual rays with appropriate intensity, momentum, and direction. These rays propagate in a straight line in uniform, non dispersive media and can be described by geometrical optics.

After a light ray traveled through the particle, its momentum has changed in direction and magnitude. The momentum difference is picked up by the particle. The force due to the directional change of a ray's momentum has components in the forward direction as well as to the side. However, there are many rays incident on the particle. The net force has only a forward component due to the rotational symmetry of the problem. This symmetry is broken if the particle is not centered exactly on the optical axis of the Gaussian beam. In this case the particle feels a restoring force.

Figure 2.5b qualitatively depicts the predominant trapping forces in this regime. Consider that the rays p_1 and p_2 in the top insert of Figure 2.5b have different intensities, so the momentum changes of these rays (dp_1 and dp_2, respectively) differ in magnitude, causing a net reaction force on the refracting medium in the direction of highest intensity. The x-projection of this force, dp_x, tends to counteract a displacement from the laser beam axis, pulling the particle towards the center of the beam. The axial gradient force is similarly caused by a momentum transfer upon refraction, resulting in a restoring force toward the focus, as in the bottom insert of Figure 2.5b.

Intermediated Regime

When the particle dimensions are comparable with the laser wavelength, the intermediate regime, a complete wave-optical modelling of the particle-light interaction is necessary for calculating the optical forces. For spherical particles, the Lorenz-Mie theory can be used to generate accurate numerical results for essentially any size and refractive index [92–94]. However, this model does not fit for non-spherical particles e. g.elongated particles, optically anisotropic particles, and inhomogeneous particles [94]. Moreover, in optical trapping experiments complex objects from tens of nanometers to tens of micrometers are manipulated, and cells, biological structures, metallic, dielectric, or hybrid

structures are often far from the two extreme regimes. In such cases, the dipole approximation can be used [95].

An optical trap forms a three-dimensional potential well for the trapped particle. This means that the total force acting on the particle is the sum of all the contributions from each ray forming the beam. The particle experiences an attractive force toward the potential minimum, which is located at a stable position where the trapped particle experiences no net force. Close to the potential minimum, the trap can be approximated to be harmonic, e. g., the attractive force F is directly proportional to the displacement x of the particle according to Hooke's law:

$$F = -k_s x \tag{2.14}$$

where k_s is the spring constant or trap stiffness in the x direction and the origin of the axis is taken at the trap equilibrium position. A calculation or measurement of the spring constants in the three orthogonal directions gives a calibration of the optical trap [88]. Using a laser of $1\,W$, the typical trap stiffness that can be obtained in a single-beam optical trap is in the order of $100\,pN/\mu m$.

2.2.3 *Optical Tweezers for Nanomechanical Characterization of Biological Samples*

OTs have now been widely employed in biology as a tool to actively probe, manipulate, and position biological systems or to measure mechanical properties from the nanoscale to microscale [96]. A particular advantage of the use of OTs in biology is that it is a noncontact method, where forces on the order of piconewtons can be applied very precisely in vivo and without any mechanical contact [97]. In addition, the information contained in the light used for optical manipulation can be used to quantify physical parameters such as forces, viscosity, and elasticity with exceptionally small forces and broad timescales ($0.1\,ms - 3,000s$) [98]. Subsequent responses of any biological system to optical forces can be measured with high precision - forces down to femtonewtons and displacements down to a single angstrom [98].

The characteristics of the mechanical deformation of living cells are known to strongly influence their functions, and their inability to deform sufficiently can contribute to a number of diseases [99]. Red blood cells (RBCs) are a good example of cells whose shape flexibility is essential to the organism and its function: their average diameter is about $8\,\mu m$, but they deform to fit through capillaries as narrow as $3\,\mu m$ in diameter [17]. OT has been widely used to perform mechanical characterization of RBCs [14, 100, 101] and to investigate the hydrodynamics effects on the biomechanical properties of its membrane under physiological flow and temperature changes [102, 103]. The current state of blood cell research by optical tweezers has been thoroughly covered in this

recent review [104].

In the results section of this thesis, a novel optical tweezer OT approach is applied, complementarily to DHM, to measure the deformation and elasticity of single RBCs trapped away from the coverslip. The cells membrane properties dependence on its lipid content were investigated in two different culture conditions.

2.3 STIMULATED EMISSION DEPLETION MICROSCOPY (STED)

2.3.1 *Super-resolution Microscopy and the Diffraction Limit*

The ability to investigate samples, using an imaging system with high resolving power able to read out information about the structure and dynamics of the sample, has always been desired in the field of natural sciences. Thus, since Ernst Abbe discovered in 1873 that the resolution of an optical system is limited by diffraction, there have been a lot of attempts to go beyond this resolution limit. Abbe stated that the resolution of an optical microscope cannot be arbitrarily improved but is subject to a fundamental limit, the so-called diffraction limit [105]:

$$r = \frac{\lambda}{2n \sin \alpha} \approx \frac{\lambda}{2NA} \tag{2.15}$$

where r is the resolution (the minimum distance between two point objects which can be resolved by the microscope), λ is the wavelength of the illuminating light, n is the refractive index of the medium between the specimen and the objective lens, $\sin \alpha$ is the semi-angle aperture of the objective lens, and NA its numerical aperture. Along the optic axis, the maximum achievable resolution is even poorer, being it related to the square of $\sin \alpha$.

The resolution limit in Equation 2.15 rules for incoherent illumination. In coherent-based imaging systems, the diffraction limit if often specified as [106]:

$$\frac{k\lambda}{NA} \tag{2.16}$$

where k is equal to 0.82 for coherent imaging systems with circular aperture. In practice, the resolution of an imaging system is not only limited to the diffraction resolution, which is related to the optical system. When the light is captured by a digital detector, (typically a CCD or CMOS camera), the spatial information regarding the optical signal is also distorted since the camera's pixels have a finite nonzero size. After that, the optical signal is converted in discrete electronic signal, and the quality of the detector including sensitivity, dynamic range, and different types of noise will also affect the final resolution [107]. Thus, the efforts to have a super-resolved microscope should address all these issues.

In some labeling microscopic techniques, such as fluoresce microscopy, the system resolution depends further on the labeling procedures and proper the working of the labels itself. However, what can be seen as an additional constraint to obtain superresolution microscopy, has actually been used to "break" the diffraction limit [108].

Although there are many label-free optical superresolution techniques [109], including digital holographic microscopy [66], in some cases, to image specific structures within intact cells, such as the proteins, labeling is unavoidable. In the following section, I will briefly introduce STimulated Emission Depletion (STED) microscopy, a fluorescence microscopic technique, which overcomes the diffraction limit. This technique was used in this work to investigate the structural arrangement of nuclear Lamin and its influence in the nuclear morphology of neutrophils precursors. The results will be presented in Chapter 5.

2.3.2 *Principle of STED*

STimulated Emission Depletion (STED) microscopy was first proposed in 1994 by Stefan Hell and Jan Wichmann [108]. Five years later, the concept was experimentally demonstrated by Thomas Klar and Stefan Hell in 1999 [110]. Although being a relatively new technique, realised less than 20 years ago, yet, more than 600 publications deal with STED [111], showing its potential to become a standard method for studying subcellular structures on the nanoscale.

In conventional optical microscopy, features bellow the diffraction limit can not be resolved. This holds true also for classical diffraction-limited fluorescence microcopy, where the emitters spaced by less than the diffraction limit cannot be individually distinguished. STED microscopy overcomes this diffraction limit by reversibly silencing (depleting) fluorophores at predefined positions of the diffraction-limited excitation regions. Only the non silenced fluorophores in the complementary regions emit light, allowing features closer than the diffraction limit to be separated [112].

The fluorophores are excited by a standard excitation laser (depicted in the three drawings in Figure 2.6). The STED beam implements a focal switch between S_1 (A) and S_0 (B) states induced via stimulated emission. During stimulated emission, an incoming photon, matching the emitters emission spectrum, forces an electronically excited energy state, S_1, to de-excite (within subpicoseconds) via the emission of a second photon having the same phase, frequency, polarization and direction as the stimulating photon [111]. In contrast, spontaneous emission occurs stochastically during the lifetime of the excited state S_1. The process of stimulated emission effectively depletes the fluorophores in the doughnut region, leaving only the flourophores close to the 'zero'-intensity point able to fluoresce.

In a standard 2D STED implementation, the excitation beam is Gaussian shaped and overlaid with the red-shifted, STED beam, which confines the

effective excitation. The STED beam is responsible to de-excite fluorophores via stimulated emission and it has a doughnut-shaped focal intensity distribution with 'zero'-intensity point in the center as shown in Figure 2.6.

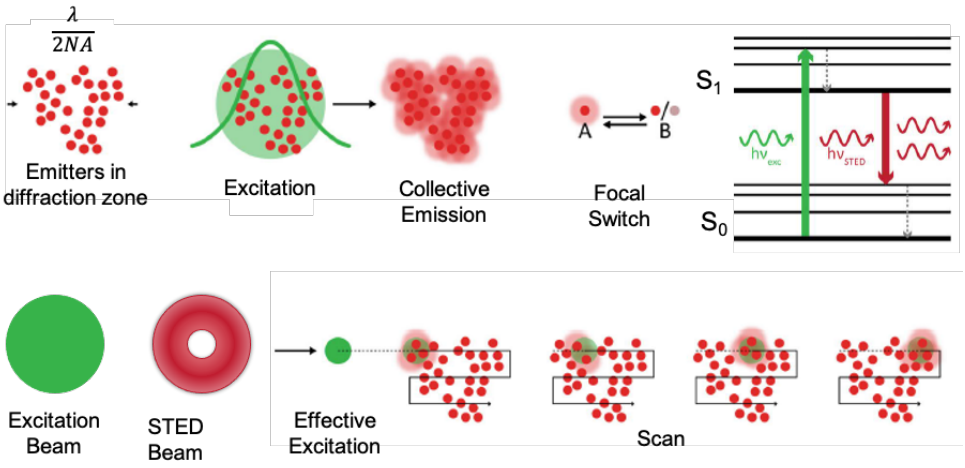

Figure 2.6: All the emitters within the diffraction zone are excited by the excitation beam (in green). The STED beam is responsible to create a focal switch, where the molecules within its region are depleted by stimulation emission. The co-aligned beams scan the sample to form a super-resolved image. Adapted from [111].

Although the STED beam is still diffraction limited, the 'zero'-intensity point in the center has a subdiffraction size and decreases with increasing STED beam intensity. The co-aligned beams (excitation and STED) scans together across a specimen, resulting in an image where the (subdiffraction) spatial resolution is given by the size of the effective fluorescent region around the 'zero' [112].

The increase in the spatial resolution is dependent on the STED excitation intensity and can be described mathematically as:

$$\Delta r \approx \frac{\lambda}{2\mathrm{NA}} \frac{1}{\sqrt{I_{\mathrm{STED}}^{\mathrm{max}} / I_{\mathrm{sat}} + 1}} \tag{2.17}$$

The resolution of STED is an extension of Abbe's equation for diffraction limited systems. It scales inversely with the square-root of the ratio between the maximum intensity at the doughnut crest $I_{\mathrm{STED}}^{\mathrm{max}}$ and the fuorophore characteristic threshold intensity I_{sat}. Theoretically, the resolution of STED microscopy can reach the molecule's size (the ultimate limit of a fluorescent microscope). However, in practice, it is limited by the signal-to-noise ratio (SNR)[113]. To obtain an effective resolution enhancement, it is important to both generate subdiffraction fluorescent regions across the whole specimen (according to the Nyquist sampling condition) and to register, from all these regions, enough fluorescent photons to obtain good SNR.

STED imaging allows the visualization of cellular structures with an effective image resolution of down to $20\,nm$ [114], and has opened up avenues for new biological discoveries [115]. To further understand the mechanisms behind nuclear

morphological changes, STED will be applied in this Thesis to visualize the supramolecular structures of lamins in the nuclear membrane of promyelocytes (neutrophil precursors). Although this Thesis is mainly focused on label-free techniques, the use of labels is required to target lamins proteins.

GOAL OF THE THESIS

The goal of this Thesis is to propose new applications of label-free markers at nanoscale for liquid biopsy using multimodal optical microscopy techniques.

The term liquid biopsy will be used with its extended meaning referring to the analysis of cells which can be found in some body fluids, as red blood cells and neutrophils in blood; neutrophil precursors in fluid bone marrow; leukocytes and bacteria in urine. On the other hand, multimodal microscopy refers to the use of more than one microscopic technique in the investigation of the same object of study.

Since Digital Holographic Microscopy (DHM) is intrinsically label-free and suitable for both high throughput and fast screening, it is the most used technique in this thesis, followed by Optical Tweezers (OTs). Other complementary techniques, as Differential interference contrast microscopy (DIC) and standard Fluorescence Microscopy (FL) were also employed for comparison purposes. Further, Stimulated Emission Depletion (STED) Microscopy was applied to investigate the structural basis of the nuclear shape as morphological marker.

The next part of the Thesis is organized as follows: in the results part, I will present three main applications where DHM and OT were used to extract label-free markers to address issues in the biomedical field in both research (for single cell characterization of Red Blood Cells and Neutrophil precursors) and clinical (fast screening for urinalysis) contexts. In the last chapter of results part, STED microscopy is used to investigate deeper the nuclear morphology by characterizing a structural protein in the nuclear membrane of neutrophils precursors during differentiation.

Finally, in the conclusion, I will summarize how the potential label-free markers suggested for each mentioned application can be explored for liquid biopsy. In addition, I will precis why nuclear morphology is a suitable label-free marker, based on the organization of lamins proteins in the nuclear membrane at a supramolecular level.

Part II

RESULTS AND CONCLUSION

The morphological and mechanical properties of living cells reflect complex functionally-associated processes. Monitoring these modifications with a label-free approach can provide a direct information on the cellular functional state which further could be used for screening and diagnosis purposes.

In this part, I report two different applications of label-free microscopic techniques to derive morphological and mechanical parameters from living cells for both single cell and wide field conditions. These parameters have been used as markers to compare between ex-vivo and cultured red blood cells in Chapter 3 and to characterize neutrophil differentiation Chapter 4 .

In Chapter 5, super-resolution STED microscopy was applied to follow structural arrangement of lamins in the nuclear membrane of neutrophil precursors under differentiation. Then, in Chapter 6, the usage of DHM to perform fast screening urine biopsy, using cell morphology as a marker, is described. Lastly, in Chapter 7, I'll summarize the main outcomes of the thesis and propose further applications for the presented label free-markers in the field of liquid biopsy.

3

BIOMECHANICAL MARKERS FOR RED BLOOD CELLS CHARACTERIZATION

3.1 INTRODUCTION/ MOTIVATION

The mechanical properties of erythrocytes are critical for maintaining cell functions and their changes are strictly associated with its maturation process from reticulocytes [116]. There is a worldwide effort to generate ex vivo cultured red blood cells (cRBCs) from different sources [117–119] for broad clinical application by using a near universal RBC phenotype. However, in ex vivo, the triggers to terminal maturation from enucleated lobular reticulocytes to biconcave erythrocytes remain elusive to date [120].

Mature RBCs demonstrate a remarkable deformability when subjected to mechanical stresses [121]. This allows them to pass through capillaries with diameter smaller than the RBC diameter at rest and restore to original shape when they leave. The deformability of RBCs plays an important role in their main function (transport or respiratory gases in the human body), therefore, it represents a natural choice to compare ex vivo cultured red blood cells versus native RBCs.

During the past years, various experimental techniques have been developed to measure cell deformability and related biomechanical parameters for individual RBCs. They include, but are not limited to: micropipette aspiration, atomic force microscopy, optical tweezers (OT), magnetic tweezers, digital holographic microscopy (DHM), dynamic light scattering, ektacytometry, microfluidics, thoroughly discussed in several reviews [122]. DHM and OT were used to characterize ex-vivo generated and native RBCs observing the membrane deformability, associated to fluctuations, and cell morphology. DHM was employed to extract cell morphology and cell membrane fluctuations of RBCs settled on a planar surface. Complementarily, single beam OTs was used to observe the cell membrane fluctuations for suspended cells and cell deformability when it is subjected to forces similar to the ones undergone in blood vessels, i. e., from less than $1\,pN$ to $90\,pN$ [84, 123].

3.2 MATERIALS AND METHODS

3.2.1 *Cell Preparation*

The cells were prepared by the group of Claudia Bernecker from the Clinical Department of Blood Group Serology and Transfusion Medicine from the Medical University of Graz. All the preparation procedure is detailed in [17]

and have been transcribed here:

Human native erythrocytes (nRBCs) were obtained from fresh RBC units within 24 h. CD34+ cells were isolated from peripheral blood (purity $97.8 \pm 0.5\%$) with the CD34 Microbead Ultrapure Kit (Miltenyi Biotec, Bergisch-Gladbach, Germany). Prior to sampling, written informed consent was obtained from volunteer donors. The study was approved by the local ethics committee of the Medical University of Graz, Austria in line with the Declaration of Helsinki (EK 27 165ex 14/15). Erythroid differentiation from CD34+ hematopoietic stem/progenitor cells (HSPCs) was conducted according to the established three-phase culture model [124]. Iscove's basal medium (Biochrome, Berlin, Germany) was supplemented with 5% human plasma (Octapharma, Vienna, Austria) (cRBCPlasma), or 2.5% human platelet lysate (cRBCHPL) (in-house production) from day 8 onwards. All media were supplemented with $10 g/mL$ insulin (Sigma Aldrich, St. Louis, MO, USA) and $330 g/mL$ human holo-transferrin (BBI solutions, Crumlin, UK). Cell differentiation was induced with $100 ng/mL$ stem cell factor (SCF), $5 ng/mL$ interleukin-3 (IL-3) (both PeproTech, Rocky Hill, NJ, USA) and $3 U/mL$ erythropoietin (EPO) (Erypo, Janssen Biologics B.V., Leiden, The Netherlands) and $10^{-6} M$ hydrocortisone (SigmaAldrich, St. Louis, MO, USA). Erythroid differentiation was monitored microscopically with May-Giemsa-Gruenwald (Hemafix, Biomed, Oberschleissheim,Germany) and neutral benzidine co-staining (o-dianisidine, SigmaAldrich, St. Louis, MO, USA). Additionally, the maturation stages were confirmed by flow cytometry CD36, GPA (Beckman Coulter, Brea, California, USA); CD45, CD71 (Becton Dickinson, Franklin Lakes, NJ, USA)) on a CytoFLEX flow cytometer (Beckman Coulter, Brea, CA, USA). Dead cells were excluded by co-staining with 4,6-diamidino-2-phenylindole (DAPI; ThermoFisher, Waltham, MA, USA). After 18 days of differentiation, cells were filtered through a syringe filter (Acrodisc WBC syringe filter, Pall, Port Washington, NY, USA) to obtain the pure enucleated cRBC fraction free of precursors and expelled nuclei. Enucleated cRBCs were further characterized microscopically by new methylene blue staining for ribosomal residues (reticulocyte stain, Sigma-Aldrich, St. Louis, MO, USA) and flow cytometry for CD71 expression and on the basis of thiazole orange stain (ReticCount, Beckton Dickinson, Franklin Lakes, NJ, USA). Before the measurements, the cells were diluted in Phosphate-buffered saline buffer (pH 7.4) and then measured at room temperature.

3.2.2 *Cell Deformation and Cell Membrane Fluctuations in an Oscillatory Optical Trap*

Cell deformation and cell membrane fluctuations of single erythrocytes confined in an optical trap were investigated using custom-built oscillatory optical tweezers (OOTs). The setup is schematically represented in figure 3.1. It is based on the modular Thorlabs OT kit (OTKB, Thorlabs Inc., Newton, NJ, USA) with some modifications to allow probing cell biomechanics with silica microbeads [125, 126]. To investigate cell deformation under optical forces,

here, we trapped and manipulated the cell directly. The trapping laser (YLM-5, IPG Photonics GmbH, Oxford, Massachusetts, USA) is a continuous wave (CW) infrared (IR) fiber laser at $1064\,nm$ and the optical trap can be moved axially in a range of $\pm 8\,\mu m$ from the laser focus, by using a focus tunable lens (FTL) (EL-10-30-NIR-LD, Optotune AG, Dietikon, Switzerland).The power of the IR laser at the sample was kept between $10\,mW$ and $30\,mW$, allowing trapping without damaging. A high numerical aperture microscope lens (ML) is used for trapping and imaging (Nikon, NA 1.25, 100X, oil immersion, Nikon, Tokio, Japan) and a tube lens ($f = 200\,mm$) for projecting the image on the Complementary Metal-Oxide-Semiconductor (CMOS) camera (DCU224M, Thorlabs Inc.). After cell identification, the trapping laser was switched on and the cell was picked up into the optical trap, positioned at a height $H \approx 20\,\mu m$ from the coverslip. The cell was kept in the fixed optical trap for $10\,s$, then the trap was moved along the optical axis in an oscillatory movement with frequency $f = 0.75\,Hz$ and amplitude $A = 5\,\mu m$ (for $10, s$), followed by a second oscillatory movement with higher amplitude $A = 7\,\mu m$(for 10 s). Finally, by switching the laser off, the cell was released from the trap. Notice that using the FTL, the trapped cell can be shifted up and down without the need to change the position of the microscope objective. Cell trapping, folding and shape recovery were monitored with time-lapse microscopy, recording at 11 frames per second.

Cell membrane fluctuations are investigated using the interference pattern formed by the laser light scattered forward by the cell, collected by a microscope lens (Nikon, NA 0.3, 10X, not shown in Figure 1) and projected on a quadrant photo detector QPD (PDQ80A, Thorlabs Inc.) by a positive lens ($f = 40\,mm$, Thorlabs Inc., not shown). The QPD allows for recording the intensity fluctuations of the light with a $5\,kHz$ frequency bandwidth. The variance (σ^2) and the power spectrum density (PSD) are calculated for the intensity fluctuation signal $S(t)$ acquired by the QPD and given in mV:

$$\sigma^2 =< S^2(t) > \tag{3.1}$$

$$PSD(f) = FTR_S(\tau) \tag{3.2}$$

where $R_S(\tau) =< S(t) \cdot S(t-\tau) >$ is the autocorrelation function, FT is the Fourier transform and f is the frequency variable. The variance σ^2 is the value of the autocorrelation function at delay $\tau = 0$ and shows how much the signal values are spread from the mean value, while the PSD is a measure of the signal's power content versus frequency. The signal $S(t)$, the variance σ^2 and the power spectrum density PSD are processed using custom Matlab code (Matlab R2017b, MathWorks, Natick, MA, USA).

3.2.3 *Quantitative Phase Imaging with Digital Holographic Microscopy*

The cell height is obtained by numerical reconstruction of a recorded hologram using DHM. The setup is represented schematically in Figure 3.2. It is based

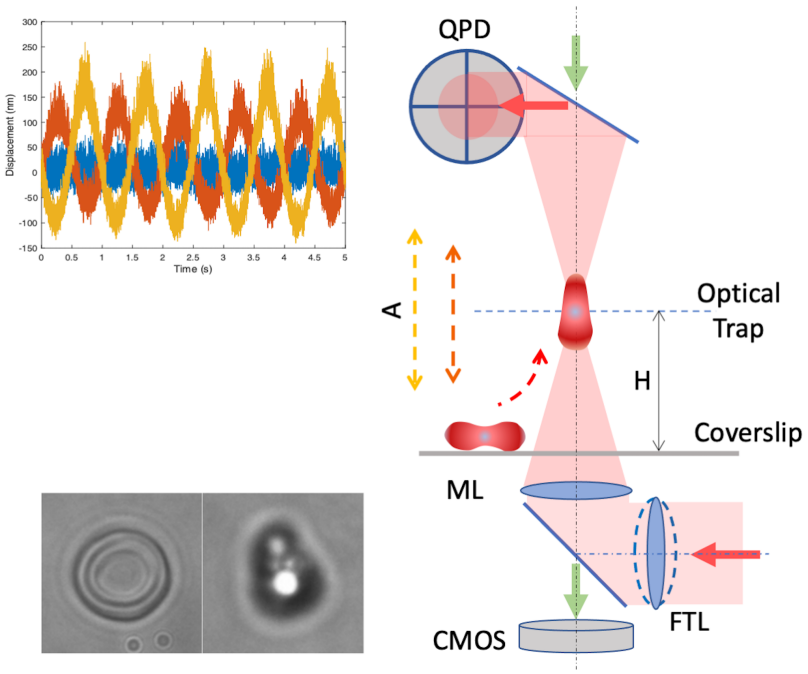

Figure 3.1: The RBC is picked up from the coverslip into the optical trap by the trapping IR laser (red arrows). Cell imaging (down left inset) by the microscope lens (ML) on the sensor of a CMOS camera by up-down illumination (green arrows) while the intensity fluctuations of the light scattered by the cell are recorded on the QPD (top left inset). Using the Focus Tunable Lens (FTL), the position of the optical trap is moved vertically in an oscillatory motion (lens with dotted line illustrates the change of the FTL curvature.

on a Mach-Zender interferometer adapted to a custom inverted microscope [68, 127]. The laser beam (520 nm, max 20 mW) from a diode laser (LP520-SF15, Thorlabs Inc.) is split into two beams: one passes through the RBC and one is used as a reference. The beam passing through the sample is again collimated and the two beams are then recombined to form an interference pattern on the sensor of the CMOS camera (CS235MU, Thorlabs Inc). The power of the laser beam at the sample was less than 1 mW. The 3D profile of the RBC is obtained by numerically processing the digital hologram with custom Matlab algorithms (MathWorks.com). The CMOS sensor works at a 110 fps frame rate (exposure time: 9 ms), recording holographic movies from which cell membrane fluctuations are measured.

The height h at the point (x,y) of the RBC is calculated using the formula [127]:

$$h(x,y) = \frac{\lambda \cdot OPD(x,y)}{2\pi \cdot (n_c - n_m)} \tag{3.3}$$

where λ is the wavelength of the light ($\lambda = 520\,nm$), $OPD(x,y)$ is the optical path difference obtained from hologram reconstruction, n_c is the refractive index

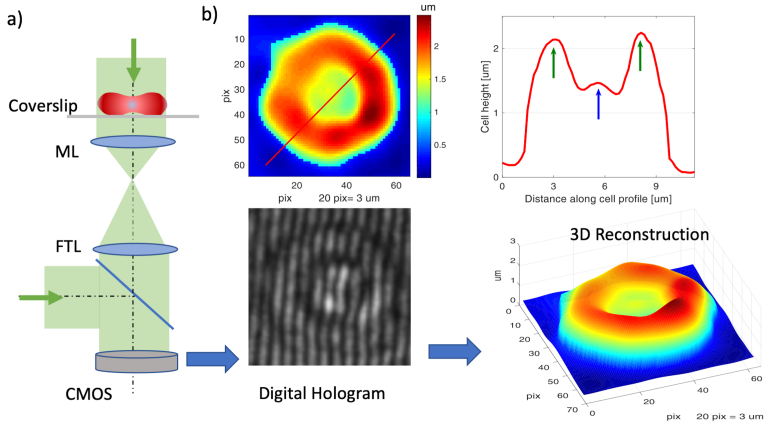

Figure 3.2: Schematic of the DHM setup. Green arrows: laser beam; ML: Microscope Lens, TL: tube lens, CMOS: camera sensor. Digital Hologram on CMOS and 3D Reconstruction (bottom). Height profile of the cell (top right) along the red line shown in reconstruction (top left).

of RBC ($n_c = 1.4184$), n_m is the refractive index of the medium ($n_m = 1.33$). The refractive index n_c is considered the same for all the RBC types analyzed hereafter [127].

An example of a digital hologram and its reconstruction is shown in figure figure 3.2b for a native RBC (nRBC). The diameter of the cell about $7 - 9\mu m$, in agreement with the size measured with normal bright field microscopy. The additional information by DHM is the cell height, obtained with equation 3.3. A height profile is taken along the red line and represented in figure figure 3.2b, showing the characteristic profile for RBC height, with a dimple in the center. The max cell height is $2.3\,\mu m$, while the height at the dimple is $1.4\,\mu m$, giving a sphericity coefficient of $CS = 1.4/2.3 = 0.61$.

3.2.4 *Cell Morphological Parameters and Cell Membrane Fluctuation*

Using DHM, we measured morphological parameters and cell membrane fluctuations. The holographic reconstruction of the DHM of the cell from a single frame is enough to derive the morphological parameters:

CELL PROJECTED AREA (CA):

$$CA = N_p \cdot pa \tag{3.4}$$

where N_p is the number of pixels inside the cell area and pa is the pixel area (for an effective pixel size of $p = 4.8\,\mu m/33 \approx 0.15\,\mu m$, the square pixel is $pa = 0.0225\,\mu m^2$).

CELL VOLUME (CV):

$$CV = pa \sum_i h_i \tag{3.5}$$

CV is calculated by summing the volume corresponding to all the pixels within the cell area.

CELL EQUIVALENT HEIGHT (HM):

$$hm = \frac{CV}{CA} \tag{3.6}$$

is the mean height of the cell assuming the cell was a cylinder with CA, the cell projected area.

CELL SPHERICITY, (CS):

$$CS = \frac{hD}{hR} \tag{3.7}$$

where hR is the cell height at the ring and hD is the height at the dimple (see the green and blue arrows in figure 3.2). The cell sphericity is a shape parameter which helps to evaluate if the cell is biconcave or spherocyte-like. The ring region is the region where the cell height is maximum. The diameter of the ring is about half the diameter of the cell. In practice, we sample the ring for cell height for $n = 8$ points and the dimple for $n = 3$ points and we calculate hR and hD as the mean of these values.

MEAN CORPUSCULAR HEMOGLOBIN (MCH):

$$MCH = \frac{10 \cdot mPhase \cdot \lambda \cdot CA}{2\pi \cdot \alpha_{Hb}} \tag{3.8}$$

where $mPhase$ is the mean phase value over the cell projected area CA and $\alpha_{Hb} = 1.96\,\mu m^3/pg$ is a constant known as a specific refraction increment related mainly to the protein concentration [127].

CELL MEMBRANE FLUCTUATION (CMF): To determine CMF, we calculated, for each pixel within the cell, the fluctuation of the cell height in time ($t > 1\,s$ at 110 fps) and the corresponding standard deviation for each pixel of the cell, STD_{pix_i} [127]. The CMF value is calculated as the mean of STD_{pix} [127].

$$CMF = \frac{1}{N_p} \sum_i STD_{pix_i} \tag{3.9}$$

3.3 RESULTS AND DISCUSSION

Cell membrane fluctuations and deformability, together with morphological parameters were used as biomechanical and morphological markers to compare ex-vivo differentiated $cRBC^{Plasma}$ and $cRBC^{HPL}$ with native $RBCs$. Two label-free microscopy techniques: OT and DHM, were used to characterize the cells as described in Section 3.2. Cultured RBC^{Plasma} and RBC^{HPL} were differentiated ex vivo as detailed in [17].

3.3.1 *Cell Membrane Fluctuations of Native vs. Ex Vivo-Generated RBCs Measured by DHM*

The cell membrane fluctuations were measured as mentioned in 3.2.4. To confirm that the membrane fluctuations were not due to background noise, the standard deviation of the optical path difference (OPD) of regions within and out the cell were measured. Three randomly chosen pixels were used to evaluate the OPD: one on cell simple, one on the cell ring and on background, as shown in figure 3.3. The standard deviations of the region within the cell (ring $0.053\,rad$ and dimple $0.051\,rad$) were two times higher than the background ($0.028\,rad$), indicating that the membrane fluctuation signals were reliably.

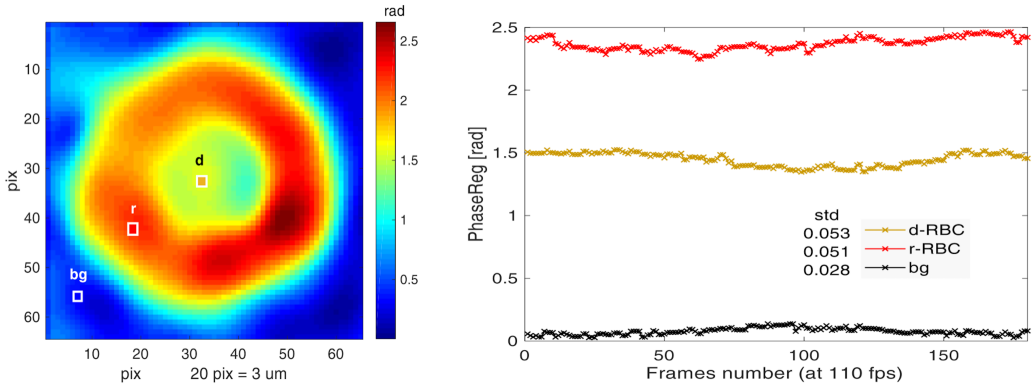

Figure 3.3: RBC OPD map with three points chosen randomly: ring, dimple, background (left). OPD fluctuations recorded for t > 1s and standard deviation calculated for each chosen point (right).

To confirm the validity on the OPD fluctuation measurements, the height fluctuations at each pixel of the cell were calculated using Equation 3.6. The standard deviation of the height fluctuations was then calculated for each pixel, resulting on a fluctuation map over the cell, shown in Figure 3.4 for the case of a native RBC. The standard deviation of each pixel varies over different regions of the cell, with values ranging from 10 to $28\,nm$. To represente the CMFs for the whole cell in a single value, the mean value of the standard deviation for all the pixels within the cell (Equation 3.9) was calculated. A high CMF value is associated with high membrane flickering/flexibility.

The results obtained for the three types of cells are presented in Table 3.1. The CMF amplitude of the nRBCs is the highest, followed by $cRBC^{Plasma}$ and then by $cRBC^{HPL}$. Analyzing how the CMF correlates with morphological factors as done in [127], we find that the CMF exhibits a negative correlation with the sphericity coefficient CS projected area CA and CV for $nRBCs$ and $cRBC^{HPL}$, revealing results which are in line with the CMF analysis of stored RBCs [127]. The CMF amplitude of the $cRBC^{Plasma}$ does not follow this trend.

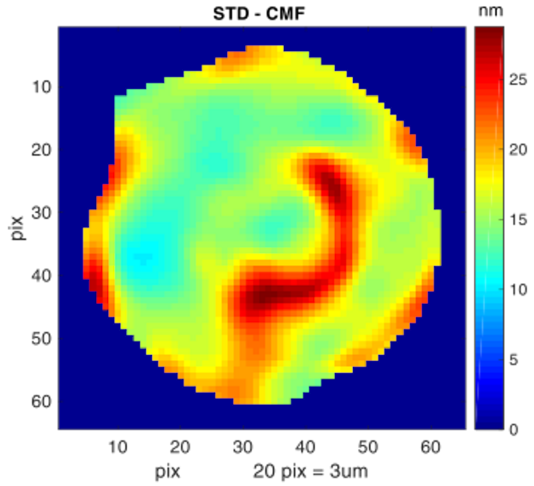

Figure 3.4: Standard deviation distribution over the cell area.

Table 3.1: The height normalization coefficient, c is calculated using the mean height, hm, given in Table 3.2. Corrected CMF is obtained from measured CMF divided by the normalization coefficient c.

CMF		Measured Cell		Background		Height Normalization	Cell Corrected
		mean	std	mean	std	c	mean
cells	n	nm	nm	nm	nm	-	nm
nRBC	25	54,4	10,8	24,7	6,2	1,00	54,47
cRBCPlasma	24	53,8	21,4	25,3	9,1	1,78	30,27
cRBCHPL	29	37,9	14,3	19,4	7,9	0,89	42,61

The measurements results using OOTs indicated that $nRBCs$ are the most flexible and $cRBC^{Plasma}$ the least, with $cRBC^{HPL}$ in between. This difference regarding the DHM measurement might be related to subtle dissimilarities of the cytoplasm composition for different types of cells, and the fact that in DHM the cell height is derived from the phase retardation of the light passing through the cell [17]. If the measured CMF is normalized by the cell height $c = hm_{RBC-Type}/hm_{nRBC}$, the CMF values can be rearranged in a sequence following the expected trend.

3.3.2 *Morphological Parameters of Native vs. Ex Vivo-Generated RBCs Measured by DHM*

The morphological characterizaton of the three cell types: $nRBCs$, $cRBC^{Plasma}$ and $cRBC^{HPL}$ was done as described in Section 3.2 and the results are present in Table 3.2.

Table 3.2: Cell morphology parameters. CA: Cell Area; CV: Cell Volume; CS: Cell Sphericity coefficient; MCH: Mean Corpuscular Hemoglobin; hm: equivalent cell height.

Morphology		CA	CV	CS	MCH	hm
		mean ± std	mean ± std	mean ± std	mean ± std	mean
Cells	n	μm^2	μm^3(or fL)	-	Picogram [pg]	μm
$nRBC$	25	55,42 ± 9,2	95,2 ± 16,6	0,57 ± 0,1	25,24 ± 5	1,72 ± 0.4
$cRBC^{Plasma}$	24	41,05 ± 14,4	125,5 ± 43,3	1,04 ± 0,1	31,17 ± 11,7	3,06±0.6
$cRBC^{HPL}$	29	70 ± 21,7	107,1 ± 37,8	0,671 ± 0,4	28,1 ± 10,9	1,53± 0.3

The smallest projected area corresponded to the $cRBC^{Plasma}$ ($CA = 41.05\,\mu m^2$), which had also the highest sphericity coefficient $CS = 1.04$ and second highest volume $CV = 125.5\,\mu m^3$ (or fL). Although the projected area CA is small, the volume CV for $cRBC^{Plasma}$ is big because of the cell shape. In fact, the shape of these cells is predominantly spherical-convex, different from the biconcave shape of the $nRBC$. Thus, the mean height for $cRBC^{Plasma}$ is also maximum among all the cell types ($hm = 3.06\,\mu m$), confirming this observation. The sphericity of $cRBC^{Plasma}$ cells was confirmed also by the optical tweezers OT experiments, where the $cRBC^{Plasma}$ cell was trapped without being deformed and maintaining its spherical symmetry (while $nRBC$ are clearly deformed by the OT forces, denoting that they are more deformable, see Section 3.3.3).

The biggest projected area CA was found for the $cRBC^{HPL}$ ($CA = 70\,\mu m^2$) though it is not associated with the biggest volume ($CV = 107.1 < 133.6\,\mu m^3$). This is due to the biconcave shape of the cell, as reflected also by the sphericity coefficient ($CS = 0.67$). From a morphological point of view for parameters: CV, CS, MCH and hm have similar values for $nRBC$ and $cRBC^{HPL}$. The difference in CA tells us that a $cRBC^{HPL}$ are slightly flattened than $nRBC$. The mean corpuscular hemoglobin (MCH) values of $cRBC^{HPL}$ and $nRBC$ are similar and confirmed the MCH values reported for $nRBC$ elsewhere [127].

3.3.3 *Cell Membrane Fluctuations of Native vs. Ex Vivo-Generated RBCs in OOTs*

Cell membrane fluctuations (CMF) were investigated measuring the intensity fluctuations of the intensity of laser light scattered by the RBC in the trap, as described in Section 3.2. The intensity fluctuations, $S(t)$ are due to two factors: 1) the displacement of the cell in the trap and 2) cell membrane flickering. Although these two components cannot be decoupled, the signal analysis might be useful if the goal is to compare the fluctuations for cells of similar size, for which the contribution of the first component is assumed to be comparable, while the contribution of the cell membrane fluctuations is predominant for

Table 3.3: Variance for cells in fixed and oscillating traps.

Variance	nRBC	cRBCPlasma	cRBCHPL
Mean / Std $[mV^2]$	(n= 32)	(n= 24)	(n= 30)
Fix trap	460 / 160	300 / 100	470 /140
Osc. $A = 5\,\mu m$	10800 / 5500	5600 / 1500	9200 / 5100
Osc. $A = 7\,\mu m$	22600 / 10800	11300 / 3100	19900 / 11600

the difference between different types of cells.

We acquired the signal $S(t)$ for the three cell types during the trapping experiments described above. The QPD signal $S(t)$ was sampled at $5\,kHz$. This is a large frequency bandwidth, thoroughly covering the frequency band of the cell fluctuations [21,24]. The variance (σ^2) of the signal $S(t)$ was first calculated for each RBC in fix static and oscillating trap and then the mean value and standard deviation of the variances for the same type of cells were determined. From the results obtained for the three types of $RBCs$, shown in Table 1, we found that the mean variances for $cRBC^{HPL}$ (n= 30 cells) and $nRBC$ (n=32 cells) are close and that both are higher than the mean variance for the cRBCPlasma (n=24 cells). Since a higher value of the variance is associated with higher CMF, this result shows that the CMF of $nRBC$ is similar to that of $cRBC^{HPL}$ and higher than that of $cRBC^{Plasma}$. Since not all the distributions are normally distributed, we also performed a Mann-Whitney U test. The variance distributions for each type of cells are represented graphically in Figure 4 together with the p values. The p values show a net difference between $nRBC$ and $cRBC^{Plasma}$, $cRBC^{HPL}$ and $cRBC^{Plasma}$, and a clear likeness between $nRBC$ and $cRBC^{HPL}$ This observation holds both for static and oscillating trap. Interestingly, the p-value between $nRBC$ and $cRBC^{HPL}$ decreases for oscillating trap, indicating a different behavior of the cells in movement. The variance for $nRBC$ is higher, suggesting that the cell membrane of $nRBC$ fluctuates more than $cRBC^{HPL}$ when the cell moves in fluid.

3.3.4 *OOTs Allow the Investigation of Cell Deformation under Forces of Similar Strength as Those on Cells in the Blood Stream*

A step forward towards the understanding if ex-vivo $cRBCs$ would be suitable to replace $nRBCs$ is to compare how such cells behave under forces similar as those in the blood stream. In OOTs, the radiation pressure of light interacts with the cell, inducing cell trapping and deformation without a mechanical contact. Optical trapping allows for studying the cell suspended in solution, away from the wall surfaces of the experimental chamber. The radiation pressure of

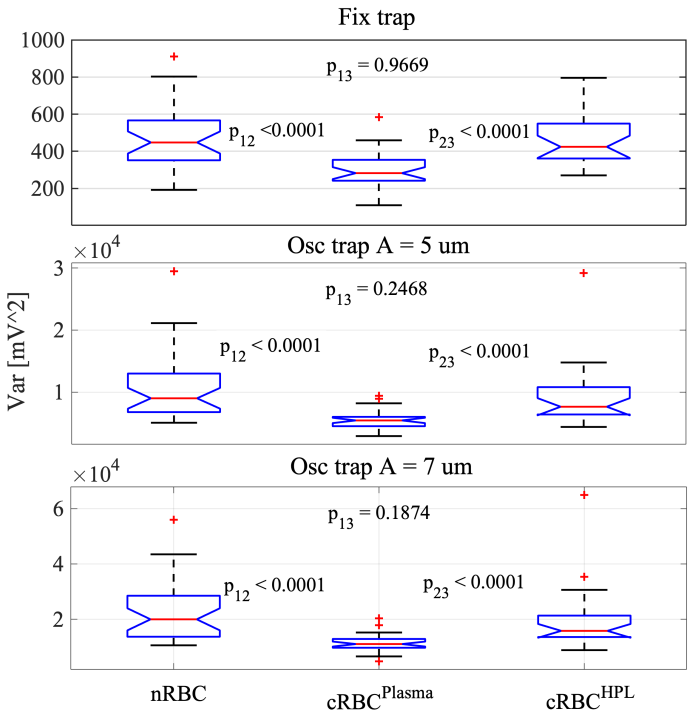

Figure 3.5: Variance results for $nRBCs$, $cRBC^{Plasma}$ and $cRBC^{HPL}$ for fixed and oscillating traps: $A = 5\mu m$ and $A = 7\mu m$,respectively. The distributions of the variance values for each cell type are represented graphically using the boxplot method. The p values are calculated with a Mann-Whitney U test.

light has a clepsydra-like shape, following the intensity's spatial distribution, with the highest pressure at the clepsydra neck (focus of the laser beam) [128]:

$$RP = n_m \times P/A/c \tag{3.10}$$

where n_m is the refractive index of the medium, A is the laser spot area and c if the speed of light in vacuum. Thus, if we consider a laser beam of power $P = 20\,mW$ focused through a high-numerical aperture lens ($NA = 1.25$) onto a focal spot of diameter $d \approx 0.6\,\mu m$, in a liquid chamber ($n_m \approx 1.33$), the radiation pressure in the focus is $RP_{max} \approx 300Pa$.

Step forward towards laboratorial investigation of the cells in the blood to perform detailed liquid biopsy (at single cell level, not high throughput) . Due to the light beam focusing through the high-NA lens, the radiation pressure rapidly drops along the optical axis, before and after the focus. For the above numerical values, which correspond to the OOT experimental setup, they result in an attenuation factor of $\approx 19 \times L^2$ for the radiation pressure, where L is the distance from the focus, expressed in microns. Considering the average diameter of an RBC is about $8\,\mu m$, the magnitude of the radiation pressure

at the extremities of cell in the optical trap ($L = \pm 4\,\mu m$) drops about 300 times to $RP_L = 1\,Pa$. The spatial distribution of the radiation pressure is symmetric and well controlled by the optical configuration. Therefore, the interaction between light and cell manifests in forces, which for a given value of the radiation pressure, depend only on the local material and morphological properties of the cell. A rough idea of the strength of forces locally acting on the cell is given by:

$$F = Q \times RP \times A_c \tag{3.11}$$

where A_c if the light-cell contact area and Q is a dimensionless coefficient, which considers the material and morphological properties of the cell [128, 129]. The value of Q ranges from 0.03 to about 0.3 for cells ($Q_{max} = 2$ for perfectly reflecting objects), meaning that for a contact area $A_c = 1\mu m^2$ the forces acting on the cell range from less than $1\,pN$ to $90\,pN$. The spatial distribution of these forces over the cell is neither homogeneous nor isotropic and hence they can induce cell folding and buckling.

3.3.5 *Mophological and Biomechanical markers for a faithful identification of native RBCs vs. cultured RBCs*

Due to its ability to reconstruct the 3D profile of the cell, DHM provides useful information on the cell morphology, complementary to the OOT approach. The cell volume, CV and the sphericity coefficient, CS are two important parameters to assess the morphologic similarity between native and generated erythrocytes.

Calculating the dry mass of the cell DHM allows to evaluate the mean corpuscular hemoglobin (MCH) which is another important parameter for erythrocyte characterization. The DHM method is quite simple and fast: tens of cells situated in a field of view of about $0.2 \times 0.2mm$ can be measured simultaneously in several seconds.

Cell membrane fluctuations (CMFs) can be measured at different points of the cell and averaged to get the CMF value for the entire cell. The result is expressed in terms of the standard deviation of the height fluctuations over all the cell pixels. The values obtained for nRBCs are in line with the results reported in the literature for $nRBCs$ [130] and allows the comparison of $nRBCs$ to generated $cRBCs$. For nRBCs and cRBCHPL, the results obtained by DHM (Table 3.2) follow the same trend as the results obtained by OOTs (Table 3.3). The complementarity of DHM to OOTs can be used for a multi-parameter analysis of cells in different conditions. DHM can be applied only to cells laid on a surface while OOTs allow us to study the behaviour of the cells under forces comparable to those present in the blood stream. Both techniques provide useful information regarding the bending modulus and can be successfully used to characterize and compare different types of red blood cells.

4

MORPHOLOGICAL MARKERS FOR NEUTROPHIL DIFFERENTIATION

In this chapter, I will present the results of investigation on the DHM usefulness to characterize neutrophil precursors at distinct differentiation stages using label-free morphological markers. Moreover, an automatic segmentation method is proposed to estimate the nuclear region, which has the potential to be extended for nuclear and cell characterization in other contexts.

4.1 INTRODUCTION/ MOTIVATION

Nuclear morphology is closely related to cellular functioning, and during human neutrophil differentiation, the nucleus undergoes significant changes which are further correlated with its biophysical characteristics. Morphological abnormalities in human neutrophils have been reported in severe infections [131–134] and have recently being observed in patients with SARS-CoV-2 infection [135–138]. Since the use of ex-vivo primary mature blood neutrophils in large scale is very limited, mature neutrophil-like granulocytes are differentiated from human myeloid leukemia cell lines.

Human neutrophils are polymorphonuclear and phagocytic leukocytes that comprises our innate immune system. They are generated from granulocyte-monocyte progenitors (GMPs) in the bone marrow, where they undergo several stages of maturation [139]. Primary blood neutrophils have a short lifetime, and lack proliferation and transfection capacity, thus limiting their ex-vivo experimental use in the laboratory [140]. Therefore, protocols using human myeloid leukemia cell lines, such as HL-60 and PLB-985 (which provides higher differentiation efficiency), have been developed for neutrophil differentiation in-vitro [141, 142]. In the presence of appropriate inducing agents, these cell lines can undergo granulocyte differentiation into mature neutrophil-like granulocytes [139, 140, 143]. The assessment of the differentiation process is based on cellular morphological parameters, molecular and functional properties of differentiated cells, defining a neutrophil-like phenotype which resembles to the mature blood neutrophils mostly [143, 144].

Human promyelocytic leukemia cell lines, can be differentiated into granulocyte -like cells using a wide variety of agents, such as all-trans retinoic acid, butyrate, hypoxanthine, dimethyl sulfoxide (DMSO) or dimethylformamide (DMF). During differentiation process, which lasts about 4-6 days, they follow the subsequent stages: myeloblasts, promyelocytes, myelocytes, metamyelocytes, band neutrophils and finally polymorpho nuclear (segmented) neutrophils [139, 140, 145]. Monitoring the changes in nuclear morphology represents one of the

most reliable technique to assess different stages and the success of the differentiation process [144, 146, 147]. Thus, cells in segmented neutrophils stage, presenting polymorph nucleus formed usually by two to five nuclear segments, are considered as mature neutrophile-like. In the first stages (promyelocyte and myelocyte) cells have compact ellipsoidal nuclei occupying almost all the cell body. Nuclei of the metamyelocytes begin to be distorted and present indentations. Band neutrophils have more distorted nuclei often with a “horseshoe" shape, while in the final stage, segmented neutrophils present multi-lobed nuclei connected between them [144, 146, 147]. A schematic representation of each maturation stage beginning from a promyelocyte is shown in Figure 4.1.

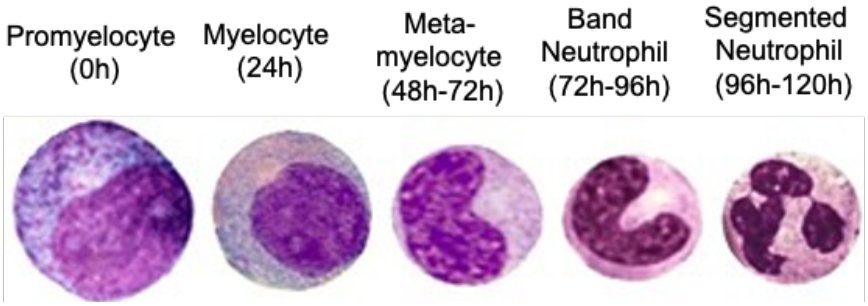

Figure 4.1: Neutrophil differentiation drawing scheme. From left to right: Promyelocytes have round nucleus, occupying more than 50% of the cell. Myelocytes are slightly smaller with smaller round nucleus if compared with Promyelocytes. Meta-myelocytes have ellipsoidal nuclear shape with indentation. Band neutrophils presents a nuclar shape similar to a “horseshoe". In the last differentiation stage, the nucleus develop lobes and the cell is classified as segmented or polymorphonuclear neutrophils.

The current practice to examine the nucleus morphology during neutrophil differentiation involves nuclear staining and epifluorescence microscopy [145, 148–150]. Since these techniques require sample preparation and provide relatively poor information, they are mostly used to evaluate the final stage of the differentiation process. Moreover, the labelling methods have a potential risk of altering cellular functions and phototoxicity from repeated excitation of the dye in the imaging process limits the duration of the time-lapse imaging [150].

Oppositely, label-free techniques, such as Quantitative Phase Imaging (QPI) are completely non-invasive because they do not require any sample preparation. Further, if applied in suitable conditions, with temperature and O_2 control, as in an incubation chamber, the technique itself do not have limitations regarding the experiment time. DHM, as a common implementation of QPI, has been recently implemented in different setups to study morphology, structure and dynamics of unstained living cells [46, 48, 67].

Morphological and biomechanical features such as cell and nuclear shape, and membrane fluctuations are promising label-free biomarkers candidates for both fast screening and detailed liquid biopsy. Many of them have been successfully

combined with machine learning algorithms in cytometric classification of cancer cells and blood cells [151], phenotyping of cell lines [152], classification of leukocytes flowing in microfluidics [153] or automatic detection of P. falciparum [154].

Using QPI with a common arrangement for DHM, this chapter reports the study (published in [21]) on the usefulness of a set of cell parameters extracted directly from OPD to supervise the neutrophil differentiation from PLB-985 cell line.

4.2 MATERIAL AND METHODS

This section corresponds to the section "Methods" in [21].

4.2.1 *Cell preparation*

Neutrophil differentiation from its promyelocytic progenitors was performed following the dimethyl sulfoxide (DMSO) protocol described in [142]. Briefly, PLB-985 cells (DSMZ, Braunschweig, Germany) were cultured in RPMI 1640 media supplemented with 10% fetal bovine serum (FBS), 1% L-Glutamin, as well as streptomycin (100 mg/mL) and penicillin (100 U/mL) (P/S)] at 37^oC in a humidified atmosphere with 5% CO_2. Cell cultures were passed three times per week, maintaining cell densities between 10^5 and 2×10^6 cells per mL. The cells were differentiated into a neutrophil-like state by culturing at an initial density of 2×10^5 using RPMI 1640 media supplemented with 10% FBS concentration and 1.3% DMSO for 6 days.

Cell differentiation was monitored each 24 hours beginning from day 0, for 6 days. For each measurement, $1\,mL$ of cell suspension was taken from the culture flask. The suspension was then centrifuged and the supernatant was removed to exclude debris and impurities. Then, the sample was resuspended and incubated for 5 minutes at 37^oC. To measure the cells, $50\,\mu L$ of cell suspension was placed in a $18\,mm$ diameter glass slide. About 2-3 minutes were required for cells to sediment before beginning to image it. For DHM imaging the sample was resuspended in RPMI 1640 media while for fluorescence imaging the sample was resuspended in a Hoechst 33342 solution of 1:1000 in RPMI 1640 media as in [149].

4.2.2 *Digital Holographic Microscopy Measurements*

We used a simplified version of a previously developed DHM off-axis configuration, based on a Mach-Zehnder interferometer [65, 68]. The laser beam ($\lambda = 520\,nm$, Thorlabs LP520-SF15) was split into object and reference beams by a fiber optic coupler (Thorlabs TW560R3F1) and recombined by a cube beam splitter (Thorlabs, BS079) to generate the hologram, recorded on a sCMOS camera (Thorlabs CS2100M-USB Quantalux). The power P of the laser

was set to $P < 1\,mW$, and the exposure time $1 < t < 5\,ms$. The magnification of the microscope was 33X, with a lateral spatial resolution $d \sim 600\,nm$. An aspheric lens (Thorlabs C230TMD-A) with the numerical aperture NA=0.55 was used as objective lens. The size of the sCMOS sensor was $4.8\,\mu m \times 4.8\,\mu m$. The inter-fringe i, of the interference pattern was adjusted to 5 pixels on the sensor, corresponding to $750\,nm$ at the sample plane.

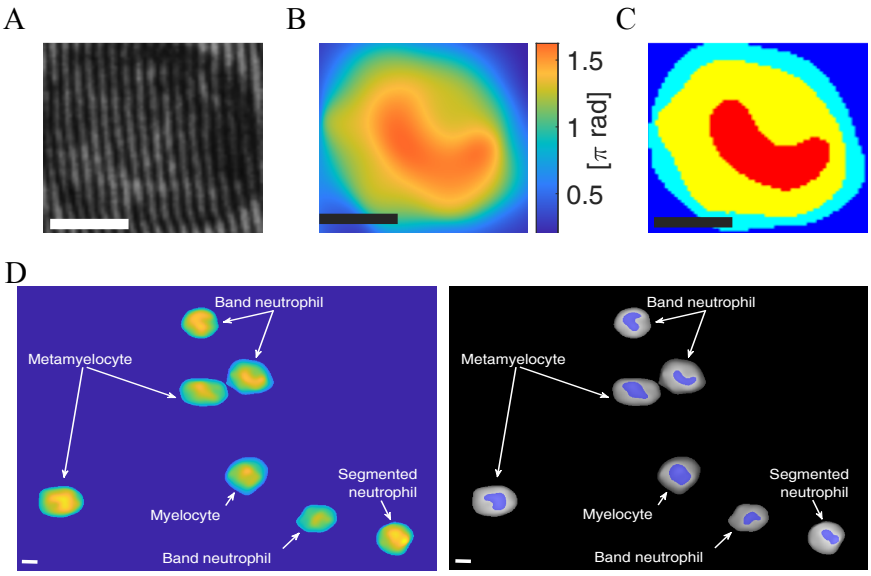

Figure 4.2: **(A)** recorded hologram, **(B)** reconstructed Optical Phase, **(C)** segmentation,**(D)** full field image taken at day 5 showing different types of cells; left: after cell selection, the colors indicate cell height; right: cell and nucleus regions are shown after cell and nucleus selection. Scale bars: $5\,\mu m$.

The numerical reconstruction of the optical phase was performed using a method based on the spatial filtering at the Fourier plane from the recorded hologram [66]. Thus, the complex amplitude distribution of the transmitted frequency band-pass was recovered by applying a Fourier transform over the recorded hologram and considering a circular spatial filtering mask, located at one of the diffraction orders. After the filtering and centering process at the Fourier domain, the complex amplitude was Fourier transformed again to propagate it to the sample plane and retrieve the wrapped optical phase. The final step is phase unwrapping to get the reconstructed optical phase function. Since these issues are of particular significance in the reconstruction process, we defined the parameters for spatial filtering, propagation and phase unwrapping by calibration with silica microbeads of different diameters $(3 - 30\mu m)$ [68]. Microbeads are the perfect sample for calibration purposes since they are microspheres of a single material (silica, polystyerene, etc.) with known value of the refractive index.

4.2.3 *Segmentation of the OPD function for cell and nuclear region designation*

To automatically identify the cells present in the full field of view, Otsu's global threshold [155] is applied to the Optical Phase Difference (OPD) images after normalization. The original OPD image is masked with the binary matrix generated after global threshold segmentation and all the background pixels are set to zero. To avoid that non desired objects present in the image, such as debris or dirties, to be processed as cells, the phase volume of each object is computed and those volumes below a predetermined threshold are discarded. Each cell is then cropped to its bounding box region and a four-level segmentation (L=4) is performed with MATLAB *multitresh* function followed by *imquantize* from the Image Processing Toolbox. The number of levels ($L = 4$) is justified by the Histogram-based Valley Estimation Method for determining the number of clusters for an image to be properly segmented as described in [156]. Within the cell region, three clusters are presented (as shown in figure 4.3) while the fourth one refers to the background pixels (not shown in the histograms). Furthermore, the search-based algorithm from *multitresh* function does not converge for $L > 4$ and has lower values of the metrics coefficient for $L < 4$, indicating that the different classes are not optimally separated.

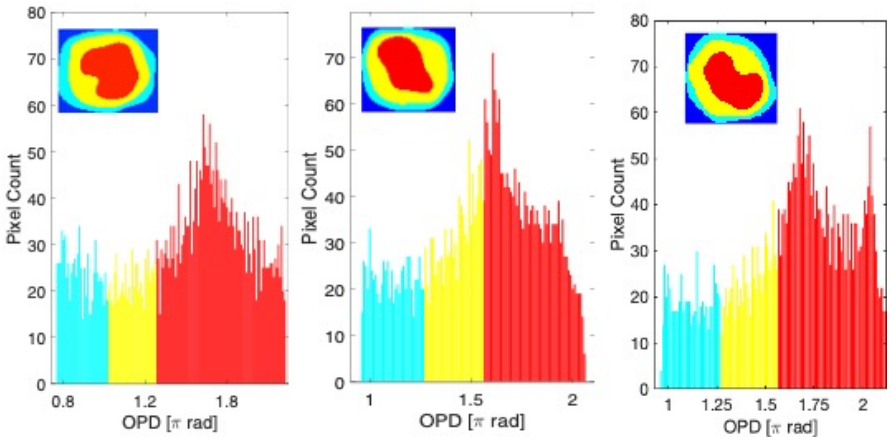

Figure 4.3: Histograms presenting the pixels count within the cell region. Each colour represents a class corresponding to a cell region (shown on the top). The nucleus is designated to the last segmentation class coloured in red, the cyan and yellow regions are assigned to the cytoplasm.

In both single and multiple threshold segmentation, the thresholds are estimated based on Otsu's global segmentation [155]. Briefly, it works by searching the thresholds that minimizes the weighted within-class variance (called intra-class variance), while maximizes the between-class variance (called inter-class variance). For an image represented in G gray levels $(0, 1, ..., G-1)$, the number of pixels at level i is denoted by f_i; then the total number of pixels

equals $N = f_0 + f_1 + ... + f_{G-1}$. For a given gray level image, the occurrence probability of gray level i is given by:

$$p_i = \frac{f_i}{N}, \quad p_i \geq 0, \quad \sum_{i=0}^{G-1} p_i = 1 \tag{4.1}$$

If the image is segmented into L levels (classes) $(C_0, C_1, ..., C_{L-1})$, $L-1$ thresholds $(t_0, t_1, ..., t_{L-2})$ must be selected. The cumulative probability w_l and mean gray level μ_l for each class C_l are respectively given by:

$$w_l = \sum_{i \in C_l} p_i \quad and \quad \mu_l = \sum_{i \in C_l} i \cdot p_i / w_l, \; l \in 0, 1, ..., L-1 \tag{4.2}$$

Therefore, the mean intensity of the whole image μ_T, the between-class variance σ_B^2 and within-class variance σ_W^2 are respectively determined by:

$$\mu_T = \sum_{i=0}^{G-1} i \cdot p_i = \sum_{l=0}^{L-1} \mu_l w_l \tag{4.3}$$

$$\sigma_B^2 = \sum_{l=0}^{L-1} w_l (\mu_l - \mu_T)^2 = \sum_{l=0}^{L-1} w_l \mu_l^2 - \mu_T^2 \tag{4.4}$$

and

$$\sigma_W^2 = \sum_{i=0}^{G-1} w_i (\mu_i \mu_T)^2 - \sigma_B^2 \tag{4.5}$$

The optimal thresholds are determined by minimizing the within-class variance(σ_W^2), while maximizing the between-class variance (σ_B^2).

The nuclear region is defined as the pixels from the last segmentation level (coloured in red in Figure 4.3), because they are in agreement with the expected morphology for the nucleus corresponding to each cell maturation stage.

4.3 RESULTS AND DISCUSSION

To understand if the morphological characteristics extract by DHM could be used as label free-markers to classify cells during its maturation stage, PLB-985 cell line was monitored during differentiation from promyelocytes to segmented neutrophils. The cells were imaged at intervals of 24h for 6 days during its differentiation cycle. The prominent morphological changes undergone by the cell nucleus during neutrophil differentiation is already well stablished and (together with other biochemical analysis) used to categorize the differentiation stage. We aimed to perform the same classification without the need of nuclear staining, by estimating the nuclear region based on OPD measurements.

In Figure 4.2, an example of image taken at day 5 of treatment (Section 4.2.1) shows the presence of multiple types of cells as indicated by the morphology of the cell and the designated nuclear regions, characterized by high values of the OPD function. At a first qualitative inspection, using the morphological phenotypes reported in literature [144, 146, 147] it is possible to identify one segmented neutrophil (SN), three band neutrophils (BN), two metamyelocytes (MM), one myelocyte (M). BN are the most frequent, as expected for day 5. The presence of other types of cells is justified by the various biological times employed by different cells to transform [139]. This observation indicates that OPD and the segmented OPD could be used to extract morphological markers to characterize different stages during neutrophil differentiation.

4.3.1 *Cell Differentiation*

To compare the results reported in literature based on nuclear staining and fluorescence imaging, we performed image analysis of the nucleus morphological changes using Hoechst staining and live cell fluorescence imaging (Nikon TE2003-E inverted microscope, 60X, DAPI fluorescence cube). In Figure 4.4 an example of nuclear architecture changes is given for each differentiation stage. In the first three rows: bright field, DIC and fluorescence microscopy images were taken for the same cell with the same field of view (in each column). The last two rows illustrate the DHM phase reconstruction images (on the top) and the image segmentation with the suggested segmented nuclear region (in red). Despite both bright field and DIC imaging allows only the entire cell to be identified without no indication of the nuclear region, the last one offers better contrast. In fluorescence images only the DNA was stained, thus the highlighted regions corresponds to the nucleus.

At the beginning of the differentiation, corresponding to promyelocytes (PM) and M cells, the cell nucleus is round to oval, occupying more than 50% of the cell projected surface area (shown in columns 1 and 2 in Figure 4.4). The oval shape begins to be preponderant to round shape for M, and the ratio between nucleus and cell area is also slightly smaller than for PM. As the cell matures, the nucleus begins to be indented and becomes asymmetric with respect to the cell center (MM). A more mature cell presents highly indented nucleus and often a “horseshoes” shape (BN), arriving to the segmentation of the nucleus at the end (SN).

Neutrophil differentiation was monitored recording five DHM image fields / day at intervals of 24h starting from DMSO treatment day 0 (Section 4.2.1). Two different differentiation cycles were completed. The OPD was calculated for each field and a qualitative inspection performed as discussed above and showed in Figure 4.2, discarding the cells which did not correspond to the differentiation stage of the respective day. Five groups of $N > 20$ cells were

created, corresponding to the 5 stages: PM, M, MM, BN and SN, and calculated the parameters defined above for each cell.

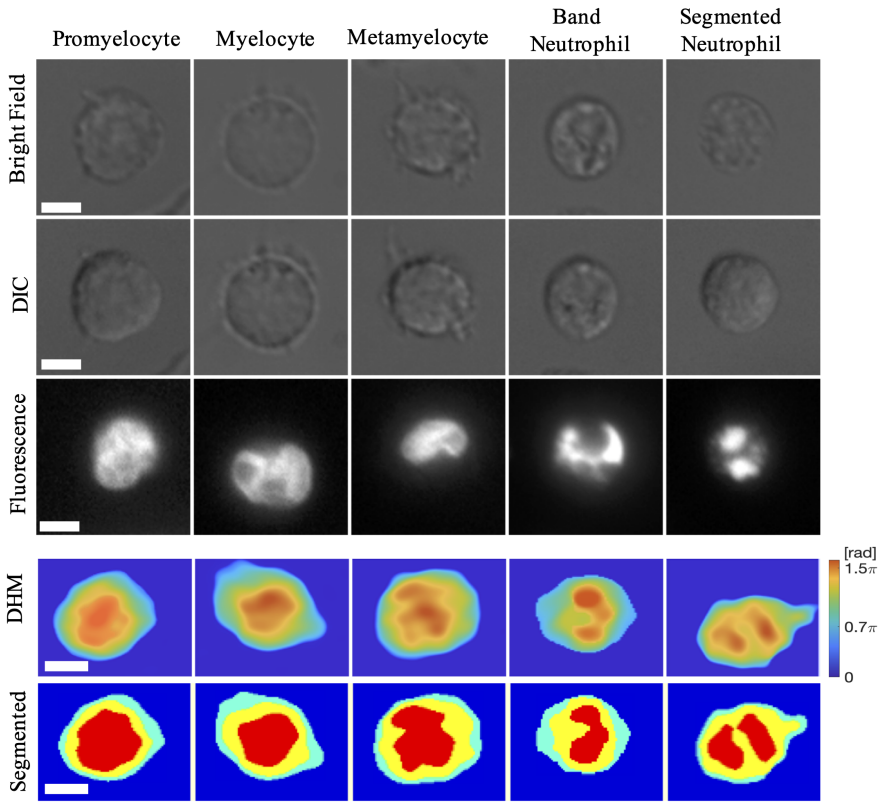

Figure 4.4: The first three rows show Bright field, DIC and Fluorescence images, where each column represents the same cell. The last two rows shows the reconstructed Optical Phase Difference (OPD) and cell segmentation.Scale bar: $5\mu m$

4.3.2 *Label-free Morphological Parameters from Optical Phase Difference*

Cellular morphologic parameters as projected surface area, optical volume and circularity have been effectively used for the characterization of red blood cells [127], [65], [157] in QPI and DHM. Similar parameters have also been used to screen and classify mouse lymphocytes and macrophages [64] and recently to classify white blood cells from bone marrow using RI tomograms [158]. Here we propose similar parameters also for the nucleus, including the ratios between the values for nucleus and cell as parameters. We define the following morphological parameters:

1. Projected surface area (PSA), of the cell and nuclear regions:

$$PSA = N \cdot (ps/M)^2 \tag{4.6}$$

where N is the number of pixels within the cell, respectively nucleus region, $ps = 4.8 * 4.8 = 23.04\mu m^2$ is the area of a single pixel of the CMOS sensor and M= 33X is the microscope magnification.

2. Optical Phase Volume (OV), of the cell and nuclear regions:

$$OV = PSA \cdot \sum_{i=1}^{N} OPD_i \tag{4.7}$$

where $OPDi$ is the optical phase difference of cell / nucleus corresponding to pixel.

3. Circularity (C), of the cell and nuclear regions:

$$C = 4\pi \cdot PSA/Pm \tag{4.8}$$

where Pm is the perimeter of the cell / nucleus. Circularity expresses the roundness of an object, e.g. $C = 1$ means a perfectly round cell, as a circular disk.

4. PSA and OV nucleus to cell N/C aspect ratio:

$$\begin{aligned} PSA_{N/C} &= PSA_N/PSA_C \\ OV_{N/C} &= OV_N/OV_C \end{aligned} \tag{4.9}$$

where N stays for nucleus, C for cell, PSA for projected surface area and OV for optical volume.

The mean and standard deviation values for each parameter are presented in Figure 4.5A. for each group of cells. As one can note, PSA and OV monotonously decrease as the cells maturate, both for cell and nucleus region. The cell circularity, C_C is preserved close to $C_C = 1$ for PM, N and MM, decreasing slightly for the last two stages, BN and SN ($C_C > 0.9$). As the cells present more protrusions in these two stages, the values for circularity are also more dispersed. The circularity values for nucleus, C_N decrease more than for cell: $C_N > 0.8$ for PM and M, $C_N = 0.8 \pm 0.08$ for MM, $C_N = 0.69 \pm 0.13$ for BN and $C_N = 0.63 \pm 0.15$ for SN, indicating that the nucleus undergoes substantial morphological changes during the differentiation process. The relative morphological changes of the nucleus vs cell are outlined by the N/C ratio for area and volume respectively, $PSA_{N/C}$ and $OV_{N/C}$ in the last row of Figure 4.5, where both ratios decrease monotonically during cell maturation, with a more pronounced change in $OV_{N/C}$.

The values between neighboring stages overlap for some parameters, indicating that a set of parameters should be considered rather than a single parameter, to characterize the differentiation stages. In order to test the weight of each parameter we used the Mann-Whitney U test (or two-sided Wilcoxon rank sum) test for each pair of classes. The results are schematically illustrated in Figure 4.5: $p < 0.05$ (blue box) is considered as a threshold for good distinction between stages, $0.05 < p < 0.1$ (gray) as acceptable and $p > 0.1$(white) as non-confident.

4.3.3 *Morphological parameters as markers to asses PLB-985 differentiation*

All the eight parameters showed to be individually suitable to distinguish SN from PM. All parameters but cell PSA_C and cell OV_C were useful to discriminate SN from M and MM. Only three parameters ($OV_{N/C}$, $PSA_{N/C}$, $OV_{N/C}$) are available to distinguish between SN and BN. All the used parameters were extracted from the OPD, which is provided by DHM only. Additionally, the presence of a segmented nucleus (SN), represents another useful parameter which distinguishes SN from all the other stages (crossed box in Figure 4.5).

All the eight parameters are suitable to distinguish BN from PM cells, four of eight parameters to separate BN from M cells, and only two to discriminate BN from neighbouring stage, MM: the nucleus and cell circularity, C_N and C_C. These two parameters are complementary to the parameters which distinguish BN from the other neighbouring stage, SN. Moreover, considering $0.05 < p < 0.1$ for an acceptable discrimination, the nucleus area PSA_N becomes also and eligible parameter to distinguish between BN and MM or M.

As regards the MM cells, seven of eight parameters are useful to distinguish MM from PM cells, but none is adequate using the criterium $p < 0.05$ to separate MM from M. However, considering $p < 0.1$, both NA and NC can be used to separate M from MM. Finally, five of eight parameters can be used to separate M from PM cells. These parameters are complementary to the parameters used to distinguish between BN and MM, and only two are in common with the discrimination between BN and SN. Five parameters can be used to separate M from PM cells. These parameters are complementary to the parameters used to distinguish between BN and MM, and only two are in common with the discrimination between BN and SN. According to the imposed criterium, p-value $p < 0.05$, the nearest two classes seem to be MM and M cells. However, relaxing the criterium to $p < 0.1$ two more parameters are indicated as suitable also for MM and M cells discrimination.

The analysis of the results show that all the morphological parameters are useful to discriminate between cells in different differentiation stages. Three of these parameters: OV_N, OV_C, $OV_{N/C}$, which have a central role for cell characterization and discrimination between differentiation stages, are extracted from the OPD, being completely label-free. These preliminary results suggest that a combination of the parameters derived by means of DHM in a multiparameter testing scheme would allow to characterize and monitor the stages of the cell differentiation.

Cell morphological analysis was performed during promyelocytic differentiation into segmented neutrophil for both cell and nuclear regions using DHM as free label optical imaging technique. DHM provides additional information with respect to the standard fluorescence imaging of stained nucleus. This information is related to the cell and nucleus volumes and allows a better

discrimination between different stages of neutrophil differentiation. Being automatized this analysis can be extended for higher throughput configuration and is a good candidate to used for liquid biopsy analysis.

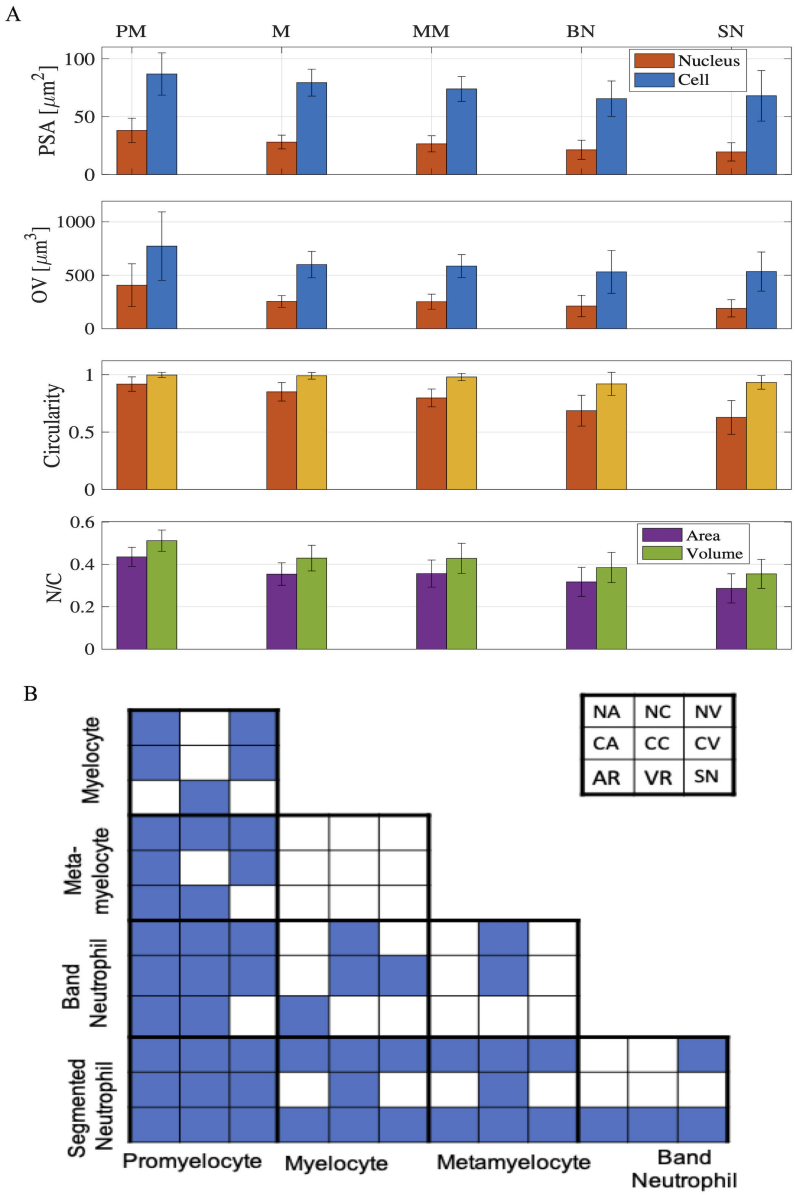

Figure 4.5: (a) Projected Surface Area (PSA), Optical Volume (OV), Circularity, and ratios nucleus to cell NC of PSA and OV. Mean and standard deviation values for: promyelocytes (PM, $N = 22$), myelocytes (M,$N = 21$), metamyelocytes (MM, $N = 24$), band neutrophils (BN, $N = 21$), segmented neutrophils (SN, $N = 25$). (b) Diagram showing the results of the Mann-Whitney U test calculated for nine parameters, for each class pair. A p-value $p < 0.05$ is indicated by blue color. The legend of the parameters is shown top right: PSA_N, PSA_C - nucleus respectively cell PSA; C_N, C_C - nucleus, cell circularity; OV_N, OV_C - nucleus, cell OV; $PSA_{N/C}$, $OV_{N/C}$ ratio for PSA and OV; SNG - segmented nucleus.

5

NUCLEAR SHAPE AS A MORPHOLOGICAL MARKER FOR NEUTROPHIL DIFFERENTIATION: LAMIN A/C BEHIND THE SCENES

Although this Thesis is mainly focused on label-free techniques, the use of labels is important because it allows the imaging of native supramolecular structures in the Lamina in intact cells. Thus, this advantage will be used to bring insights into why nuclear morphology can be used as a trustful label-free marker. In this chapter, I will present preliminary results of a quantitative analysis of the supramolecular distribution of Lamin A/C in the nucleus of neutrophil precursors (promyelocytes from PLB985 cell line) imaged by Stimulated Emission Depletion (STED) Microscopy. An algorithm for automatic Lamin meshwork extraction will be presented in detail. Further, we will see that nuclear morphological changes during neutrophil differentiation are associated with structural changes in the Lamin A/C meshwork.

5.1 INTRODUCTION

The nucleus has long been considered the cell's command unit, housing genetic material and providing a biochemical factory for DNA replication and RNA synthesis [20]. It is the largest organelle and up to ten times more rigid than the cytoplasm. The nucleus exerts significant influence on cellular biomechanical functioning [159]. Although it is known that the nuclear morphology has a straight relation with cell functioning, the exact mechanisms governing it are still not clear [160, 161].

For more than a century, diagnostic pathologists have used morphologic abnormalities of the nucleus as essential diagnostic features to perform biopsy. These features include nuclear enlargement and increased nuclear-to-cytoplasmic ratio and nuclear membrane irregularities [161]. Nevertheless, nuclear morphological changes are not always associated to mutations or pathologies. For some type of cells, nuclear morphological changes are required for its regular functioning [20, 160]. This is also the case of neutrophil cells and its precursors [20].

5.1.1 *Lamin A/C and the Nucleus shape*

Most eukaryotic cells have a single nucleus in which a nuclear envelope (NE) separates the chromosomes from the cytoplasm. The NE is composed of two lipid bilayers: the outer and inner nuclear membranes, nuclear pore complexes (NPC), and the nuclear Lamina. The outer nuclear membrane (ONM) is continuous with the endoplasmic reticulum, whereas the inner nuclear membrane

(INM) surrounds the nuclear Lamina [162].

The nuclear Lamina is made predominantly of intermediate filaments called Lamins, of which there are two main types: type A and type B, based on their primary sequence and biological properties [163, 164]. In mammals, Lamins are encoded by three genes: *LMNB1* encodes Lamin B1, *LMNB2* encodes Lamin B2 and Lamin B3, and *LMNA* encodes the major forms Lamin A and C (referred to as Lamin A/C in this Thesis), as well as Lamins AΔ10 and C2 [163, 164].

The structural roles of Lamin A/C include maintenance of nuclear shape, nuclear positioning and genome organization [163–166]. It has long been known that changing in the levels of Lamin A/C leads to alteration in nuclear shape [160]. Indeed, cells with abnormally shaped nuclei are often seen in diseases in which Lamina proteins are mutated (collectively called Laminopathies) [167]. Changes of Lamina proteins expression can also occurs in healthy cells. In neutrophils, for instance, the lobed nuclear shape is linked to a considerable decrease of Lamin A/C expression with respect to its precursors (promyelocytes) [168].

In spite of the important role Lamin A/C plays in neutrophils nuclear structure and function, their spatial organization in nuclei have remained elusive. In this chapter, I will present a quantitative analysis of the supramolecular distribution of Lamin A/C in the nucleus of neutrophil precursors (promyelocytes from PLB985 cell line) imaged by Stimulated Emission Depletion (STED) Microscopy. This work has been done during a three months internship in the Max-Planck-Institut für medizinische Forschung, (Heidelberg, Germany), of which purpose was mainly training for a new technique.

The use of labels allows the imaging of native supramolecular structures in the Lamina of intact cells. Thus, this advantage will be used to bring insights into why nuclear morphology can be used as a trustful label-free marker.

5.2 MATERIALS AND METHODS

5.2.1 *Sample Preparation*

PLB-985 cells (DSMZ, Braunschweig, Germany) were cultured in RPMI 1640 media supplemented with 10% fetal bovine serum (FBS), 1% L- Glutamin, as well as streptomycin ($100\,mg/mL$) and penicillin ($100\,U/mL$) (P/S) at 37^oC in a humidified atmosphere with 5% CO_2. Cell cultures were passed three times per week, maintaining cell densities between 10^5 and2×10^6 cells per mL. The cells were differentiated into a neutrophil-like state by culturing at an initial density of 2×10^5 using RPMI 1640 media supplemented with 10% FBS concentration and 1.3% DMSO for 6 days without changing the medium.

Neutrophil differentiation from its promyelocytic progenitors was performed following the dimethyl sulfoxide (DMSO) protocol described in [142]. Briefly, PLB-985 cells (DSMZ, Braunschweig, Germany) were cultured in RPMI 1640 media supplemented with 10% fetal bovine serum (FBS), 1% L-Glutamin, as well as streptomycin (100 mg/mL) and penicillin (100 U/mL) (P/S)] at 37^oC in a humidified atmosphere with $5\% CO_2$. Cell cultures were passed three times per week, maintaining cell densities between 10^5 and 2×10^6 cells per mL. The cells were differentiated into a neutrophil-like state by culturing at an initial density of 2×10^5 using RPMI 1640 media supplemented with 10% FBS concentraion and 1.3% DMSO for 6 days.

Before fixation, PLB985 cells were washed two times in phosphate-buffered saline (PBS) solution and resuspended in PBS with a final concentration of 10×10^7 cells per mL. $500\,mL$ of cell suspension was placed on the top of a $15\,mm$ diameter cover slip. The cells were then taken to a humidified atmosphere with 5% CO_2 at 37^oC for 20 minutes. After that, the cover slip was carefully washed with PBS. Both PLB985 and U2OS cells were fixed methanol at -20^oC for 10 minutes. Cells were permeabilised for 5 min in 0.1% Triton X-100 and blocked with 1% BSA for 1 h. Samples were incubated with primary antibody dilutions in PBS for 1 h at room temperature. Primary antibodies used were: mouse monoclonal Anti-Lamin A + Lamin C antibody cat. [ab8984] (1:50 dilution for PLB985 cells and 1:200 for U2OS cells; 131C3; Abcam, Cambridge, UK). Samples were washed and incubated with secondary antibody: goat anti-mouse immunoglobulin G (IgG) – STAR580 cat.[ST580-1001] (1:200 dilution, Aberrior Labels GmbH, Germany).

5.2.2 *Imaging*

The images were acquired using the microscopy facilities from the Max-Planck-Institut für medizinische Forschung, Department of Nanoscopy at Heidelberg (Germany), after a training kindly held by Dr. Elisa D'Este.

Samples were imaged on an Abberior expert line (Abberior Instruments GmbH, Germany) with pulsed STED line at $775\,nm$, excitation laser at $580\,nm$. Detection window was set to $600-630\,nm$. Images were acquired with a 100x/1.4 NA magnification oil immersion lens. Pixel sizewas set to $20\,nm$[1] , pinhole to $100\,\mu m$ (0.85 AU). Laser powers, line accumulations and dwell times were kept consistent throughout the entire study. Confocal acquisition of the STAR580 channel was performed in all the image sequences to monitor lateral drift. Axial drift was minimised by the Z-focus drift compensation unit.

1 As in confocal microscopy, in STED the pixel size is given by the size of the scanned area divided by the number of pixels used to sample the area in each X and Y direction. For a $20\,\mu m \times 20\,\mu m$ scanned area, if there are 1024 pixels per scanned line, the final pixel size will be $\approx 20\,nm$.

Computing environment

Images were captured and visualised with Imspector (Abberior Instruments GmbH, Göttingen Germany). MATLAB (MathWorks, Natick, MA) was used as the base numerical computing package to analyze images and data. The Java library Bioformats was used to load images and metadata from the microscope files into MATLAB [169].

5.2.3 *Automatic Lamin Meshwork Segmentation and Characterization*

The contrast of the image was adjusted by saturating the bottom 1% and the top 1% of all pixel values. Then, a mask for the cell nucleus was created by using global Otsu's threshold [155]. Morphological closing by a disk with a radius of 3 pixels, filling, and opening with a disk with a radius of 100 pixels were used to create a binary image without holes. The largest connected component of the image covering $< 80\%$ of the image was selected as the mask for the nucleus. Nuclei consuming $> 80\%$ of the image were excluded from meshwork segmentation and analysis since there would be insufficient background pixels to determine thresholds for auditing.

On the masked image, the meshwork segmentation was performed using an optimized steerable line filter based on linear combinations of Gaussian derivatives up to the fifth order [170] (Gaussian SD = 4 pixels = 120 nm to obtain a ridge detection). The filters were implemented by F. Aguet in C++ with wrappers for Matlab [171]. Nonmaximal suppression (NMS) [172] was applied to identify the center of each filtered curvilinear structure, representing a meshwork edge. The resulting from NMS was then binarized (Figure 5.1 bottom row). Only edges made of at least ten pixels and within the nucleus mask were retained. Then, unconnected pixels were bridged, that is, 0-valued pixels were set to 1 if they had two nonzero neighbors that were not connected. The result was skeletonized. Gaps of 5 pixels between two ending edges were filled using the function *filledgegaps* [173]. The boundaries of the cell mask was computed and applied to the image. After this, the function *find junctions* [173] was used to classify the remaining edges according to the number of other pixels in its eight-connected neighbourhood. Pixels with more than two connected neighbours were junctions (i. e., intersections of two or more edges), and pixels with only one connected neighbour were endpoints. In addition, all the boundary pixels were set as junctions. To close gaps in the edges at junctions, manifesting themselves as premature endpoints, the distance between each endpoint and all the junctions was computed. Edges were extended from their original endpoint in that direction of the closest junction until a new junction was created with other edges. The extensions were done by using the Bresenham line extension algorithm [174]. The resulting connected meshwork was then skeletonized. The complementaty of the resulting meshwork image was calculated and each connected region was labeled (shown in last image

from Figure 5.1).

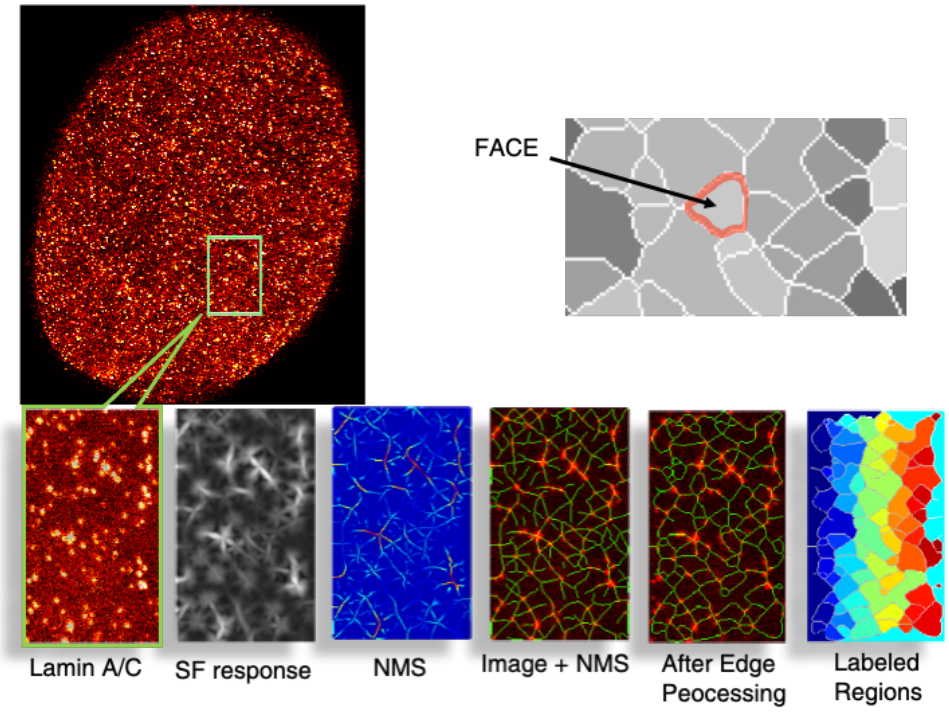

Figure 5.1: Schematic of meshwork segmentation. Image of U2OS cell labeled against Lamin A/C after cell nucleus mask and intensity adjustment was applied. Image size: $15 \times 18\,\mu m^2$. On bottom inset: cropped rectangular region, size: $2.8 \times 4.4\,\mu m^2$. The consecutive frames are: the steerable filter (SF) response; the nonmaximum supression (NMS) response, a montage of the original image superposed with the skeleton of the NMS, the resulting meshwork after edge processing and the labeled regions.

Meshwork properties were then, calculated by evaluating the properties of the labeled regions, denominated as *face* (shown in Figure 5.1). The properties: face perimeter, face area, and face eccentricity, were available by encoding these structures as connected components and using the built-in MATLAB command *regionprops*. For example, eccentricity is a measure of shape that is 0 for a circle or 1 for a line segment.

Properties were aggregated for multiple labeled regions in the same cells to create sample distributions, which were then compared. When comparing distributions of properties of Lamin A/C meshwork in wild-type cells (i. e.U2OS vs PLB985), the compared distributions originated from the same set of cells.

All the code was written by me using Matlab, unless otherwise explicitly stated. Built-in Matlab functions were used whenever available. The algorithm was optimised from [175].

5.3 RESULTS AND DISCUSSION

5.3.1 *Lamin A/C Automatic Meshwork Characterization*

Recent cryo-electron tomography revealed that the nuclear Lamina is composed of $54\,nm$ lenght Lamin filaments, approximately $3.5\,nm$ thick, binding to each other forming a micrometer scale meshwork structure with averaged connected filament's lenght of $380\,nm \pm 122\,nm$ for mouse embryonic fibroblast nucleus [176, 177]. While these structures are not directly resolvable by light microscopy, larger similarly oriented arrays of these filaments appear as fibers and have been detected by immunofluorescence with the super-resolution light microscopy techniques: including structured illumination microscopy (SIM) and stochastic optical reconstruction microscopy (STORM) [175, 178]. Using STED microscopy we obtained similar, but better resolved images with respect to previous SIM and STORM, which the reported resolution was $\approx 110 - 130\,nm$ [175, 178] against $70\,nm$ of our images with STED. Figure 5.2 shows a representative STED image from immortalized human bone osteosarcoma epithelial cell's nucleus (U2OS cell line) stained for Lamin A/C.

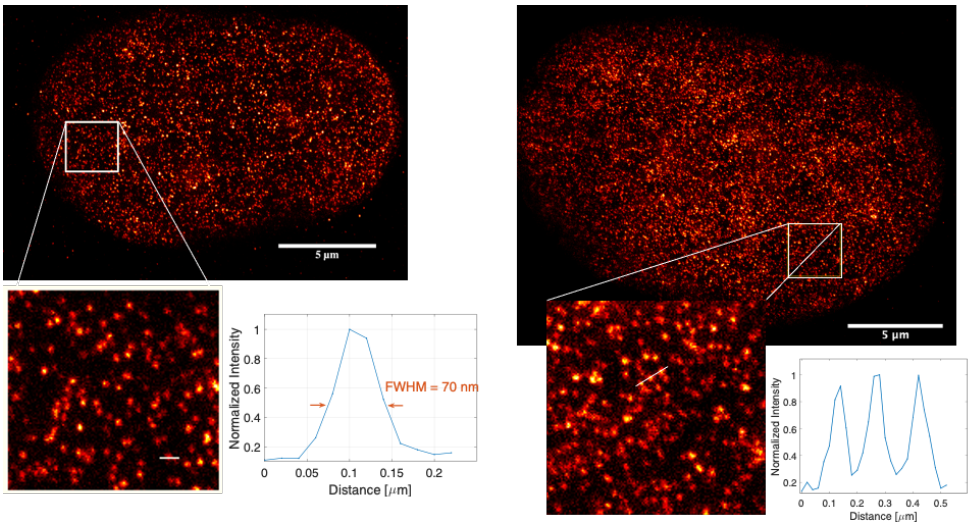

Figure 5.2: Representative STED images of Human Bone Osteosarcoma Epithelial Cells' nucleus. Samples were stained for Lamin A/C. The insets corresponds to the rectangular selection on the images, magnified approximately fivefold along each edge. Line profiles are marked on the insets. Scale bar is $5\,\mu m$.

Altough in Figure 5.2 we see dotted structures instead of filaments, this happens because the antibody binds only to the immunoglobulin (Ig) domain. A recent study on the structural basis for Lamin assembly at molecular level, described the crystal structure of a human Lamin A/C fragment at 3.2Å [179]. The proposed model for the assemble mechanism of mature human Lamin A/C reveled that Lamins filaments binds together in tetrametric assemblies (schematically shown in Figure 5.3). When a pair of Ig-like domains (shown as violet squared in Figure 5.3) are place on both sides of the tetramers, the

average distance between the neighbouring Ig-like domains is $\approx 20\,nm$. The $\approx 40\,nm$ long intervals is the distance between the C-terminal ends of two coiled-coil dimers in the same direction. Although a $70\,nm$ resolution is not enough to guarantee the localization of each single protein filament, it is good enough to detect a triplet of connected proteins.

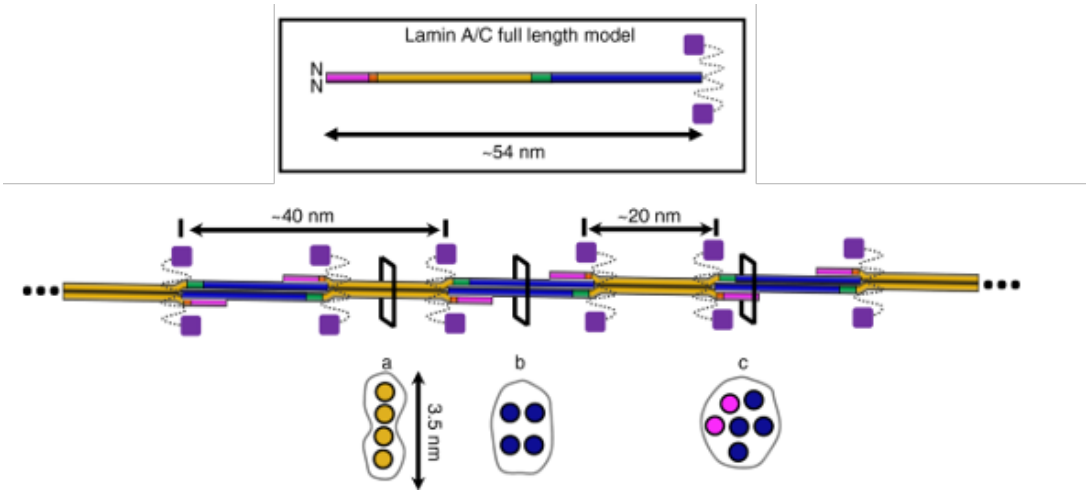

Figure 5.3: Proposed assembly mechanism of Lamin A/C. Schematic drawings of the dimer model of the 54-nm-long full-length Lamin A/C is in the box. The model of the mature Lamin filament, formed by the successive and alternative interactions between the dimers. When a pair of Ig-like domains (violet square) are placed on the both sides of the tetramers, the distance between the neighbouring Ig-like domains is $\approx 20\,nm$. Schematic cross-sections (a–c) of the Lamin filament model are shown in the bottom (circles represent intersection of an α-helix). Adapted from [179]

In Figure 5.2 we can see some brighter and bigger spots with respect to the the average pixels intensity and size. This might indicate the presence of a junction (i. e., more than two filaments connected together) or might be that more than one secondary antibody has binned to the same primary antibody [180]. The two hypothesis are not mutually exclusive.

The use of steerable filters (SF) to detect Lamin filaments meshwork from immunofluorescence super-resolution microscopy has been already validated in [175] and detailed explained in [178]. To test our implemented version of the algorithm, we applied SF to laimin A/C meshwork segmentation to the nucleus of 14 human bone osteosarcoma epithelial cells. These cells are adherent and present a flat and spread-out nuclear morphology, which makes them ideal for superresolution imaging [181].

Figure 5.4 shows the boxplot of resulting measurements from face area, eccentricity and perimeter for 14 cells. Each box corresponds to the meshwork of a single cell. From the graphs it is possible to see that the meshwork of the cells have a similar distribution for all the three parameters, however applying a Kruskal-Wallis test, the null hypothesis that all the 14 samples comes from the

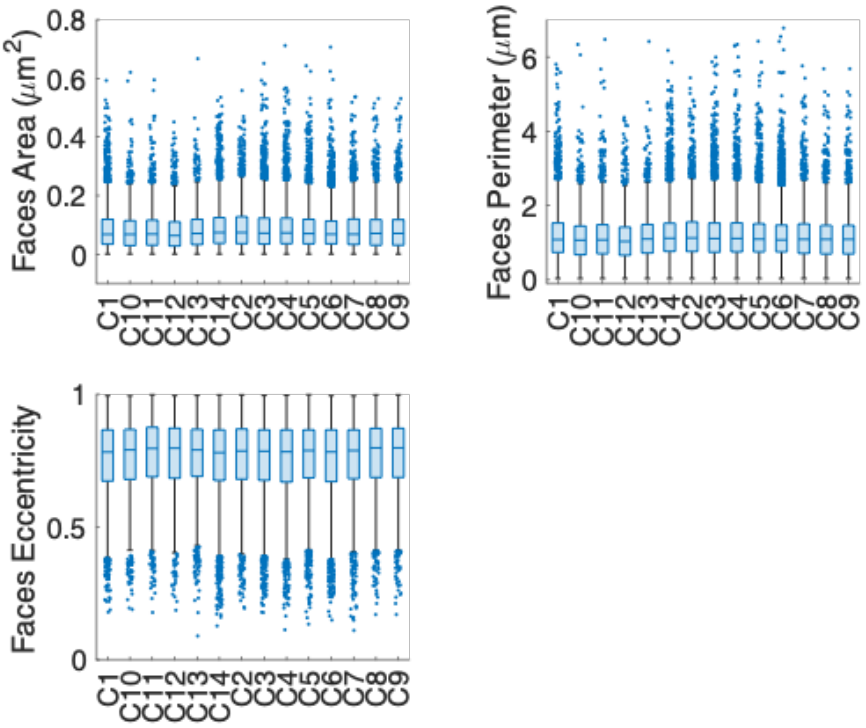

Figure 5.4: Box plot from the distributions of face area, perimeter and eccentricity from Lamin A/C meshworks of U2OS cells. 14 cells are presented in each graph.

same distribution is rejected with a significance interval $< 1\%$. This indicates that the algorithm to extract the meshwork is not influencing on the results, otherwise, all the cells would have the same distributions.

The median value for face area values considering all the cells was $0.07\,\mu m^2$. Since in literature there is no reported characterization of Lamin meshwork for U2OS cells, we do not have a direct reference to compare this value. However, the face meshwork size of HeLa cells nucleus (which have a similar nuclear morphology to U2OS) has been reported to have a median value of $0.13\,\mu m^2$ [182], which has the same order of magnitude as our results. On the other hand, the resolution limit from the microscopic technique used in the mentioned study was $200\,nm$, which is ten times higher than the distance between the neighbouring Ig-like domains [179]. Additionally, in their investigation the meshwork characterization was not done using SF.

Regarding face perimeter, the median value was $1.1\,\mu m$ and for eccentricity 0.79. In a recent study SF approach to derive Lamin A/C meshwork from immortalized mouse embryo fibroblasts (MEFs) have been used [175], however, the values for face area and and eccentricity have not been reported, since the purpose of the study was to compare different Lamins isotypes. Nonetheless, they reported the mean edge length per face of approximately $0.45\,\mu$ and an

average of 4.4 edges per face. Estimating the perimeter as ≈ (mean edge length per face × edges per face), we have 1.98 μm as estimated face perimeter. This value is almost two times the measured median face perimeter for U2OS cells, but still within the same order of magnitude.

5.3.2 *Lamin A/C is organized into distinct supramolecular structures in the nuclear Lamina during Neutrophil Differentiation*

We characterized the Lamin A/C meshwork of PLB985 cells during differentiation from promyelocytes to segmented neutrophils. Three time intervals after differentiation inducing treatment with DMSO were considered: after 48 h, 72 h and 120 h. To guarantee that chosen cells were from different maturation stages, besides differentiation time, the nuclear morphology was also taken in account by visual inspection as described in Section 4.3.1. The cells were then classified as non treated promyelocytes (NT), myelocytes (48 h), metamyelocytes (72 h) and segmented neutrophils (120 h). Figure 5.5 bottom right inset shows a representative for each type of cell, where it is possible to notice the morphological changes undergone by the nucleus.

Box plots with the resulting meshwork distribution for each type of cell is shown in Figure 5.5. Kruskal-Wallis test rejects the null hypothesis that the data from each population comes from the same distribution with a significance interval $< 1\%$. Non treated promyelocyte had smaller face area and perimeter (0.08 μm^2 and 1.07 μm respectevely) compared to treated cells, indicating that promyelocytes have denser Lamin A/C meshwork. Myelocytes had the second smaller face area 0.10 μm^2 and perimeter 1.25 μm followed by segmented neutrophils (0.12 μm^2 and 1.33 μm) and metamyelocytes (0.13 μm^2 and 1.37 μm). Myelocytes, which nucleus are characterized by an ovoidal shape had the most elongated faces with higher median face eccentricity value (0.76), while promyelocytes had the smaller face eccentricity value (0.71). Neutrophils and metamyelocytes had both median eccentricity values equal to (0.74).

The differentiation of promyelocytes into mature neutrophils is associated with Lamin A/C downregulation [20]; primary human neutrophils, differently from other cells from human immune system, express very low levels of Lamin A/C [165, 183]. Given that Lamin A/C expression changes are associated with granulopoiesis, we can expect an arrangement of Lamin A/C over the nuclear membrane. Despite the small number of investigated samples, our results confirms an architectural change of Lamin A/C over the nuclear membrane during differentiation based on the increase of meshwork face area, perimeter and eccentricity. Further experiments with a greater number of cells needed to be performed in order to provide a statically relevant number of samples.

Few differentiated cells have been used in this study because after 96 h of DMSO exposure, the great majority of the cells exhibit polarised lamellipodia formation as shown in Figure 5.6. These cells presented nucleus with elongated

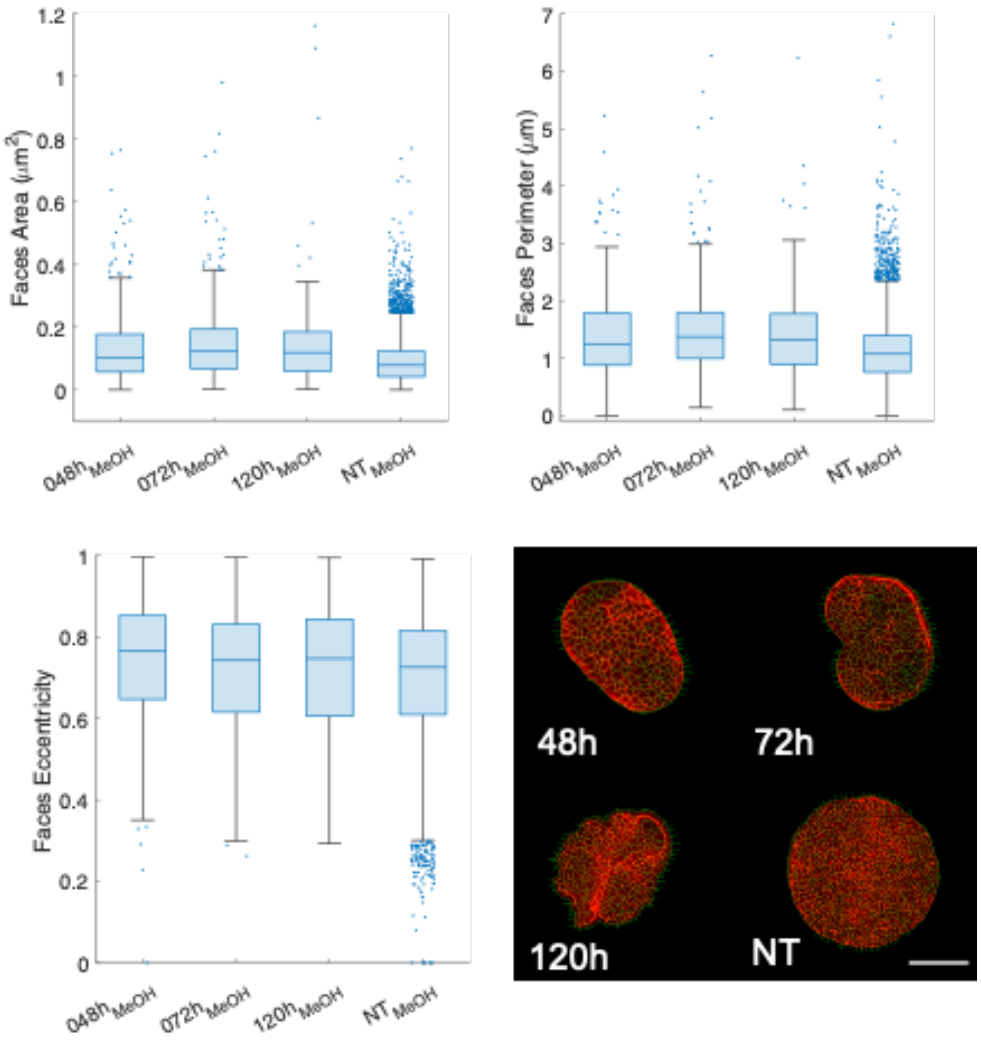

Figure 5.5: Box plot from the distributions of face area, perimeter and eccentricity from Lamin A/C meshworks in PLB985 cells after 48 h, 72 h and 120 h of DMSO exposure and non treated (NT) control cells. The distributions corresponds to grouped meshwork statistics of 2 cells from each time interval. For NT cells, the results of 8 cells are grouped. Scale bar = 5 μm

spread shape, which despite not being a characteristic of unactivated mature neutrophils, it is a morphological marker of migrating neutrophils [184]. An example of elongated nucleus in mature neutrophil is shown in bottom right inset of Figure 5.6.

When not kept under an inert gas atmosphere, DMSO oxidizes within days [185]. When oxidazed DMSO is put in contact with cells, it can induce small calcium fluxes [186], which further activates mature neutrophils [187, 188]. A recent study with HL-60 DMSO differentiated neutrophils, showed that under activation, the cells displayed disorganized migratory directions [189] as we have also seen in DMSO differentiated PLB985 cells (Figure 5.6). This further

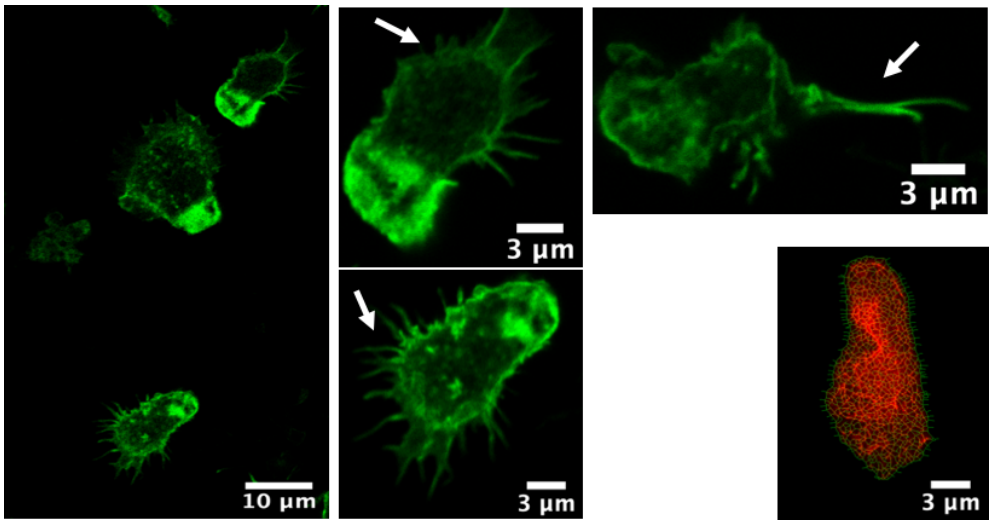

Figure 5.6: Confocal images of differentiated neutrophil cells after 96 h of DMSO exposure showing the formation of polarized lamellipodia. Cells were labeled with STARGREEN-phalloidin for F-actin. On the bottom right, STED image of a nucleus morphology of one cell after 96 h of DMSO exposure labeled against Lamin A/C (in red) and the extracted meshwok (in green).

corroborates the hypothesis that differentiated neutrophils have been activated by DMSO oxidation and developed polarized lamellipodia phenotype.

5.4 CONCLUSION AND PROSPECTIVES

Preliminary results have shown that nuclear morphological changes during neutrophil differentiation are associated with structural changes in the Lamin A/C meshwork, implicating a general meshwork enlargement. The accidental neutrophil activation raised up a new question for the investigated topic: how the arrangement of Lamin A/C meshwork changes during neutrophil migration? Moreover, it has been shown that the Lamin A/C content of neutrophils nuclear envelope has a stronger influence than nuclear morphology on the ability of neutrophils to pass through constrictions. Low lamin A/C content of neutrophil nuclei has been associated to both high speed of neutrophil migration and the short lifespan of these cells [165]. Lamin A/C has a great influence on neutrophil nuclear morphology and functioning, further research into the role of lamin A/C in the molecular basis on neutrophils nuclear deformability will advance our understanding of the morphological aspects of cell biology, and possibly contribute to new therapeutic approaches.

6

DHM FOR URINALYSIS

In this chapter, I will present the results of the use of DHM as a label-free technique to perform fast screening urinalysis. Due to its capability of quantifying phase changes along an optical path, the detection and recognition of urine components was possible. Leukocyturia and bacteriuria analysis of the urine samples were performed and morphological markers were used to characterize urine cellular constituents.

6.1 INTRODUCTION/ MOTIVATION

Urine is formed in the kidneys through blood filtration. It is then passed through the ureters to the bladder, where it is stored. During urination, the urine goes from the bladder through the urethra to be then expelled from the body. Normally, urine is composed of 95% water and 5% solutes (urea and other organic and inorganic chemicals, shown in Table 6.1). Considerable variations in the concentrations of these solutes can occur owing to the influence of factors such as dietary intake, physical activity, body metabolism and endocrine functions [32].

In urinalysis, the content of a urine sample is evaluated and should include physical, chemical, and microscopic examinations. Physical examination of urine comprises the determination of the urine color, clarity, odor, volume, and specific gravity/ osmolality [190]. In chemical examination, semiquantitative and qualitative tests are performed on reagent strips and tablets. It allows the identification of protein, blood cells, glucose, pH, bilirubin, urobilinogen, ketone bodies, nitrites, and leukocyte esterase. The third part of routine urinalysis is the microscopic examination of urinary sediments, when all non soluble components of urine are isolated through centrifugation and observed under the microscope [191].

Microscopic examination consists on the analysis of urinary sediment. Its purpose is to detect and to identify insoluble materials present in the urine. The blood, kidney, lower genitourinary tract, and external contamination contribute to urine elements, which comprises RBCs, WBCs, epithelial cells, casts, bacteria, yeast, parasites, mucus, spermatozoa and crystals (listed in Table 6.2). Since some of these components are of no clinical significance and others are considered normal unless they are present in increased amounts, examination of the urinary sediment must include both *identification* and *quantitation* of the elements present. There are different manual methods for urine sediment examination such as counting in a standardized or non-standardized way under a coverslip or counting of centrifuged or uncentrifuged urine specimens in a

Table 6.1: Primary Soluble Components in Normal Urine

Component	***Comment***
Urea	Primary organic component. Product of protein and amino acid metabolism
Creatinine	Product of creatine metabolism by muscles
Uric acid	Product of nucleic acid breakdown in food and cells
Chloride	Primary inorganic component.
Sodium	Primarily from salt, varies by intake
Potassium	Combined with chloride and other salts
Phosphate	Combines with sodium to buffer the blood
Ammonium	Regulates blood and tissue fluid acidity
Calcium	Combines with chloride, sulfate, and phosphate

chamber [192].

Manual microscopic sediment examination is labor-intensive, time-consuming, and lacks standardization in high-volume laboratories [190]. The potential variables in the microscopic examination of the urine are the speed and time of centrifugation, the amount of urine remaining in the tube for resuspension, and whether urine is stained [192]. In this context, automatic urine analyzers for high-volume laboratories were developed in order to provide better standardization, improve the certainty of measurement and save staff time.

Two main technologies are used to completely or semi-automatically analyze insoluble urine components: digital imaging and flow cytometry. Digital imaging analyzers relays on laminar flow to record the urine components imaged by a camera detector, while algorithms and software are designed to classify and quantify them. Each particle is categorized based on characteristics, such as shape, contrast, and texture. After classification by the instrument, the operator has the possibility to reclassify or correct the obtained images in the correct categories [193].

Flow cytometry utilizes scattered light to count and profile cells in a heterogenous fluid mixture. A suspension of disperse single, unclumped cells run one at a time, through a laser beam. Each particle is then analyzed for visible light scatter and one or multiple fluorescence parameters, when labeled. Usually, visible light scattered is measured in two different directions, the forward direction (Forward Scatter) which can indicate the relative size of the cell, and at 90^o (Side Scatter or SSC) which indicates the internal complexity or granularity of the cell [194]. In the newest systems, side fluorescent light, and

Table 6.2: Non soluble urine components, morphological description and clinical relevance

Component	Appearance	Clinical Significance
RBCs	Round biconcave disks with $\approx 7\,\mu m$ diameter.	Demage on glomerular membrane or vascular injury within the UT.
WBCs	Round disks with $\approx 12\,\mu m$.	UTI and renal transplant rejection.
Squamous Cells	Rectangular $\approx 60\,\mu m$.	No clinical significance.
Transitional Cells	Spherical, polyhedral, or caudate with centrally located nucleus.	Malignancy or viral infection.
RTE Cells	Rectangular, columnar, round, oval or, cuboidal with an eccentric nucleus.	Necrosis of the renal tubules.
Bacteria	Spherical $\approx 0.6 - 2.5\,\mu m$ or rods $\approx 1 - 5\,\mu$.	Urinary tract Infection
Yeast	Oval $\approx 2 - 10\,\mu m$, refractile structures with buds and/or mycelia.	Diabetes, immunodepression and vaginal moniliasis
Parasites	Varies with the parasite type.	Bladder cancer or sexually transmitted diseases.
Spermetozoa	Tapered oval head with long, thin tail.	No clinical significance
Crystals	Geometrically formed or amorphous structures.	Liver disease, inborn errors of metabolism, or renal damage.
Mucus	Single or clumped threads with a low RI.	No clinical significance.

depolarized side scattered light analysis have also been introduced [195].

From both mentioned urinalysis approaches, only flow cytometry allows the bacterial classification [196]. Automated bacteriuria screening tests have been proposed to avoid unnecessary bacterial culture, which is still the "gold standard" for diagnosis [197]. The biggest drawback from agar plate culture method is the required $12h - 28h$ incubation time to give a result when the initial bacterial concentration is low, which represents approximately 80% of the cases [198].

The laboratory diagnosis of urinary tract infection (UTI) is based on the detection and quantification of bacteria (bacteriuria) and leukocytes (leukocyturia) in urine. The presence of bacteria in the urine does not necessarily diagnose a UTI, as bacteriuria may also result from contamination of the sample or from normal bacterial colonization of the urethra. The presence of urinary leukocytes is often associated with UTI but may also derive from vaginal contamination in women [197]. The amount of bacteria that defines a "relevant bacterial growth" from urine culture is typically 10^5 or more colony forming units (CFU) per ml of up to two bacterial species, although lower thresholds exist in particular for vulnerable patients or sterile sampling conditions [199], [200], [201]. The cut-off value for WBCs is, in turn, $100\,cells/mL$, which can be reduced to $65\,cells/mL$ if the patient is symptomatic and presents positive bacteriuria [197].

The work presented in this chapter was aimed to investigate the usefulness of DHM as possible technique for fast screening for both bacteriuria and leukocyturia, however, it brings evidence that the screening can be extended also for others insoluble elements (such as listed in Table 6.2).

Being a QPI technique, DHM allows quantitative phase imaging of low contrast objects such as cells (including bacteria), allowing its detection. Further it brings additional parameters derived from the OPD to cell classification, and consequently its quantification. This characteristics makes DHM a complementary technique to digital imaging and flow cytometry, once it enable bacteria detection, does not require sample preparation or labeling.

6.2 MATERIALS AND METHODS

6.2.1 *Sample Preparation*

Urine samples were provided by the Department of Infectology of the *Ospedale Maggiore di Trieste* in a laboratory $15\,mL$ falcon tube. The time from the samples collection until their imaging with DHM varied from $6h$ to $72h$; meanwhile they were stored at $4^o\,C$. Before imaging, the samples were kept in room temperature and each sample was manually homogenized by shaking the tube for 3 seconds. The input tube of the syringe pump (Parker Smart Syringe Pump, Parker Hannifin Corporation, US) was inserted in the middle

of the sample tube containing the urine. Then, $500\,\mu L$ of urine was taken to fill the pump reservoir and was disposed at $1000\,\mu L/s$ to fill the pump and capillary tubing system. Then, more $500\,\mu L$ of sample was taken to fill the reservoir again and the urine was fluxed to the capillary and imaged with a flow of $10\,\mu L/min$ for about 20 to 30 seconds. After each measurement the entire tubing system was cleaned by flowing two times commercial sodium hypochlorite solution and two times milliQ water.

6.2.2 *Digital Holographic Microscopy for Urine screening*

We used a customized DHM off-axis configuration, based on a Mach-Zehnder interferometer [17, 21]. The laser beam ($520\,nm$, max $20\,mW$) from a diode laser (LP520-SF15, Thorlabs Inc.) is split into two beams with a 50:50 fiber couple (TW560R3F1, Thorlabs Inc.): one passes through the capillary chamber and other is used as a reference (Figure 6.1a). The objective lens (OL) is placed in an afocal-telecentric configuration with a tube lens (TL) to produce directly a plane wavefront in the object arm [71]. Similarly, fiber's output responsible for the reference beam is also placed in a distance equal to the focal lenght, f_{TL} of the TL, producing a plane reference wave on the CMOS (CS2100M-USB,Thorlabs Inc.) detector shown in Figure 6.1b.

A linear neutral density filter (NDF) (NDC-50C-4M-A, Thorlabs Inc.) is placed after the reference beam to control the laser intensity: since the object beam is attenuated after passing through the capillary, the reference needs to be also compensate so both beams have comparable intensities on the detector. A cube beam splitter (BS) is set after the sample chamber to combine both object and references in the same optical path. The urine passes trough a borosilicate glass capillary of $0.8\,mm$ internal diameter and $1\,mm$ external diameter, holden by a customised metallic chamber shown in Figure 6.1a.

The movies were recorded at 60 frames per second, with the camera sensor's exposure time of of $2.5\,ms$ and illuminated with a laser power $< 1\,mW$. The NDF had an optical density (OD) equal to 3.478. The recorded video images had 16-bit depth. The acquisition frame rate was chosen so objects flowing at $10\,\mu mL/min$ could be detected in at least 4 frames, so not only the shape, but also the average flowing velocity of the object could be measured and additional information of the object density could be extracted.

The samples were classified according to bacteria and leukocytes concentration and divided in six groups: negative leukocyturia and bacteriuria (G1), positive leukocyturia and negative bacteriuria (G2), positive leukocyturia and positive bacteriuria at high concentration (G3), negative leukocyturia and positive bacteriuria at high concentration (G5) and negative leukocyturia and positive bacteriuria, shown in Table 6.3.

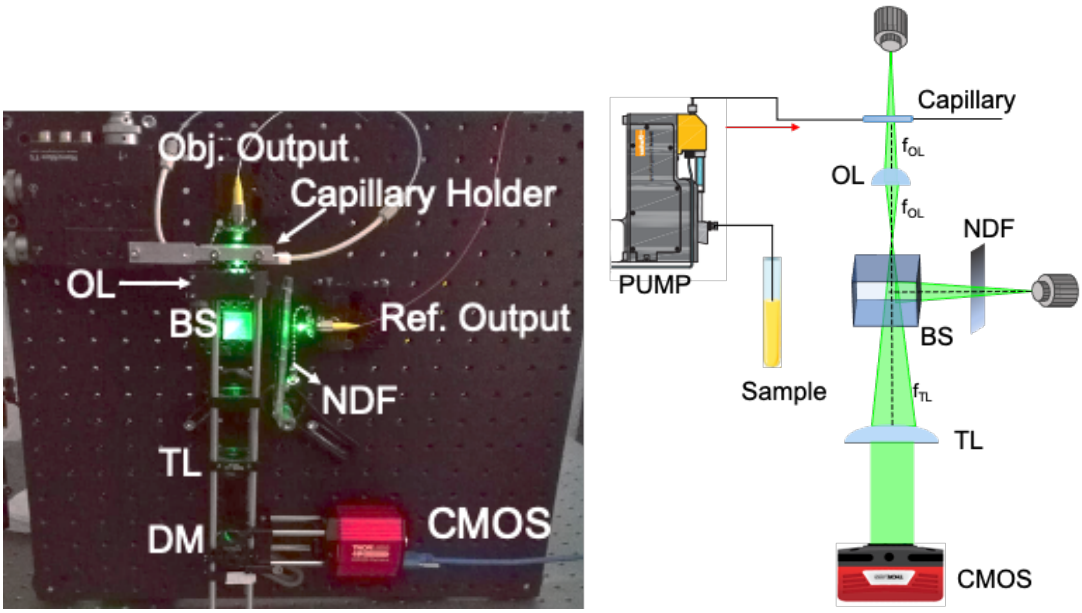

(a) Picture of DHM setup (b) Setup schematic

Figure 6.1: a)Picture of DHM compact setup mounted in a $(450\,mm)^2$ optical breadboard showing fluidic system and the capillary chamber. (b) Schematic of the setup: The reference beam passes trough the capillary and hits the objective lens (OL), goes through the cube beam splitter (BS), the tube lens (TL) and is redirected to the CMOS. The reference beam crosses a neutral density filter (NDF), hits the BS and is combined with the object wave with an offset angle. A dichroic mirror (DM) placed after the TL redirects the beams to the camera sensor and allowing a second camera to be coupled to the setup for bright field or fluorescence imaging.

6.2.3 *Bacteria Concentration Estimation*

The samples were divided in two categories after the visual inspection of the presence or absence of speckle in the original hologram images: highly positive (non countable bacteria) or low positive/negative (countable bacteria).

The analysis of variations of laser light scattered from biological samples is known as biospeckle. It has been broadly used to detect the presence and estimate the concentration of bacteria for food quality inspection [202, 203], [204] and to asses antibacterial susceptibility and growth [205–207]. Real-time measurements techniques for speckle image analysis have also been proposed recently[208–210]. In the mentioned works, the bacteria detection and estimation is done in a steady (non flowing regime) and the bacterial activity is correlated with temporal speckle changes. Two main parameters are considered to describe biospeckle analysis for bacterial growth in suspension: the speckle grain size and speckle spatial contrast [209].

Table 6.3: Groups for urine classification considering positive and negative values for leukocyturia and negative, positive and highly positive values for bacteriuria. Leukocyturia $-$ means $N.Leukocytes < 100\,cells/\mu L$, Leukocyturia $+$ means $N.Leukocytes > 100\,cells/\mu L$, Bacteriuria $-$ means $N.Bacteria < 100\,cells/\mu L$, Bacteriuria $++$ means $N.Bacteria > 10000\,cells/\mu L$ and Bacteriuria $+$ means $100\,cells/\mu L < N.Bacteria < 10000\,cells/\mu L$.

Group	Leukocyturia	Bacteriuria
G1	-	-
G2	+	-
G3	+	++
G4	-	++
G5	+	+
G6	-	+

Considering second-order statistics on speckle images, the grain size can be related to the number or the size of the scatterers in the medium [211], then, the evolution of the grain size over time can be correlated with some bacterial activity such as growth or susceptibility. In addition to the speckle grain size, the spatial contrast of the speckle image provides information about the nature of the medium, for example its viscosity [212].

To estimate the bacteria concentration in flowing urine based on both speckle grain size and spatial contrast, the image entropy, as defined in Equation 6.1, was computed for the difference of two consecutive hologram frames. The difference of consecutive frames was preferred instead of taking single frames to minimize the effect of the fringes in the entropy calculation. The same can be done by blocking the reference wave, however this would imply in recording an additional movie to the hologram one. Another option would be to reconstruct only the intensity of the hologram, but some spatial frequencies could be lost in the filtering process Section 2.1.2.2.

Samples of which images presented no speckle pattern (Figure 6.2 first row), the bacteria concentration was estimated by manually counting the bacteria in focus. Samples which its recorded images presented high speckle (Figure 6.2 second row) were classified as highly positive bacteriuria ($++$) and the values of $1000\,cells/\mu L$, $10000\,cells/\mu L$ $100000\,cells/\mu L$ were assigned to the sample, as the estimated bacteria number based on its speckle intensity pattern and image entropy (H).

$$H = -\sum(p * log_2(p)) \tag{6.1}$$

where p is the normalized histogram bins counts from the grayscale image.

Figure 6.2 shows examples of speckle pattern for six urine samples in the negative ($-$ bac. $< 100\,bac./\mu L$) and positve ($++$ bact. $> 1000\,bac./\mu L$) ranges

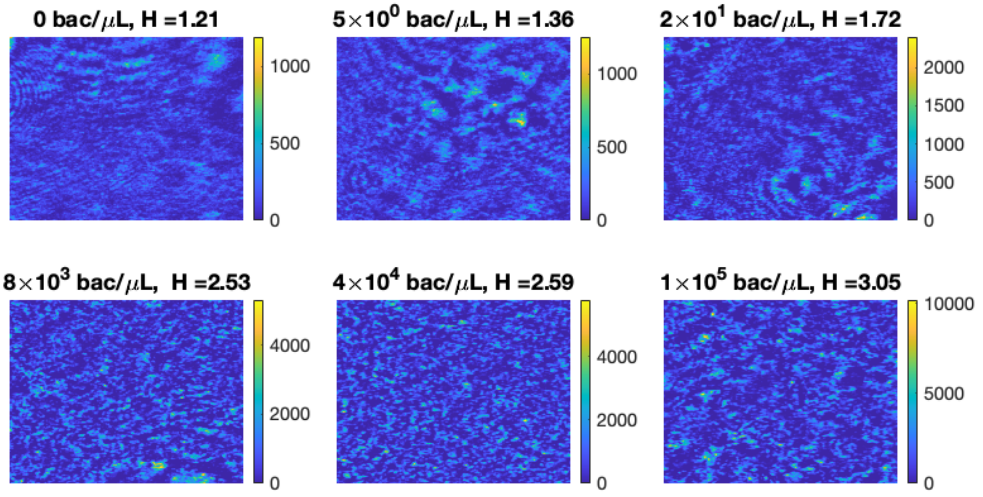

Figure 6.2: Speckle pattern of 6 urine samples. The image shows the subtraction of two consecutive hologram frames $((540\,pixels)^2)$ for each urine sample. The title has the nominal bacteria concentration provided by the hospital measured with UX-2000 (Sysmex, Kobe, Japan) and the measured image entropy.

with its respective entropy calculation. For imaged samples which the field of view contained no visible cells or other urine components, a threshold of image entropy $H > 2$ was considered to designate a positive urine and the assigned value for the bacteria concentration was as described bellow. Samples with $H < 1.8$, the bacteria should be counted considering its morphology and optical phase difference.

Entropy	Bacteria Concentration Level	Procedure
< 1.79	$< 100\,cells/\mu L$	Count bacteria in the sample
$1.8 < H < 2.49$	$1000\,cells/\mu L$	Set counted bacteria in this range
$2.5 < H < 2.69$	$10000\,cells/\mu L$	Set counted bacteria in this range
$2.7 > H$	$100000\,cells/\mu L$	Set counted bacteria in this range

6.2.4 *Optical Phase Difference for Urine Insoluble Components Detection*

Escherichia coli (E. Coli) is the most common causative agent for both uncomplicated and complicated UTIs [213]. For the agents involved in uncomplicated UTIs, E. Coli is followed in prevalence by *Klebsiella pneumoniae*, *Staphylococcus saprophyticus*, *Enterococcus faecalis*, *group B Streptococcus* (GBS), *Proteus mirabilis*, *Pseudomonas aeruginosa*, *Staphylococcus aureus* and *Candida spp.* For complicated UTIs, the order of prevalence for causative agents, following E. coli as most common, is *Enterococcus spp.*, *K. pneumoniae*, *Candida spp.*, *S. aureus*, *P. mirabilis, P. aeruginosa* and GBS [213]. These bacteria that compose urine's microbiome have either an oval (*cocci*) or rod (*bacilli*) shape with a

diameter varying from $0.5\,\mu m - 2.5\,\mu m$ and length ranging from $0.5\,\mu m - 2\,\mu m$ for elongated ones. They appear as single cells or in aggregates as schematically illustrated in Figure 6.3.

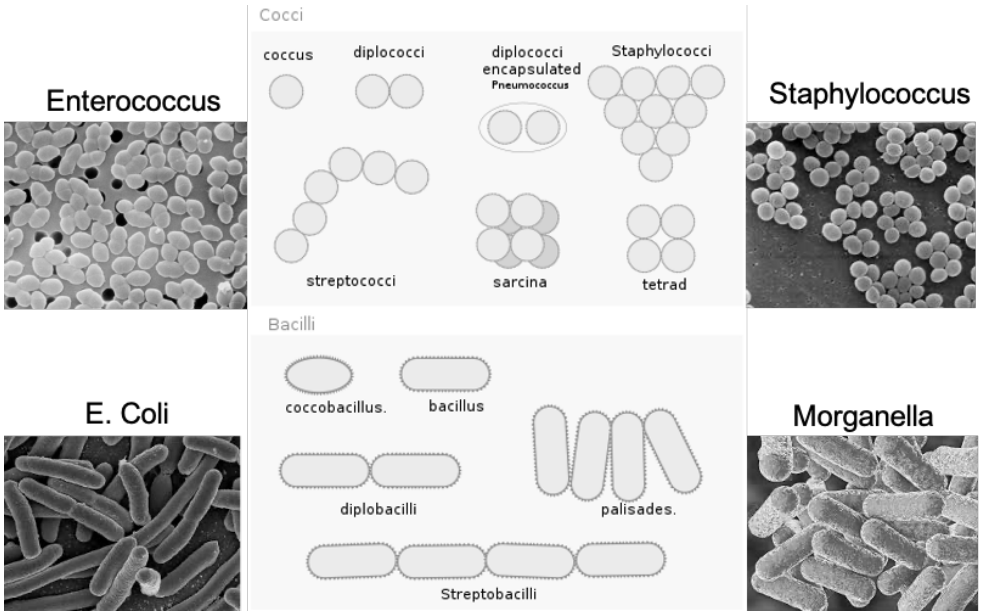

Figure 6.3: Schematic of *cocci*) and (*bacilli* bacteria shape and how they aggregate. Scanning electron microscope images of two cocci and two baccilli bacteria types.

Bacteria have low contrast with respect to the urine, which makes its detection challenging through regular microscopy in non labeled samples. Being a quantitative phase technique, DHM facilitates the detection of bacteria based on its shape and optical phase difference. The estimated refractive index of E. Coli is $n_{Ecoli} = 1.384$ [214], while human urine RI ranges from 1.335 ± 0.001 to 1.339 ± 0.001 depending on its urea concentration [215]. For a bacterium with $1\,\mu m$ radius, the phase variation with respect to the background will be approximately 1.2 radians.

The capillary through which the urine sample is flown has an internal diameter of $0.8\,mm$, while the microscope depth of field is $\approx 2\,\mu m$. Assuming we are able to detect and count only bacteria in focus within a $4\,\mu m$ range and that they flow homogeneously trough the capillary, the investigated volume is approximately $1/200$ of its total. Thus, the total number of bacteria present on the sample is extrapolated by 200 times. RBCs and leukocytes have an average diameter of $7\,\mu m$ and $12\,\mu m$, respectively. Within an $15\,\mu m$ depth, these cells can be detected and recognized, thus the extrapolation value for RBCs and WBCs counting is about 50 times.

6.3 RESULTS AND DISCUSSION

6.3.1 *Bacteriuria and Leukocyturia*

Six groups of urine samples were established, as defined in Table 6.3, and according to the bacteriuria and leukocyturia ranges given by Flow cytometry measurements (UF-2000, Symex). The first group, G1, had negative bacteriuria and leukocyturia with cut-off values of $10^2 cells/\mu L$ and $100 cells/\mu L$, respectively. From 21 samples, only 4 were misclassified according to the numbers of counted leukocytes, however all of them presented the correct bacteriuria range. The second group, G2, (represented by a pink inverted triangle in Figure 6.4) corresponds to positive leukocyturia and negative bacteriuria. In this case, 7 out of 8 samples were correctly classified, while only one stayed on the borderline. For this group most of the samples had the bacteria counting smaller than $1 cells/\mu L$. The third and the fourth group, respectively represented by caramel circles (G3) and green crosses (G4) in Figure 6.4 were the groups with highly positive bacteriuria. All 7 samples belonging to group 3 were categorized correctly. For group G4, 3 out of 4 samples where missclassified due to the leukocytes counting. The last two groups G5 and G6 corresponded to positive bacteriuria, which despite the presence of speckle in the some cases, it was still possible to detect bacteria traveling in focus. G5 was the group which more samples were analysed and were more dispersed being miss classified due to both bacteriuria and leukocyturia results: only 13 out of 21 samples were correctly classified. On the other hand, all 7 samples from G6 were correctly classified for both bacteriuria and leukocyturia estimations.

From the results shown in Figure 6.4 it is possible to see that Leukocyte counts represents the biggest source of misclassification, when bacteriuria and leukocyturia are taken in account to group the samples. This error might be attributed to the amount of cells too far from the focus, the extrapolation value and the total analysed volume: miscounts in the leukocyte quantity (due to out of focus cells), are propagated with extrapolation and becomes more relevant to smaller volumes. When leukocytes are in focus, they can be easily identified due to their well defined nuclear shape, which gets evidenced trough OPD reconstruction [21]. For instance, Figure 6.5 shows the phase reconstruction of two examples of WBCs detected in flowing urine, which's OPD profile presents similar characteristics to mature neutrophils, the predominant type of WBC found in urine sedimentation analysis [32]. We should note that information regarding the cellular nuclear shape would not be available using standard urinalysis imaging techniques without sample staining or labeling. On the other hand, if it is out of focus, WBCs can be confused with round renal tubular epithelial cells, transitional epithelial cells, yeast or big RBCs. Although rare, it might also succeed that more than one urine component passes simultaneously intersecting each other on the field of view, which difficult, if not preclude its identification, since morphological description of the component can not be

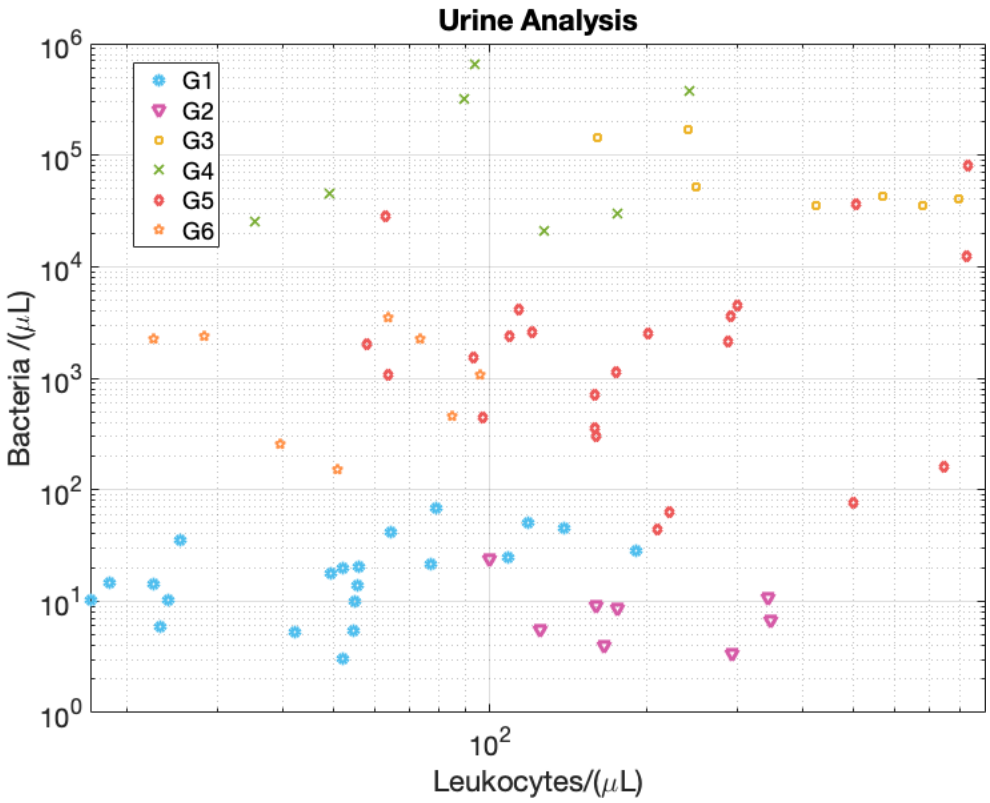

Figure 6.4: Bacteria quantification estimation and leukocytes quantification estimation for urine samples pre-classified in six different groups according to bacteriuria and leukocyturia results given by Flow cytometry measurements (UF-2000, Symex).

done.

The classification regarding bacteria concentration matched the assigned groups for most samples. For urine with more than $10^3\, bac./\mu L$ the presence of speckle and its characterization through image entropy computation demonstrated to be effective in concentration estimation. To our knowledge this technique applied to urine samples has not been reported before. The detection of bacteria in urine for high concentrations ($> 10^3\, bac./\mu L$) is not a challenge in clinical context because its detection can be done even imediatly without the need of urine culture, further this concentration indicates severe UTI probably followed by symptoms such as fever, chills, urgent and/or painful urination [216].

From the results shown in Figure 6.4, all the samples with ($< 10^2\, bac./\mu L$) were correctly classified in its respective groups, considering only bacteria concentration. This result indicates that the DHM can be a suitable candidate for the detection and count of single bacterium in urine. However, the presence of other urine components and artefacts (as described in Table 6.2) makes bacterial recognition challenging and might cause counting discrepancies within the same sample.

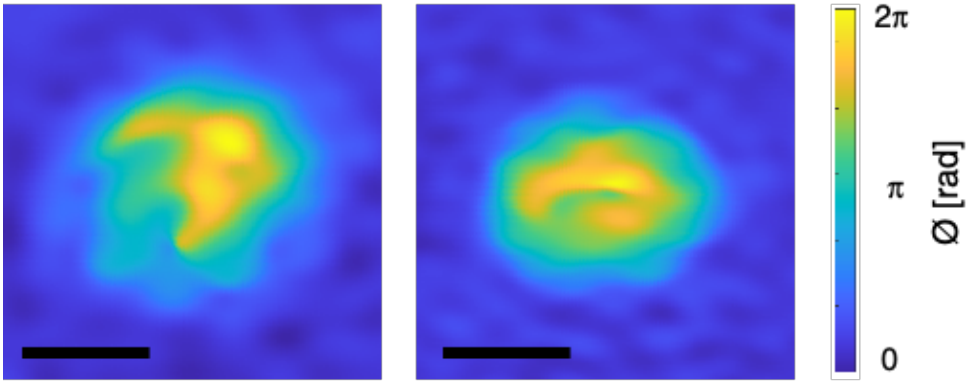

Figure 6.5: Phase reconstruction of White Blood Cells detected in flowing urine. The estimated nuclear region of the cells resembles mature neutrophils. Scale bar $=5\,\mu m$.

Regarding this issue, a software, i. e., image processing solution would be to set a phase threshold to saturate all the components with bigger phase changes than the set value. Then re-scale the image contrast according to the new phase range. In this way, smaller phase objects can be easier identified. A physical solution can be also implemented: the urine samples can be previously filtered, allowing only the passage of small components, as bacteria. However, in both cases, the misclassification of bacteria with others urine artefacts, can not be avoided if the artefact has the same shape, size and causes the same phase retardation as bacteria in urine.

When counting detected bacteria, an important requirement to follow is the minimum analyzed volume. For instance, concentrations of $10\,bac./\mu L$ if in only $1/200$ of the sample volume can be analyzed, this means that at least $20\,\mu L$ of sample should be imaged, so in average at least 1 bacterium should be detect per movie recording. For our first experiments performed only $3-5\mu L$ urine was analyzed and this might have influenced the low bacteria counts matching the low concentration groups.

6.3.2 *Detection of Urine Insoluble Components*

When imaged in focus, urine insoluble components could be reconstructed and characterised according not only to its shape and size, but also considering the derived OPD information. Further, the detection of bacteria in a single cell level in most of the cases was possible only after phase reconstruction, as illustrated in Figure 6.6.
Despite the drawback of bigger storage requirement and longer processing time, the movies recorded at higher frame rates, allows the morphology of the objects to be more accurately inferred. For example, for a sample being flushed at flow rate of $Q = 10\,\mu L/min$ in a capillary with circular cross section with a

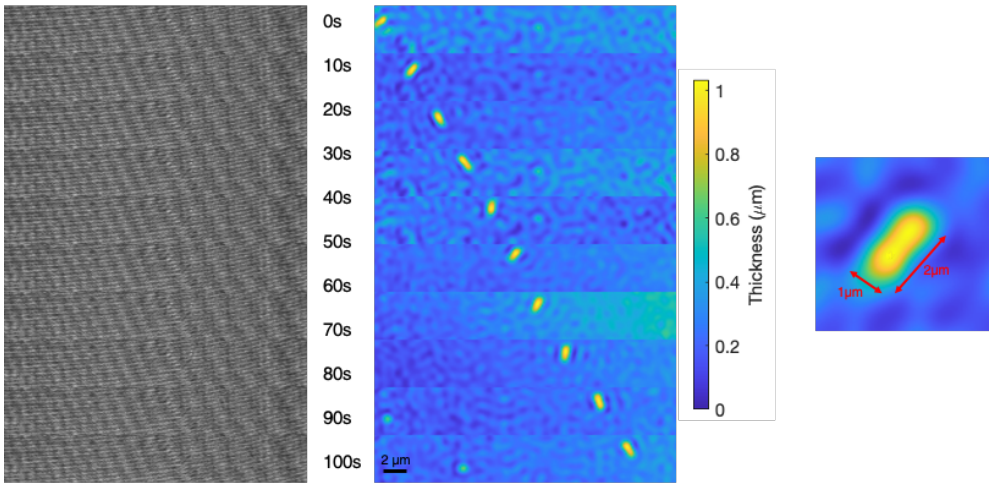

Figure 6.6: Sequence of ten hologram frames (left) and its respective thickness reconstruction (right) taken 10 seconds apart. The assumed RIs for thickness reconstruction were $n_{Ecoli} = 1.384$ and $n_{urine} = 1.335$. On the right, zoomed image of the bacterium in frame number 2 ($10\,s$).

diameter of $\phi = 0.8\,mm$, the average flowing velocity ν, assuming laminar flow regime, will be:

$$\nu = \frac{Q}{\pi r^2} = \frac{10 \cdot 10^{-9}}{\pi(0.8 \cdot 10^{-}3)^2} \approx 20\,mm/min \approx 333\,\mu m/s. \tag{6.2}$$

Considering a square frame window of $(150\,\mu m)^2$, this means that a particle within the urine with an average velocity of $333\,\mu m/s$ would need almost half a second to cross the field of view. So, a frame rate of 2 frames per second should be enough to image each particle at least once, while crossing the field of view. For samples which its morphology can be ambiguous depending on the imaging view, despite the phase information, it is useful to have the sample imaged more than once.

Figure 6.6, exemplifies the cases which the same bacterium is sequentially imaged in different frames. Given the object length ($\approx 2\,\mu m$), thickness $\approx 1\,\mu m$ and single occurrence (i. e.no chains, or pairs formation), we might infer that this is an *E. Coli*, since this is the most abundant microbial cell in urine [217]. In the same figure, on the bottom left corner of the last two frames (at times $90\,s$ and $100\,s$) a second bacterium appears out of focus, travelling about 3 times faster than the first one. This represents the cases, where objects are assigned to be bacteria (due to their size and OPD), but no further information regarding its type can be deduced based on its morphology.

Not only bacteria and WBCs could be identified, but also epithelial cells, casts, mucus, yeast and RBCs. Also crystals could be detected, however their presence would cause phase reconstruction errors. In overall, the usefulness of additional phase information for low contrast/ transparent objects such as bacteria in urine was confirmed.

In prospective steps, the total investigated sample volume should be increased to avoid undersampling of bacteria count. Alternatively, the ratio analysed volume in focus over total flown volume should be decreased. The automatization of urine components detection and counting as is done in [193] is required to extend the technique for clinical usage. In overall, as first proof of concept, DHM showed to be a promising tool for urinalysis because it allows fast screening and urine components identification.

7

CONCLUSIONS AND FUTURE PROSPECTS

In this thesis, three new applications for the usage of label-free markers in the analysis of body fluid cellular constituents have been presented. More than one microscopic technique to derive the same biomarker was used, which besides reinforcing the findings, brought also complementary useful information. Moreover, the supramolecular structural basis of one morphological marker has been shown with unprecedented resolution.

Digital holographic microscopy and optical tweezers were applied to the characterization of ex-vivo generated and native red blood cells. Membrane deformability was associated with the quantification of cell membrane fluctuations and cellular phenotipical changes. More deformable cells presented higher membrane fluctuations and cellular morphology in conformity with native red blood cells. Oscillatory Optical tweezers allowed the investigation of the cell membrane fluctuations while the cells were subjected to forces comparable to the ones present in blood stream. With digital holographic microscopy, cell membrane fluctuations were measured for several cells contemporarily, allowing high throughput. Further, due to the additional phase information, morphological parameters such as membrane height and cell sphericity could be measured.

In a second application, neutrophils precursors were characterized and classified according to its cellular and nuclear morphology during ex-vivo granulocytic differentiation. An automatic segmentation method was proposed to estimate the nuclear region based on optical phase changes within the cell. The projected surface area, optical volume and circularity were measured for each cell, then together with the ratios nucleus to cell for the projected area and optical volume, were shown to be suitable morphological markers. The obtained results suggests that a combination of the parameters derived by means of DHM in a multiparameter testing scheme allows to characterize and monitor the stages of the cell differentiation. Although the use of DHM has been already proposed to distinguish between different leukocytes types and neutrophil differentiation classification has been applied to stained cells, it was the first time that a completely automatic and label-free method was used to classify neutrophils during differentiation.

In a third proposed application, digital holographic microscopy was used to perform fast screening urinalysis. Due to its capability of quantifying phase changes along an optical path, the detection and recognition of urine components was possible. Leukocyturia and bacteriuria analysis of the urine samples were performed and morphological markers showed to be useful to identify urine cellular constituents.

The morphological characterization of both RBCs and Neutrophils can be extended to detect circulating tumour cells (CTCs) in blood. Besides morphological evaluations, the quantitative phase-contrast map supply information on the whole cell inner structure at single cell level, thus allowing the identification of all-optical fingerprints directly connected with biophysical parameters as the hemoglobin content in RBCs or the physical changes connected with biological processes as differentiation. Further, DHM can be easily integrated with microfluidics and artificial intelligence for high-throughput and real-time analysis. The development of a nondestructive unlabeled CTCs methodology for heterogeneous CTCs populations could have clinically significant outcomes for optimizing precision medicine.

The automatic urine screening proposed for urinalysis can also be broaden to diagnosis of urothelial carcinoma in urine specimens based on cytomorphology. As in the case of blood biopsy, DHM integrated with microfluidcs and artificial intelligence can derive an accurate, noninvasive, label-free, and low-cost test for both screening high-risk populations and monitoring patients with a history of bladder cancer to help in identifying recurrence early and preventing disease progression. As was demonstrated for the neutrophils, DHM can be used to assess the urothelial cell nuclear phenotype, including dry mass which can serve as quantitative marker for urothelial neoplasia.

To conclude, different applications which can benefit from label-free markers for single cell and fast screening liquid biopsy have been addressed. The most suitable set of markers and which microscopic technique is more appropriated should be chosen according to each specific biological problem. Mechanical and phenotypical label-free biological markers can be exploited for different biological problems and are not restricted only to the biological applications presented in this Thesis. All the presented methods for the extraction and analysis of label-free markers presented here can be extended to other liquid biopsy analysis and have research and clinical potential.

BIBLIOGRAPHY

[1] SB Hulka. "Overview of biological marker." In: *Biological markers in epidemiology.* (1990), pp. 3–15.

[2] Stephen Naylor. "Biomarkers: current perspectives and future prospects." In: *Expert review of molecular diagnostics* 3.5 (2003), pp. 525–529.

[3] Furong Niu et al. "Potentials of single-cell biology in identification and validation of disease biomarkers." In: *Journal of cellular and molecular medicine* 20.9 (2016), pp. 1789–1795.

[4] Dino Di Carlo. "A mechanical biomarker of cell state in medicine." In: *Journal of laboratory automation* 17.1 (2012), pp. 32–42.

[5] Prajokta Ray and Andrew J Steckl. "Label-free optical detection of multiple biomarkers in sweat, plasma, urine, and saliva." In: *ACS sensors* 4.5 (2019), pp. 1346–1357.

[6] Xiaole Mao and Tony Jun Huang. "Exploiting mechanical biomarkers in microfluidics." In: *Lab on a Chip* 12.20 (2012), pp. 4006–4009.

[7] Grannum R Sant et al. "Live-single-cell phenotypic cancer biomarkers-future role in precision oncology?" In: *NPJ precision oncology* 1.1 (2017), pp. 1–7.

[8] Richard Mayeux. "Biomarkers: potential uses and limitations." In: *NeuroRx* 1.2 (2004), pp. 182–188.

[9] Emad Moeendarbary and Andrew R Harris. "Cell mechanics: principles, practices, and prospects." In: *Wiley Interdisciplinary Reviews: Systems Biology and Medicine* 6.5 (2014), pp. 371–388.

[10] Kelly Molnar and Michel Labouesse. "The plastic cell: mechanical deformation of cells and tissues." In: *Open Biology* 11.2 (2021), p. 210006.

[11] Ju Li et al. "Cytoskeletal dynamics of human erythrocyte." In: *Proceedings of the National Academy of Sciences* 104.12 (2007), pp. 4937–4942.

[12] Gabriel YH Lee and Chwee T Lim. "Biomechanics approaches to studying human diseases." In: *Trends in biotechnology* 25.3 (2007), pp. 111–118.

[13] Subra Suresh. "Biomechanics and biophysics of cancer cells." In: *Acta biomaterialia* 3.4 (2007), pp. 413–438.

[14] Subra Suresh et al. "Connections between single-cell biomechanics and human disease states: gastrointestinal cancer and malaria." In: *Acta biomaterialia* 1.1 (2005), pp. 15–30.

[15] Wenwei Xu et al. "Cell stiffness is a biomarker of the metastatic potential of ovarian cancer cells." In: *PloS one* 7.10 (2012), e46609.

[16] Damir B Khismatullin. "The cytoskeleton and deformability of white blood cells." In: *Current topics in membranes* 64 (2009), pp. 47–111.

[17] Claudia Bernecker et al. "Biomechanics of Ex Vivo-Generated Red Blood Cells Investigated by Optical Tweezers and Digital Holographic Microscopy." In: *Cells* 10.3 (2021), p. 552.

[18] Timo Betz et al. "ATP-dependent mechanics of red blood cells." In: *Proceedings of the National Academy of Sciences* 106.36 (2009), pp. 15320–15325.

[19] Monica Diez-Silva et al. "Shape and biomechanical characteristics of human red blood cells in health and disease." In: *MRS bulletin* 35.5 (2010), pp. 382–388.

[20] Harriet R Manley et al. "The neutrophil nucleus: an important influence on neutrophil migration and function." In: *Frontiers in immunology* 9 (2018), p. 2867.

[21] Maria Augusta do RBF Lima and Dan Cojoc. "Monitoring Human Neutrophil Differentiation by Digital Holographic Microscopy." In: *Frontiers in Physics* 9 (2021), p. 190.

[22] Fengzhu Xiong et al. "Interplay of cell shape and division orientation promotes robust morphogenesis of developing epithelia." In: *Cell* 159.2 (2014), pp. 415–427.

[23] Ross A Marklein et al. "Functionally-relevant morphological profiling: a tool to assess cellular heterogeneity." In: *Trends in biotechnology* 36.1 (2018), pp. 105–118.

[24] Faliu Yi et al. "Cell morphology-based classification of red blood cells using holographic imaging informatics." In: *Biomedical optics express* 7.6 (2016), pp. 2385–2399.

[25] Nipon Theera-Umpon and Sompong Dhompongsa. "Morphological granulometric features of nucleus in automatic bone marrow white blood cell classification." In: *IEEE Transactions on Information Technology in Biomedicine* 11.3 (2007), pp. 353–359.

[26] Björn Kemper et al. "Quantitative phase imaging-based concepts for the analysis of global morphology changes in confluent cell layers." In: *Quantitative Phase Imaging V*. Vol. 10887. International Society for Optics and Photonics. 2019, p. 108871M.

[27] Ying Li et al. "Classification of cell morphology with quantitative phase microscopy and machine learning." In: *Optics Express* 28.16 (2020), pp. 23916–23927.

[28] José Marrugo-Ramírez et al. "Blood-based cancer biomarkers in liquid biopsy: a promising non-invasive alternative to tissue biopsy." In: *International journal of molecular sciences* 19.10 (2018), p. 2877.

[29] Martin HD Neumann et al. "ctDNA and CTCs in liquid biopsy–current status and where we need to progress." In: *Computational and structural biotechnology journal* 16 (2018), pp. 190–195.

[30] Wei Zhang et al. “Liquid biopsy for cancer: circulating tumor cells, circulating free DNA or exosomes?” In: *Cellular Physiology and Biochemistry* 41.2 (2017), pp. 755–768.

[31] Yatian Fu et al. “Liquid biopsy technologies for hematological diseases.” In: *Medicinal Research Reviews* 41.1 (2021), pp. 246–274.

[32] Susan King Strasinger and Marjorie Schaub Di Lorenzo. *Anlisis de orina y de los lquidos corporales/Urinalysis and body fluids*. Ed. Médica Panamericana, 2010.

[33] Xiangyu Quan et al. “Multimodal Microscopy: Fast Acquisition of Quantitative Phase and Fluorescence Imaging in 3D Space.” In: *IEEE Journal of Selected Topics in Quantum Electronics* 27.4 (2020), pp. 1–11.

[34] Jerome Mertz. *Introduction to optical microscopy*. Cambridge University Press, 2019.

[35] Caitlin Smith. “Two microscopes are better than one.” In: *Nature* 492.7428 (2012), pp. 293–297.

[36] Nicolas Pavillon et al. “Noninvasive detection of macrophage activation with single-cell resolution through machine learning.” In: *Proceedings of the National Academy of Sciences* 115.12 (2018), E2676–E2685.

[37] Jeon Woong Kang et al. “Combined confocal Raman and quantitative phase microscopy system for biomedical diagnosis.” In: *Biomedical optics express* 2.9 (2011), pp. 2484–2492.

[38] Jacques Klossa et al. “Quantitative phase imaging and Raman microspectroscopy applied to malaria.” In: *Diagnostic pathology*. Vol. 8. 1. BioMed Central. 2013, pp. 1–4.

[39] Xiangyu Quan et al. “Phase and fluorescence imaging by combination of digital holographic microscopy and fluorescence microscopy.” In: *Optical Review* 22.2 (2015), pp. 349–353.

[40] Etienne Shaffer et al. “Single-shot, simultaneous incoherent and holographic microscopy.” In: *Journal of microscopy* 245.1 (2012), pp. 49–62.

[41] Xuejing Chen et al. “Dual-wavelength digital holographic phase and fluorescence microscopy combining with Raman spectroscopy for microquartz pieces-based dual-channel encoded suspension array.” In: *Optics express* 27.3 (2019), pp. 1894–1910.

[42] Ruei-Yu He et al. “Imaging live cell membranes via surface plasmon-enhanced fluorescence and phase microscopy.” In: *Optics express* 18.4 (2010), pp. 3649–3659.

[43] Kalle Hanhijärvi et al. “Simultaneous TIRF Microscopy and Optical Trapping for Single Molecule Experiments.” In: *Biophysical Journal* 100.3 (2011), 138a.

[44] Tatsuki Tahara et al. “Digital holography and its multidimensional imaging applications: a review.” In: *Microscopy* 67.2 (2018), pp. 55–67.

[45] Myung K Kim. "Principles and techniques of digital holographic microscopy." In: *SPIE reviews* 1.1 (2010), p. 018005.

[46] Pierre Marquet et al. "Digital holographic microscopy: a noninvasive contrast imaging technique allowing quantitative visualization of living cells with subwavelength axial accuracy." In: *Optics letters* 30.5 (2005), pp. 468–470.

[47] Xiao Yu et al. "Review of digital holographic microscopy for three-dimensional profiling and tracking." In: *Optical engineering* 53.11 (2014), p. 112306.

[48] Pierre Marquet et al. "Review of quantitative phase-digital holographic microscopy: promising novel imaging technique to resolve neuronal network activity and identify cellular biomarkers of psychiatric disorders." In: *Neurophotonics* 1.2 (2014), p. 020901.

[49] Björn Kemper and Gert Von Bally. "Digital holographic microscopy for live cell applications and technical inspection." In: *Applied optics* 47.4 (2008), A52–A61.

[50] Myung K Kim. "Digital holographic microscopy." In: *Digital Holographic Microscopy*. Springer, 2011, pp. 149–190.

[51] Dennis Gabor. "A new microscopic principle." In: *nature* 161 (1948), pp. 777–778.

[52] Theodore H Maiman et al. "Stimulated optical radiation in ruby." In: (1960).

[53] Emmett N Leith and Juris Upatnieks. "Reconstructed wavefronts and communication theory." In: *JOSA* 52.10 (1962), pp. 1123–1130.

[54] URL: https://photos.aip.org/history-programs/niels-bohr-library/photos.

[55] Joseph W Goodman and RW Lawrence. "Digital image formation from electronically detected holograms." In: *Applied physics letters* 11.3 (1967), pp. 77–79.

[56] Ulf Schnars and Werner Jüptner. "Direct recording of holograms by a CCD target and numerical reconstruction." In: *Applied optics* 33.2 (1994), pp. 179–181.

[57] Thomas Kreis. *Handbook of holographic interferometry: optical and digital methods*. John Wiley & Sons, 2006.

[58] Emilia Mihaylova. "Holography: basic principles and contemporary applications." In: (2013).

[59] Joseph W Goodman. *Introduction to Fourier optics*. Roberts and Company Publishers, 2005.

[60] Kevin J Chalut et al. "Quantifying cellular differentiation by physical phenotype using digital holographic microscopy." In: *Integrative biology* 4.3 (2012), pp. 280–284.

[61] Etienne Cuche et al. “Simultaneous amplitude-contrast and quantitative phase-contrast microscopy by numerical reconstruction of Fresnel off-axis holograms.” In: *Applied optics* 38.34 (1999), pp. 6994–7001.

[62] Etienne Cuche et al. “Spatial filtering for zero-order and twin-image elimination in digital off-axis holography.” In: *Applied optics* 39.23 (2000), pp. 4070–4075.

[63] Ana Doblas et al. “Study of spatial lateral resolution in off-axis digital holographic microscopy.” In: *Optics Communications* 352 (2015), pp. 63–69.

[64] Hassaan Majeed et al. “Quantitative phase imaging for medical diagnosis.” In: *Journal of biophotonics* 10.2 (2017), pp. 177–205.

[65] F Merola et al. “Digital holography as a method for 3D imaging and estimating the biovolume of motile cells.” In: *Lab on a Chip* 13.23 (2013), pp. 4512–4516.

[66] Vicente Micó et al. “Superresolution digital holographic microscopy for three-dimensional samples.” In: *Optics express* 16.23 (2008), pp. 19260–19270.

[67] Vicente Micó et al. “Resolution enhancement in quantitative phase microscopy.” In: *Advances in Optics and Photonics* 11.1 (2019), pp. 135–214.

[68] José Ángel Picazo-Bueno et al. “Single-shot, dual-mode, water-immersion microscopy platform for biological applications.” In: *Applied optics* 57.1 (2018), A242–A249.

[69] Thomas M Kreis. “Frequency analysis of digital holography.” In: *Optical Engineering* 41.4 (2002), pp. 771–778.

[70] Nicolas Verrier and Michael Atlan. “Off-axis digital hologram reconstruction: some practical considerations.” In: *Applied optics* 50.34 (2011), H136–H146.

[71] Emilio Sánchez-Ortiga et al. “Off-axis digital holographic microscopy: practical design parameters for operating at diffraction limit.” In: *Applied optics* 53.10 (2014), pp. 2058–2066.

[72] James L Flewellen. “Digital holographic microscopy for three-dimensional studies of bacteria.” PhD thesis. Oxford University, UK, 2012.

[73] Leslie Ying. “Phase unwrapping.” In: *Wiley Encyclopedia of Biomedical Engineering* (2006).

[74] Dennis C Ghiglia and Mark D Pritt. *Two-dimensional phase unwrapping: theory, algorithms, and software*. Vol. 4. Wiley New York, 1998.

[75] Richard M Goldstein et al. “Satellite radar interferometry: Two-dimensional phase unwrapping.” In: *Radio science* 23.4 (1988), pp. 713–720.

[76] Donald J Bone. “Fourier fringe analysis: the two-dimensional phase unwrapping problem.” In: *Applied optics* 30.25 (1991), pp. 3627–3632.

[77] Smith Carey. *Goldstein Unwrap 2D*. MATLAB Central File Exchange. 2010. URL: https://www.mathworks.com/matlabcentral/fileexchange/29497-goldsteinunwrap2d_r1.

[78] Arthur Ashkin. "Acceleration and trapping of particles by radiation pressure." In: *Physical review letters* 24.4 (1970), p. 156.

[79] Arthur Ashkin et al. "Observation of a single-beam gradient force optical trap for dielectric particles." In: *Optics letters* 11.5 (1986), pp. 288–290.

[80] Arthur Ashkin and James M Dziedzic. "Optical trapping and manipulation of viruses and bacteria." In: *Science* 235.4795 (1987), pp. 1517–1520.

[81] Arthur Ashkin. "The pressure of laser light." In: *Scientific American* 226.2 (1972), pp. 62–71.

[82] Steven Chu. "Laser trapping of neutral particles." In: *Scientific American* 266.2 (1992), pp. 70–77.

[83] Justin E Molloy and Miles J Padgett. "Lights, action: optical tweezers." In: *Contemporary physics* 43.4 (2002), pp. 241–258.

[84] David McGloin. "Optical tweezers: 20 years on." In: *Philosophical Transactions of the Royal Society A: Mathematical, Physical and Engineering Sciences* 364.1849 (2006), pp. 3521–3537.

[85] Jeffrey R Moffitt et al. "Recent advances in optical tweezers." In: *Annu. Rev. Biochem.* 77 (2008), pp. 205–228.

[86] Philip Jones et al. *Optical tweezers*. Cambridge University Press Cambridge, 2015.

[87] Paolo Polimeno et al. "Optical tweezers and their applications." In: *Journal of Quantitative Spectroscopy and Radiative Transfer* 218 (2018), pp. 131–150.

[88] Joost van Mameren et al. "Introduction to optical tweezers: background, system designs, and commercial solutions." In: *Single Molecule Analysis* (2011), pp. 1–20.

[89] Raghbir Singh Khandpur. *Compendium of Biomedical Instrumentation*. John Wiley & Sons, 2019.

[90] David G Grier. "A revolution in optical manipulation." In: *nature* 424.6950 (2003), pp. 810–816.

[91] Yasuhiro Harada and Toshimitsu Asakura. "Radiation forces on a dielectric sphere in the Rayleigh scattering regime." In: *Optics communications* 124.5-6 (1996), pp. 529–541.

[92] Hendrik Christoffel Hulst and Hendrik C van de Hulst. *Light scattering by small particles*. Courier Corporation, 1981.

[93] Gérard Gouesbet and Gérard Gréhan. *Generalized lorenz-mie theories*. Vol. 31. Springer, 2011.

[94] Ferdinando Borghese et al. *Scattering from model nonspherical particles: theory and applications to environmental physics*. Springer Science & Business Media, 2007.

[95] Michael I Mishchenko et al. *Scattering, absorption, and emission of light by small particles*. Cambridge university press, 2002.

[96] Itia A Favre-Bulle et al. "Optical trapping in vivo: theory, practice, and applications." In: *Nanophotonics* 8.6 (2019), pp. 1023–1040.

[97] Hu Zhang and Kuo-Kang Liu. "Optical tweezers for single cells." In: *Journal of the Royal Society interface* 5.24 (2008), pp. 671–690.

[98] Xinming Zhang et al. "High-resolution optical tweezers for single-molecule manipulation." In: *The Yale journal of biology and medicine* 86.3 (2013), p. 367.

[99] CT Lim et al. "Mechanical models for living cells—a review." In: *Journal of biomechanics* 39.2 (2006), pp. 195–216.

[100] Jochen Guck et al. "Optical deformability of soft biological dielectrics." In: *Physical review letters* 84.23 (2000), p. 5451.

[101] Jochen Guck et al. "Stretching biological cells with light." In: *Journal of Physics: Condensed Matter* 14.19 (2002), p. 4843.

[102] R Waugh and Evan A Evans. "Thermoelasticity of red blood cell membrane." In: *Biophysical journal* 26.1 (1979), pp. 115–131.

[103] Ji-Jinn Foo et al. "Human red blood cells deformed under thermal fluid flow." In: *Biomedical Materials* 1.1 (2006), p. 1.

[104] Tatiana Avsievich et al. "The advancement of blood cell research by optical tweezers." In: *Reviews in Physics* 5 (2020), p. 100043.

[105] Ernst Abbe. "Beiträge zur Theorie des Mikroskops und der mikroskopischen Wahrnehmung." In: *Archiv für mikroskopische Anatomie* 9.1 (1873), pp. 413–468.

[106] Max Born and Emil Wolf. *Principles of optics: electromagnetic theory of propagation, interference and diffraction of light*. Elsevier, 2013.

[107] Vicente Micó. "Experimental research on superresolution imaging in digital holographic microscopy by synthetic aperture generation." PhD thesis. Departament d'optica, Facultat de Fisica, Universitat De València, 2008.

[108] Stefan W Hell and Jan Wichmann. "Breaking the diffraction resolution limit by stimulated emission: stimulated-emission-depletion fluorescence microscopy." In: *Optics letters* 19.11 (1994), pp. 780–782.

[109] W Ruchira Silva et al. "Toward label-free super-resolution microscopy." In: *Acs Photonics* 3.1 (2016), pp. 79–86.

[110] Thomas A Klar and Stefan W Hell. "Subdiffraction resolution in far-field fluorescence microscopy." In: *Optics letters* 24.14 (1999), pp. 954–956.

[111] Matthias Jessica. “STED Nanoscopy to Illuminate New Avenues in Cancer Research.” PhD thesis. Combined Faculty of Natural Sciences and Mathematics, Heidelberg University, Germany, 2019.

[112] Giuseppe Vicidomini et al. “STED super-resolved microscopy.” In: *Nature methods* 15.3 (2018), p. 173.

[113] Giorgio Tortarolo et al. “Evaluating image resolution in stimulated emission depletion microscopy.” In: *Optica* 5.1 (2018), pp. 32–35.

[114] Fabian Göttfert et al. “Coaligned dual-channel STED nanoscopy and molecular diffusion analysis at 20 nm resolution.” In: *Biophysical journal* 105.1 (2013), pp. L01–L03.

[115] C Roobala et al. “Applications of STED fluorescence nanoscopy in unravelling nanoscale structure and dynamics of biological systems.” In: *Journal of biosciences* 43.3 (2018), pp. 471–484.

[116] Giampaolo Minetti et al. “Membrane rearrangements in the maturation of circulating human reticulocytes.” In: *Frontiers in physiology* 11 (2020), p. 215.

[117] Claudia Bernecker et al. “Enhanced ex vivo generation of erythroid cells from human induced pluripotent stem cells in a simplified cell culture system with low cytokine support.” In: *Stem cells and development* 28.23 (2019), pp. 1540–1551.

[118] Marie-Catherine Giarratana et al. “Ex vivo generation of fully mature human red blood cells from hematopoietic stem cells.” In: *Nature biotechnology* 23.1 (2005), pp. 69–74.

[119] Kongtana Trakarnsanga et al. “An immortalized adult human erythroid line facilitates sustainable and scalable generation of functional red cells.” In: *Nature communications* 8.1 (2017), pp. 1–7.

[120] Giampaolo Minetti et al. “Continuous change in membrane and membrane-skeleton organization during development from proerythroblast to senescent red blood cell.” In: *Frontiers in physiology* 9 (2018), p. 286.

[121] Rick Huisjes et al. “Squeezing for life–properties of red blood cell deformability.” In: *Frontiers in physiology* 9 (2018), p. 656.

[122] Jeongho Kim et al. “Advances in the measurement of red blood cell deformability: A brief review.” In: *Journal of Cellular Biotechnology* 1.1 (2015), pp. 63–79.

[123] Thierry Savin et al. “Pressure-driven occlusive flow of a confined red blood cell.” In: *Soft matter* 12.2 (2016), pp. 562–573.

[124] Claudia Bernecker et al. “Cholesterol deficiency causes impaired osmotic stability of cultured red blood cells.” In: *Frontiers in physiology* 10 (2019), p. 1529.

[125] Fabio Falleroni et al. “Cell mechanotransduction with piconewton forces applied by optical tweezers.” In: *Frontiers in cellular neuroscience* 12 (2018), p. 130.

[126] Muhammad S Yousafzai et al. "Substrate-dependent cell elasticity measured by optical tweezers indentation." In: *Optics and Lasers in Engineering* 76 (2016), pp. 27–33.

[127] Keyvan Jaferzadeh and Inkyu Moon. "Quantitative investigation of red blood cell three-dimensional geometric and chemical changes in the storage lesion using digital holographic microscopy." In: *Journal of biomedical optics* 20.11 (2015), p. 111218.

[128] Arthur Ashkin. "Forces of a single-beam gradient laser trap on a dielectric sphere in the ray optics regime." In: *Biophysical journal* 61.2 (1992), pp. 569–582.

[129] Jingping Hu et al. "Isolation and functional characterization of human erythroblasts at distinct stages: implications for understanding of normal and disordered erythropoiesis in vivo." In: *Blood, The Journal of the American Society of Hematology* 121.16 (2013), pp. 3246–3253.

[130] Keyvan Jaferzadeh et al. "Quantification of stored red blood cell fluctuations by time-lapse holographic cell imaging." In: *Biomedical optics express* 9.10 (2018), pp. 4714–4729.

[131] MichaelE Miller et al. "Lazy-leucocyte syndrome: A new disorder of neutrophil function." In: *The Lancet* 297.7701 (1971), pp. 665–669.

[132] Robert I Lehrer and Tomas Ganz. "Antimicrobial polypeptides of human neutrophils." In: (1990).

[133] Meir Wetzler et al. "A new familial immunodeficiency disorder characterized by severe neutropenia, a defective marrow release mechanism, and hypogammaglobulinemia." In: *The American journal of medicine* 89.5 (1990), pp. 663–672.

[134] Atsushi Komiyama et al. "Impaired natural killer cell recycling in childhood chronic neutropenia with morphological abnormalities and defective chemotaxis of neutrophils." In: (1985).

[135] Guillaume Carissimo et al. "Whole blood immunophenotyping uncovers immature neutrophil-to-VD2 T-cell ratio as an early marker for severe COVID-19." In: *Nature communications* 11.1 (2020), pp. 1–12.

[136] Olga Pozdnyakova et al. "Clinical significance of CBC and WBC morphology in the diagnosis and clinical course of COVID-19 infection." In: *American journal of clinical pathology* 155.3 (2021), pp. 364–375.

[137] John L Frater et al. "COVID-19 and the clinical hematology laboratory." In: *International journal of laboratory hematology* 42 (2020), pp. 11–18.

[138] Gina Zini et al. "Morphological anomalies of circulating blood cells in COVID-19." In: *American journal of hematology* 95.7 (2020), pp. 870–872.

[139] Lai Guan Ng et al. "Heterogeneity of neutrophils." In: *Nature Reviews Immunology* 19.4 (2019), pp. 255–265.

[140] Charlotte Summers et al. "Neutrophil kinetics in health and disease." In: *Trends in immunology* 31.8 (2010), pp. 318–324.

[141] WT Jr Dalton et al. “HL-60 cell line was derived from a patient with FAB-M2 and not FAB-M3.” In: (1988).

[142] Kent A Tucker et al. “Characterization of a new human diploid myeloid leukemia cell line (PLB-985) with granulocytic and monocytic differentiating capacity.” In: *Blood* 9 (1987), pp. 372–378.

[143] Isaline Boulven et al. “Class IA phosphatidylinositide 3-kinases, rather than p110γ, regulate formyl-methionyl-leucyl-phenylalanine-stimulated chemotaxis and superoxide production in differentiated neutrophil-like PLB-985 cells.” In: *The Journal of Immunology* 176.12 (2006), pp. 7621–7627.

[144] Shaayau Shehu. “Regulation of apoptosis of myeloid immune cells: implication for cancer therapy and inflammation.” PhD thesis. University of Liverpool, 2017.

[145] Malene Digmann Bjerregaard et al. “The in vivo profile of transcription factors during neutrophil differentiation in human bone marrow.” In: *Blood* 101.11 (2003), pp. 4322–4332.

[146] Hiromi Iwasaki and Koichi Akashi. “Myeloid lineage commitment from the hematopoietic stem cell.” In: *Immunity* 26.6 (2007), pp. 726–740.

[147] Jonathan G Lieber et al. “The in vitro production and characterization of neutrophils from embryonic stem cells.” In: *Blood* 103.3 (2004), pp. 852–859.

[148] AV Bezrukov. “Romanowsky staining, the Romanowsky effect and thoughts on the question of scientific priority.” In: *Biotechnic & Histochemistry* 92.1 (2017), pp. 29–35.

[149] Brad Chazotte. “Labeling nuclear DNA with hoechst 33342.” In: *Cold Spring Harbor Protocols* 2011.1 (2011), pdb–prot5557.

[150] Dietmar W Siemann and Peter C Keng. “Cell cycle specific toxicity of the Hoechst 33342 stain in untreated or irradiated murine tumor cells.” In: *Cancer research* 46.7 (1986), pp. 3556–3559.

[151] Noga Nissim et al. “Real-time stain-free classification of cancer cells and blood cells using interferometric phase microscopy and machine learning.” In: *Cytometry Part A* (2020).

[152] Van K Lam et al. “Machine learning with optical phase signatures for phenotypic profiling of cell lines.” In: *Cytometry Part A* 95.7 (2019), pp. 757–768.

[153] Matthias Ugele et al. “Label-free high-throughput leukemia detection by holographic microscopy.” In: *Advanced Science* 5.12 (2018), p. 1800761.

[154] Han Sang Park et al. “Automated detection of P. falciparum using machine learning algorithms with quantitative phase images of unstained cells.” In: *PloS one* 11.9 (2016), e0163045.

[155] N. Otsu. “A Threshold Selection Method from Gray-Level Histograms.” In: *IEEE Transactions on Systems, Man, and Cybernetics* 9.1 (1979), pp. 62–66. DOI: 10.1109/TSMC.1979.4310076.

[156] Deng-Yuan Huang et al. "Automatic multilevel thresholding based on two-stage Otsu's method with cluster determination by valley estimation." In: *International journal of innovative computing, information and control* 7.10 (2011), pp. 5631–5644.

[157] HyunJoo Park et al. "Measuring cell surface area and deformability of individual human red blood cells over blood storage using quantitative phase imaging." In: *Scientific reports* 6 (2016), p. 34257.

[158] DongHun Ryu et al. "Label-free bone marrow white blood cell classification using refractive index tomograms and deep learning." In: *bioRxiv* (2020).

[159] Jan Lammerding. "Mechanics of the nucleus." In: *Comprehensive physiology* 1.2 (2011), pp. 783–807.

[160] Micah Webster et al. "Sizing up the nucleus: nuclear shape, size and nuclear-envelope assembly." In: *Journal of cell science* 122.10 (2009), pp. 1477–1486.

[161] Edgar G Fischer. "Nuclear Morphology and the Biology of Cancer Cells." In: *Acta cytologica* 64.6 (2020), pp. 511–519.

[162] Abul K Abbas et al. *Cellular and molecular immunology E-book*. Elsevier Health Sciences, 2014.

[163] Robert D Goldman et al. "Nuclear lamins: building blocks of nuclear architecture." In: *Genes & development* 16.5 (2002), pp. 533–547.

[164] Thomas Dechat et al. "Nuclear lamins." In: *Cold Spring Harbor perspectives in biology* 2.11 (2010), a000547.

[165] Angela Saez et al. "Lamin A/C and the Immune System: One Intermediate Filament, Many Faces." In: *International Journal of Molecular Sciences* 21.17 (2020), p. 6109.

[166] Eric C Schirmer and Roland Foisner. "Proteins that associate with lamins: many faces, many functions." In: *Experimental cell research* 313.10 (2007), pp. 2167–2179.

[167] Brian C Capell and Francis S Collins. "Human laminopathies: nuclei gone genetically awry." In: *Nature reviews genetics* 7.12 (2006), pp. 940–952.

[168] M Yabuki et al. "Role of nuclear lamins in nuclear segmentation of human neutrophils." In: *Physiological chemistry and physics and medical NMR* 31.2 (1999), pp. 77–84.

[169] Melissa Linkert et al. "Metadata matters: access to image data in the real world." In: *Journal of Cell Biology* 189.5 (2010), pp. 777–782.

[170] Mathews Jacob and Michael Unser. "Design of steerable filters for feature detection using canny-like criteria." In: *IEEE transactions on pattern analysis and machine intelligence* 26.8 (2004), pp. 1007–1019.

[171] F. Aguet. *2-D Steerable filters for feature detection*. https://github.com/francois-a/steerable. 2019.

[172] John Canny. “A computational approach to edge detection.” In: *IEEE Transactions on pattern analysis and machine intelligence* 6 (1986), pp. 679–698.

[173] P. D. Kovesi. *MATLAB and Octave Functions for Computer Vision and Image Processing*. Available from: <https://www.peterkovesi.com/matlabfns/>. 2000.

[174] Jack E Bresenham. “Algorithm for computer control of a digital plotter.” In: *IBM Systems journal* 4.1 (1965), pp. 25–30.

[175] Takeshi Shimi et al. “Structural organization of nuclear lamins A, C, B1, and B2 revealed by superresolution microscopy.” In: *Molecular biology of the cell* 26.22 (2015), pp. 4075–4086.

[176] Yagmur Turgay et al. “The molecular architecture of lamins in somatic cells.” In: *Nature* 543.7644 (2017), pp. 261–264.

[177] Y Turgay and O Medalia. “The structure of lamin filaments in somatic cells as revealed by cryo-electron tomography.” In: *Nucleus* 8.5 (2017), pp. 475–481.

[178] Mark Kittisopikul et al. “Computational analyses reveal spatial relationships between nuclear pore complexes and specific lamins.” In: *Journal of Cell Biology* 220.4 (2021).

[179] Jinsook Ahn et al. “Structural basis for lamin assembly at the molecular level.” In: *Nature communications* 10.1 (2019), pp. 1–12.

[180] Anna Payne-Tobin Jost and Jennifer C Waters. “Designing a rigorous microscopy experiment: Validating methods and avoiding bias.” In: *Journal of Cell Biology* 218.5 (2019), pp. 1452–1466.

[181] Britta Koch et al. “Confinement and Deformation of Single Cells and Their Nuclei Inside Size-Adapted Microtubes.” In: *Advanced healthcare materials* 3.11 (2014), pp. 1753–1758.

[182] Takeshi Shimi et al. “The A-and B-type nuclear lamin networks: microdomains involved in chromatin organization and transcription.” In: *Genes & development* 22.24 (2008), pp. 3409–3421.

[183] Ada L Olins et al. “The human granulocyte nucleus: Unusual nuclear envelope and heterochromatin composition.” In: *European journal of cell biology* 87.5 (2008), pp. 279–290.

[184] Melanie Salvermoser et al. “Nuclear deformation during neutrophil migration at sites of inflammation.” In: *Frontiers in immunology* 9 (2018), p. 2680.

[185] Leonardo Baptista et al. “Oxidation mechanism of dimethyl sulfoxide (DMSO) by OH radical in liquid phase.” In: *Physical Chemistry Chemical Physics* 10.45 (2008), pp. 6867–6879.

[186] Noboru Yamamoto. “Effect of dimethyl sulfoxide on cytosolic ionized calcium concentration and cytoskeletal organization of hepatocytes in a primary culture.” In: *Cell structure and function* 14.1 (1989), pp. 75–85.

[187] Neha Dixit et al. “Leukocyte function antigen-1, kindlin-3, and calcium flux orchestrate neutrophil recruitment during inflammation.” In: *The Journal of Immunology* 189.12 (2012), pp. 5954–5964.

[188] Chinmay R Surve et al. “Dynamic regulation of neutrophil polarity and migration by the heterotrimeric G protein subunits Gαi-GTP and G$\beta\gamma$.” In: *Science signaling* 9.416 (2016), ra22–ra22.

[189] Kehinde Adebayo Babatunde et al. “Chemotaxis and swarming in differentiated HL-60 neutrophil-like cells.” In: *Scientific reports* 11 (2019).

[190] Timo Kouri et al. “European urinalysis guidelines.” In: *Scandinavian journal of clinical and laboratory investigation* 60.sup231 (2000), pp. 1–96.

[191] Jeff A Simerville et al. “Urinalysis: a comprehensive review.” In: *American family physician* 71.6 (2005), pp. 1153–1162.

[192] Fatma Demet İnce et al. “The comparison of automated urine analyzers with manual microscopic examination for urinalysis automated urine analyzers and manual urinalysis.” In: *Practical laboratory medicine* 5 (2016), pp. 14–20.

[193] Tzu-I Chien et al. “Urine sediment examination: a comparison of automated urinalysis systems and manual microscopy.” In: *Clinica Chimica Acta* 384.1-2 (2007), pp. 28–34.

[194] Katherine M McKinnon. “Flow cytometry: an overview.” In: *Current protocols in immunology* 120.1 (2018), pp. 5–1.

[195] Giulia Previtali et al. “Performance evaluation of the new fully automated urine particle analyser UF-5000 compared to the reference method of the Fuchs-Rosenthal chamber.” In: *Clinica Chimica Acta* 472 (2017), pp. 123–130.

[196] Matthijs Oyaert and Joris Delanghe. “Progress in automated urinalysis.” In: *Annals of laboratory medicine* 39.1 (2019), p. 15.

[197] Barbara Pieretti et al. “Diagnosis of bacteriuria and leukocyturia by automated flow cytometry compared with urine culture.” In: *Journal of clinical microbiology* 48.11 (2010), pp. 3990–3996.

[198] Marie T Pezzlo. “Automated methods for detection of bacteriuria.” In: *The American journal of medicine* 75.1 (1983), pp. 71–78.

[199] Teresa C Horan et al. “CDC/NHSN surveillance definition of health care–associated infection and criteria for specific types of infections in the acute care setting.” In: *American journal of infection control* 36.5 (2008), pp. 309–332.

[200] J Michael Miller et al. “A guide to utilization of the microbiology laboratory for diagnosis of infectious diseases: 2018 update by the Infectious Diseases Society of America and the American Society for Microbiology.” In: *Clinical Infectious Diseases* 67.6 (2018), e1–e94.

[201] Christian Gehringer et al. “Accuracy of urine flow cytometry and urine test strip in predicting relevant bacteriuria in different patient populations.” In: *BMC infectious diseases* 21.1 (2021), pp. 1–8.

[202] V Bianco et al. “Food quality inspection by speckle decorrelation properties of bacteria colonies.” In: *Optical Methods for Inspection, Characterization, and Imaging of Biomaterials III*. Vol. 10333. International Society for Optics and Photonics. 2017, 103331N.

[203] V Bianco et al. “Detection of self-propelling bacteria by speckle correlation assessment and applications to food industry.” In: *Optical Methods for Inspection, Characterization, and Imaging of Biomaterials IV*. Vol. 11060. International Society for Optics and Photonics. 2019, p. 1106007.

[204] Jonghee Yoon et al. “A simple and rapid method for detecting living microorganisms in food using laser speckle decorrelation.” In: *arXiv preprint arXiv:1603.07343* (2016).

[205] Keren Zhou et al. “Dynamic laser speckle imaging meets machine learning to enable rapid antibacterial susceptibility testing (DyRAST).” In: *ACS sensors* 5.10 (2020), pp. 3140–3149.

[206] SeungYun Han et al. “Rapid antimicrobial susceptibility test using spatiotemporal analysis of laser speckle dynamics of bacterial colonies.” In: *BioRxiv* (2019), p. 853168.

[207] SeungYun Han et al. “Real-time monitoring of bacterial growth and fast antimicrobial susceptibility tests exploiting multiple light scattering.” In: *BioRxiv* (2018), p. 481184.

[208] Mohammad Zaheer Ansari et al. “Real time and online dynamic speckle assessment of growing bacteria using the method of motion history image.” In: *Journal of Biomedical Optics* 21.6 (2016), p. 066006.

[209] Hadi Loutfi et al. “Real-time monitoring of bacterial growth kinetics in suspensions using laser speckle imaging.” In: *Scientific reports* 10.1 (2020), pp. 1–10.

[210] Elías Todorovich et al. “Real-time speckle image processing.” In: *Journal of Real-Time Image Processing* 11.3 (2016), pp. 535–545.

[211] Lester I Goldfischer. “Autocorrelation function and power spectral density of laser-produced speckle patterns.” In: *Josa* 55.3 (1965), pp. 247–253.

[212] Christelle Abou Nader et al. “Assessing white wine viscosity variation using polarized laser speckle: A promising alternative to wine sensory analysis.” In: *Sensors* 17.10 (2017), p. 2340.

[213] Ana L Flores-Mireles et al. “Urinary tract infections: epidemiology, mechanisms of infection and treatment options.” In: *Nature reviews microbiology* 13.5 (2015), pp. 269–284.

[214] Aleksei E Balaev et al. “Refractive index of Escherichia coli cells.” In: *Saratov Fall Meeting 2001: Optical Technologies in Biophysics and Medicine III*. Vol. 4707. International Society for Optics and Photonics. 2002, pp. 253–260.

[215] Savarimuthu Robinson and Nagaraj Dhanlaksmi. “Photonic crystal based biosensor for the detection of glucose concentration in urine.” In: *Photonic Sensors* 7.1 (2017), pp. 11–19.

[216] Recep Öztürk and Ahmet Murt. “Epidemiology of urological infections: A global burden.” In: *World journal of urology* (2020), pp. 1–11.

[217] Payam Behzadi et al. “A survey on urinary tract infections associated with the three most common uropathogenic bacteria.” In: *Maedica* 5.2 (2010), p. 111.